# ASSESSMENT OF CARBON STORAGE IN SUBSURFACE VIA WELL AND SEISMIC DRIVEN PROPERTIES OF KADANWARI GAS FIELD LOWER INDUS BASIN PAKISTAN

**EHTESHAM HAIDER**

**(09-262232-024)**

**BAHRIA UNIVERSITY, ISLAMABAD**

# ASSESSMENT OF CARBON STORAGE IN SUBSURFACE VIA WELL AND SEISMIC DRIVEN PROPERTIES OF KADANWARI GAS FIELD LOWER INDUS BASIN PAKISTAN

**EHTESHAM HAIDER**

**(09-262232-024)**

A thesis submitted in fulfilment of the requirements for the award of the degree of Masters of Geophysics

**Department of Earth and Environmental Sciences**

**BAHRIA UNIVERSITY, ISLAMABAD**

**AUGUST, 2026**

# APPROVAL FOR EXAMINATION

**Scholar's Name:** Ehtesham Haider

**Registration No.** 09-262242-023

**Programme of Study:** Ms-Geophysics

**Thesis Title:** Assessment Of Carbon Storage In Subsurface Via Well And Seismic Driven Properties Of Kadanwari Gas Field Lower Indus Basin Pakistan

It is to certify that the above scholar's thesis has been completed to my satisfaction and, to my belief, its standard is appropriate for submission for examination. I have also conducted plagiarism test of this thesis using HEC prescribed software and found similarity index 13% that is within the permissible limit set by the HEC for the MS degree thesis. I have also found the thesis in a format recognized by the BU for the MS thesis.

Principal Supervisor’s Signature_____

Date:

Name:

## AUTHOR'S DECLARATION

I, Ehtesham Haider hereby state that my ms/mphil thesis titled " Assessment Of Carbon Storage In Subsurface Via Well And Seismic Driven Properties Of Kadanwari Gas Field Lower Indus Basin Pakistan" is my own work and has not been submitted previously by me for taking any degree from this university Bahria University or anywhere else in the country/world. At any time if my statement is found to be incorrect even after my Graduate the university has the right to withdraw/cancel my MS/MPhil degree.

**Name of scholar:** Ehtesham Haider

**Date:**

# PLAGIARISM UNDERTAKING

I, solemnly declare that research work presented in the thesis titled " Assessment Of Carbon Storage In Subsurface Via Well And Seismic Driven Properties Of Kadanwari Gas Field Lower Indus Basin Pakistan" is solely my research work with no significant contribution from any other person. Small contribution help wherever taken has been duly acknowledged and that complete thesis has been written by me.

I understand the zero tolerance policy of the HEC and Bahria University towards plagiarism. Therefore I as an Author of the above titled thesis declare that no portion of my thesis has been plagiarized and any material used as reference is properly referred/ cited.

I undertake that if I am found guilty of any formal plagiarism in the above titled thesis even after award of MS/MPhil degree, the university reserves the right to withdraw / revoke my MS/MPhil degree and that HEC and the University has the right to publish my name on the HEC University website on which names of students are placed who submitted plagiarized thesis.

Scholar / Author's Sign: _____

Name of scholar: Ehtesham Haider

# ACKNOWLEDGEMENTS

We are thankful to Almighty Allah, the most beneficent and the most merciful, for his boundless blessings with which we qualified to pursue this thesis despite living in one of the most unprecedented times in our history.

I express my deep gratitude to my supervisor Dr. Urooj Shakir, Senior Associate Professor and my Department of Earth and Environmental Sciences, Bahria University, Islamabad, for their invaluable guidance and supervision, which contributed significantly to the success of this research. I would also like to extend my thanks to my dedicated teachers, at Bahria University, Islamabad, for unwavering support throughout our academic journey.

My appreciation also goes out to our colleagues, whose help and cooperation have been invaluable. I'm forever grateful to my parents and other family members for their unwavering belief in my abilities and constant encouragement. Their prayers and unwavering support have been a constant source of motivation. I'll always cherish their prayers and tireless efforts.

# ABSTRACT

The Kadanwari Gas Field lies on the Thar Platform of the Lower Indus Basin. It is a mature field: primary recovery is largely complete, but the reservoir–seal pair is still intact and a large body of subsurface data has been collected over its producing life. This makes it a natural candidate for $CO_2$ storage. Pakistan does not yet operate a $CO_2$ storage project. The only published storage study at Kadanwari examined a different interval, did not test the bounding faults, and did not derive reservoir properties from seismic inversion. This thesis addresses those gaps by assessing the storage potential of the Lower Goru B sand, the deepest and least studied of the field's sand units, using properties derived from both well logs and two-dimensional (2D) seismic data. The dataset comprises ten 2D seismic lines and three wells. Volume of shale, porosity and water saturation were calculated at each well. Three horizons and the north-northwest to south-southeast trending normal fault system were mapped in time and converted to depth. Model-based acoustic impedance inversion was carried out along the three lines tied to wells, and an Extra Trees regression model trained on the inverted impedance was then applied trace by trace to predict reservoir properties away from the wells. The sealing potential of the bounding fault, F3, was evaluated using a juxtaposition diagram, and storage capacity was estimated volumetrically for each mapped closure. The B sand occurs between 3,438 and 3,462 m depth over a fault-bounded high to the north of Kadanwari-03. All three inverted lines show a laterally continuous zone of low impedance at reservoir level. Along most of its length, fault F3 juxtaposed sand against shale, providing two possible positions along the fault that may act as sealing windows. Storage capacity was calculated from effective porosity, volume of shale and water saturation, together with closure area and reservoir thickness. Assuming a $CO_2$ density of 600 kg/m$^3$, Closures 1, 2 and 3 hold an estimated 81,968, 167,808 and 326,823 tonnes respectively, giving a combined capacity of 576,599 tonnes (about 0.58 Mt). These figures are static, and apply only to the three mapped Closures. They support treating the closures as preliminary storage targets, with Closure 3 the most promising, but they do not establish either injectivity or long-term containment.

# TABLE OF CONTENT


| | | Pages |
|---|---|---|
| APPROVAL FOR EXAMINATION | | III |
| AUTHOR'S DECLARATION | | IV |
| PLAGIARISM UNDERTAKING | | V |
| ACKNOWLEDGEMENTS | | VI |
| ABSTRACT | | VII |
| TABLE OF CONTENT | | VIII |
| LIST OF FIGURES | | XII |
| LIST OF TABLES | | XIX |
| CHAPTER 1 | | 1 |
| INTRODUCTION | | 1 |
| 1.1 | Introduction | 1 |
| 1.2 | Study Area | 3 |
| 1.3 | Geological Setting of the Lower Indus Basin | 5 |
| 1.4 | Structural Framework of the Study Area | 7 |
| 1.5 | Stratigraphy of the Lower Indus Basin | 9 |
| 1.6 | Petroleum System of the Lower Indus Basin | 11 |
| | 1.6.1 Source Rocks | 11 |
| | 1.6.2 Reservoir Rocks | 11 |
| | 1.6.3 Seal Rocks | 12 |
| | 1.6.4 Traps and Hydrocarbon Migration Pathways | 12 |

1.7 Geological and Petrophysical Characteristics of the Kadanwari Gas Field 13
1.7.1 Reservoir Lithology 13
1.7.2 Porosity 14
1.7.3 Permeability 15
1.7.4 Fluid Saturation 15
1.8 Problem Statement 16
1.9 Research Gap 16
1.10 Research Objectives 17
1.11 Research Questions 17
1.12- Research Significance 18
1.13- Thesis Outline 19
CHAPTER 2 21
LITERATURE REVIEW 21
2.1 Literature Review 21
CHAPTER 3 28
METHODOLOGY 28
3.1 Adopted Methodology 28
3.2 Dataset 30
3.3 Petrophysical Analysis 32
3.3.1 Volume of Shale (Vsh) 33
3.3.2 Porosity Estimation (φ) 33
3.4 Structural Interpretation 34
3.4.1Data Loading 34
3.4.2 Seismic-to-Well Tie 35
3.4.3 Fault and Horizon Marking 35
3.4.4 Time-Structure Mapping 36

3.4.5 Depth-Structure Mapping 36
3.5 Machine Learning 37
3.5.1 Extra Trees Regression 37
3.5.2 Machine Learning on Seismic Data 38
3.5.3 Machine Learning on Well Data 39
3.5.4 Training, Prediction and Validation 39
3.5.5 Limitation 40
3.6 Model-Based Seismic Inversion 40
3.6.1 Wavelet Extraction and Well Correlation 41
3.6.2 Inverted Trace 41
3.6.3 Final Impedance Model 42
3.7 Fault Seal Analysis 42
3.8 Storage Capacity Estimation 43
CHAPTER 4 46
RESULTS AND INTERPRETATION 46
4.1 Introduction 46
4.2 Petrophysical Results 46
4.2.1 Kadanwari-01 47
4.2.2 Kadanwari-03 48
4.2.3 Kadanwari-04 49
4.2.4 Summary of the Petrophysical Results 50
4.3 Seismic Interpretation 50
4.3.1 Seismic-to-Well Ties 51
4.3.2 Interpreted Seismic Sections 52
4.3.3 Time and Depth Structure Maps 60
4.4 Machine Learning 62

4.4.1 Line TJ-89-512 (Kadanwari-03) 63

4.4.2 Line TJ-89-516 (Kadanwari-01) 66

4.4.3 Line TJ-89-526 (Kadanwari-04) 69

4.4.4 Summary of the Machine Learning Results 72

4.5 Seismic Inversion 73

4.5.3 Kadanwari-01 (Line TJ-89-516) 73

4.5.1 Kadanwari-03 (Line TJ-89-512) 81

4.5.2 Kadanwari-04 (Line TJ-89-526) 90

4.5.4 Summary of the Inversion Results 97

4.6 Fault Seal Analysis 100

4.7 Storage Capacity Estimation 101

4.7.1 Three closure areas marked 102

CHAPTER 5 106

DISCUSSION 106

CONCLUSIONS 110

REFERENCES 111

# LIST OF FIGURES

**Pages**

Figure 1. 1 Location of the Kadanwari Gas Field in Sindh Province, Lower Indus Basin, Pakistan, shown on the regional geological map with the study area inset (after Ali et al., 2019b). 7

Figure 1. 2 Tectonic setting of the Kadanwari Gas Field, bounded by the Sulaiman Fold Belt to the north and the Sukkur Rift and Kirthar Foredeep to the south, with the structural elements of the platform (Khan et al., 2024). 9

Figure 1. 3 Generalised stratigraphy of the Lower Indus Basin showing source, reservoir and seal intervals (a), together with the Lower Goru sand nomenclature adopted by different operators (b). The ENI scheme followed in this thesis is shown in the LASMO/ENI column (Khan et al., 2024). 10

Figure 2. 1 Principal geological storage options for CO2, comprising depleted oil and gas reservoirs, deep saline aquifers, unmineable coal seams and basalt formations, with onshore and offshore injection configurations. 22

Figure 3. 1 Methodology Workflow 29

Figure 4. 1 Composite petrophysical display for Kadanwari-01 showing the correlation, resistivity, porosity, sonic and photoelectric factor tracks together with the computed volume of shale, total and effective porosity and water saturation over the Lower Goru Sand B interval. 48

Figure 4. 2 Composite petrophysical display for Kadanwari-03 showing the computed volume of shale, total and effective porosity and water saturation over the logged Lower Goru H-Sand interval. 49

Figure 4. 3 Composite petrophysical display for Kadanwari-04 showing the computed volume of shale, total and effective porosity and water saturation over the logged Lower Goru interval. 50

Figure 4. 4 Seismic-to-well tie for Kadanwari-01 on line TJ-89-516, showing the sonic, density, impedance, velocity and reflectivity tracks, the synthetic seismogram and the extracted seismic trace with the Lower Goru sand tops posted. 51

Figure 4. 5 Seismic-to-well tie for Kadanwari-03 on line TJ-89-512, showing the synthetic seismogram against the seismic trace extracted at the well location. 52

Figure 4. 6 Seismic-to-well tie for Kadanwari-04 on line TJ-89-526, showing the synthetic seismogram against the extracted seismic trace. 52

Figure 4. 7 Interpreted seismic section along line TJ-89-510 showing the Upper Goru, Lower Goru B sand and Chiltan horizons and the interpreted faults. 53

Figure 4. 8 Interpreted seismic section along line TJ-89-512 with Kadanwari-03 projected onto the section, showing the interpreted horizons and faults. 54

Figure 4. 9 Interpreted seismic section along line TJ-89-516 with Kadanwari-01 projected onto the section, showing the interpreted horizons and the major bounding faults. 55

Figure 4. 10 Interpreted seismic section along line TJ-89-518 showing the interpreted horizons, the graben in the western part of the line and the horst block in the east. 56

Figure 4. 11 Interpreted seismic section along line TJ-89-520 showing the interpreted horizons and faults, with the intersection with line TJ-88-207 marked. 57

Figure 4. 12 Interpreted seismic section along line TJ-89-522 showing the interpreted horizons and faults. 58

Figure 4. 13 Interpreted seismic section along line TJ-89-524 showing the interpreted horizons and faults, with the intersections with lines TJ-88-207 and TJ-91-803 marked. 59

Figure 4. 14 Interpreted seismic section along line TJ-89-526 with Kadanwari-04 projected onto the section, showing the interpreted horizons and the faults bounding the well block. 60

Figure 4. 15 Time-structure map of the Lower Goru B sand, contoured in two-way travel time, with the three well locations posted. 61

Figure 4. 16 Depth-structure map of the Lower Goru B sand, converted from the time-structure map and used as the basis for the fault-seal analysis. 62

Figure 4. 17 Predicted volume of shale along line TJ-89-512, calibrated at Kadanwari-03, displayed on a scale from 0.15 to 0.70. 63

Figure 4. 18 Predicted total porosity along line TJ-89-512, calibrated at Kadanwari-03, displayed on a scale from 0.10 to 0.30. 64

Figure 4. 19 Predicted effective porosity along line TJ-89-512, calibrated at Kadanwari-03, displayed on a scale from 0.04 to 0.20. 64

Figure 4. 20 Predicted water saturation along line TJ-89-512, calibrated at Kadanwari-03, displayed on a scale from 0.30 to 1.00; blue denotes the highest saturations. 65

Figure 4. 21 Predicted Premeability along line TJ-89-512, calibrated at Kadanwari-03, displayed on a scale from 0.00 to 42.00. 65

Figure 4. 22 Predicted volume of shale along line TJ-89-516, calibrated at Kadanwari-01, displayed on a scale from 0.25 to 0.75. 66

Figure 4. 23 Predicted total porosity along line TJ-89-516, calibrated at Kadanwari-01, displayed on a scale from 0.15 to 0.65; values above approximately 1,300 ms lie outside the calibrated range. 67

Figure 4. 24 Predicted effective porosity along line TJ-89-516, calibrated at Kadanwari-01, displayed on a scale from 0.10 to 0.60; the elevated values between approximately 2,400 and 2,500 ms coincide with the low-impedance zone of Figure 4.32. 67

Figure 4. 25 Predicted water saturation along line TJ-89-516, calibrated at Kadanwari-01, displayed on a scale from 0.30 to 0.85; blue denotes the highest saturations. 68

Figure 4. 26 Predicted Permeability along line TJ-89-516, calibrated at Kadanwari-01, displayed on a scale from 0.00 to 42.00. 69

Figure 4. 27 Predicted volume of shale along line TJ-89-526, calibrated at Kadanwari-04, displayed on a scale from 0.25 to 0.75. 69

Figure 4. 28 Predicted total porosity along line TJ-89-526, calibrated at Kadanwari-04, displayed on a scale from 0.15 to 0.40. 70

Figure 4. 29 Predicted effective porosity along line TJ-89-526, calibrated at Kadanwari-04, displayed on a scale from 0.05 to 0.30; the response below approximately 1,900 ms is effectively uniform. 70

Figure 4. 30 Predicted water saturation along line TJ-89-526, calibrated at Kadanwari-04, displayed on a scale from 0.45 to 0.95; blue denotes the highest saturations. 71

Figure 4. 31 Predicted Permeability along line TJ-89-526, calibrated at Kadanwari-04, displayed on a scale from 0.00 to 42.00. 71

Figure 4. 32 Wavelet extracted over the Kadanwari-01 well-tie window, showing the time response (upper) and the amplitude spectrum (lower). 74

Figure 4. 33 Seismic-to-well tie for Kadanwari-01 on line TJ-89-516, showing the density, P-wave velocity and volume of shale tracks with the H to B sand tops posted, the synthetic seismogram against the extracted seismic trace, and the cross-correlation function computed over the 1,270 to 2,500 ms window. 75

Figure 4. 34 Initial low-frequency impedance model along line TJ-89-516, built from the interpreted horizons and the upscaled impedance log at Kadanwari-01. 75

Figure 4. 35 Log upscaling quality control at Kadanwari-01, comparing the upscaled P-impedance log with the synthetic seismogram and the extracted seismic trace at CDP 315. 76

Figure 4. 36 Cross-plot of inverted P-impedance against original P-impedance at Kadanwari-01, with the 45-degree reference line and the best-fit regression. 77

Figure 4. 37 Inverted P-impedance section along line TJ-89-516 with Kadanwari-01 tied at the well location; the low-impedance zone beneath the Lower Goru Sand horizon is highlighted. 78

Figure 4. 38 Predicted volume of shale along line TJ-89-516, calibrated at Kadanwari-01, displayed on a scale from 0.4428 to 0.7383 v/v. 79

Figure 4. 39 Predicted porosity along line TJ-89-516, calibrated at Kadanwari-01, displayed on a scale from 0.0280 to 0.4000 v/v. 80

Figure 4. 40 Predicted water saturation along line TJ-89-516, calibrated at Kadanwari-01, displayed on a scale from 0.5205 to 0.9056 v/v; dark blue denotes the highest saturations. 80

Figure 4. 41 Predicted permeability along line TJ-89-516, calibrated at Kadanwari-01, displayed on a scale from 0.0 to 40.0 mD. 81

Figure 4. 42 Statistical wavelet extracted from the seismic data between the Khadro and Chiltan levels for the inversion at Kadanwari-03, showing the time response (upper) and the amplitude spectrum (lower). 82

Figure 4. 43 Seismic-to-well tie for Kadanwari-03 on line TJ-89-512, showing the density, P-wave velocity and volume of shale tracks, the synthetic seismogram against the extracted seismic trace, and the cross-correlation function computed over the 1,100 to 2,400 ms window. 83

Figure 4. 44 Initial low-frequency impedance model along line TJ-89-512, built from the interpreted horizons and the upscaled impedance log at Kadanwari-03. 83

Figure 4. 45 Comparison of the inverted, upscaled and original impedance logs at Kadanwari-03, with the synthetic generated from the inverted result, the seismic trace at CDP 440 and the residual error. 84

Figure 4. 46 Cross-plot of inverted P-impedance against original P-impedance at Kadanwari-03, with the 45-degree reference line and the best-fit regression. 85

Figure 4. 47 Inverted P-impedance section along line TJ-89-512 with Kadanwari-03 tied at CDP 440. The highlighted interval, immediately below the Lower Goru Sand horizon, carries approximately 9,400 to 10,500 (m/s)(g/cc) between two thin high-impedance bands; the thick low-impedance interval below approximately 2,440 ms lies beneath the base of the logged section at the well. 86

Figure 4. 48 Predicted volume of shale along line TJ-89-512, calibrated at Kadanwari-03, displayed on a scale from 0.4428 to 0.7323 v/v; the highlighted interval carries the shale-rich buff response. 87

Figure 4. 49 Predicted porosity along line TJ-89-512, calibrated at Kadanwari-03, displayed on a scale from 0.0280 to 0.4000 v/v. 88

Figure 4. 50 Predicted water saturation along line TJ-89-512, calibrated at Kadanwari-03, displayed on a scale from 0.5205 to 0.9056 v/v; dark blue denotes the highest saturations. 88

Figure 4. 51 Predicted permeability along line TJ-89-512, calibrated at Kadanwari-03, displayed on a scale from 0.0 to 40.0 mD. 89

Figure 4. 52 Statistical wavelet applied to the inversion along line TJ-89-526 at Kadanwari-04, showing the time response (upper) and the amplitude spectrum (lower). 90

Figure 4. 53 Seismic-to-well tie for Kadanwari-04 on line TJ-89-526, showing the density, P-wave velocity and volume of shale tracks, the synthetic seismogram against the extracted seismic trace, and the cross-correlation function computed over the 1,500 to 2,360 ms window. 91

Figure 4. 54 Initial low-frequency impedance model along line TJ-89-526, built from the interpreted horizons and the upscaled impedance log at Kadanwari-04. 92

Figure 4. 55 Comparison of the inverted, upscaled and original impedance logs at Kadanwari-04, with the synthetic, the recorded seismic trace and the residual error. 92

Figure 4. 56 Cross-plot of inverted P-impedance against original P-impedance at Kadanwari-04, with the 45-degree reference line and the best-fit regression. 93

Figure 4. 57 Inverted P-impedance section along line TJ-89-526 with Kadanwari-04 tied at CDP 510. The highlighted interval, immediately below the Lower Goru Sand horizon, carries approximately 10,100 to 10,600 (m/s)(g/cc) with a laterally continuous high-impedance band developed within it; the green low-impedance interval higher in the Lower Goru lies between approximately 1,450 and 1,900 ms. 94

Figure 4. 58 Predicted volume of shale along line TJ-89-526, calibrated at Kadanwari-04, displayed on a scale from 0.4428 to 0.7323 v/v. 95

Figure 4. 59 Predicted porosity along line TJ-89-526, calibrated at Kadanwari-04, displayed on a scale from 0.0280 to 0.4000 v/v. 95

Figure 4. 60 Predicted water saturation Line TJ-89-526, calibrated at Kadanwari-04, displayed on a scale from 0.5205 to 0.9056 v/v. 96

Figure 4. 61 Predicted permeability along line TJ-89-526, calibrated at Kadanwari-04, displayed on a scale from 0.0 to 40.0 mD. 97

Figure 4. 62 Juxtaposition diagram for fault F3, constructed from the upthrown and downthrown cut-off depths of the D sand, the C sand and the Lower Goru B sand read at nine positions along the fault trace. Solid lines denote the upthrown block and broken lines the downthrown block; the reservoir base is taken as the top of the underlying shale. The intervals shown in red are the possible sealing areas identified from the juxtaposition. 101

Figure 4. 63 Delineation of Closure 1 on the gridded Lower Goru B sand structure map used for the volumetric $CO_2$ storage-capacity estimation, three well locations posted. 102

Figure 4. 64 Delineation of Closure 2 on the gridded Lower Goru B sand structure map used for the volumetric $CO_2$ storage-capacity estimation, three well locations posted. 103

Figure 4. 65 Delineation of Closure 3 on the gridded Lower Goru B sand structure map used for the volumetric $CO_2$ storage-capacity estimation, three well locations posted. 104

# LIST OF TABLES

**Pages**

Table 3. 1 Two-dimensional seismic lines used in this study, their well control and the analysis carried out on each. 30

Table 3. 2 Wells used in this study, the seismic lines on which they lie, the log suite available in each and the stratigraphic interval covered 31

Table 4. 1 Formation tops recorded in Kadanwari-01 for the Lower Goru sand units and the underlying Sembar Formation. 47

Table 4. 2 Quality-control summary of the model-based inversion at the three wells, giving the seismic-to-well tie parameters, the correlation between the synthetic generated from the inverted result and the recorded trace, the cross-plot errors against the 45-degree reference line and the best-fit regression, the impedance and time interval of the zone highlighted on each inverted section, and the lowest impedance reached within the logged part of the Lower Goru on each line. Impedance and error values are in (m/s)(g/cc). 98

Table 4. 3 Estimated volumetric $CO_2$ storage capacity of the three structural closures delineated on the Lower Goru B sand, calculated using an adopted $CO_2$ density of 600 kg/m³. 104

# CHAPTER 1
# INTRODUCTION

## 1.1 Introduction

Carbon dioxide (CO2) released from fossil-fuel combustion, industrial burning of gases and land-use change remains the dominant driver of the ongoing perturbation of the global carbon cycle. Global fossil CO2 emissions have continued to rise over recent decades and now exceed 37 Gt CO2 per year, with the atmospheric growth rate showing no sustained decline (Friedlingstein et al., 2025). Because the energy systems of most developing economies remain fossil-dominated, and because the replacement of that infrastructure will take decades, emission reductions achieved through efficiency gains and fuel switching alone are unlikely to occur quickly enough to stabilise atmospheric concentrations (Hepple & Benson, 2005). Carbon management therefore requires a group of measures, one of which is the measured capture of CO2 from concentrated point sources.

Carbon capture and storage (CCS) describes this chain of operations. It comprises three distinct stages. capture in which CO2 is separated from a flue-gas or process stream. Transport in which the captured stream is compressed and moved by pipeline. ship or tanker; and storage in which the CO2 is injected into a receiving medium and retained there (Metz et al., 2005). Only the third stage is a geoscientific problem in the strict sense, and it is the stage addressed in this thesis. Geological carbon storage (GCS) refers specifically to the injection of CO2 into porous and permeable rock at depths sufficient for the CO2 to exist as a dense supercritical phase, generally below about 800 m, where it is retained by a combination of physical and chemical mechanisms (Bachu, 2003; Metz et al., 2005).

Four classes of geological setting are conventionally considered for GCS. Deep saline formations offer the largest theoretical pore volume and are widely distributed, but are typically the least characterised and require the acquisition of new subsurface data (Bachu et al., 2007; Bashir et al., 2024). Depleted or mature oil and gas reservoirs are comparatively well documented, because seismic, well-log, core and production data are usually already available, and their capacity to retain buoyant fluids has been demonstrated over geological time (Bashir et al., 2024; Yang et al., 2023). Unmineable coal seams may store CO2 by adsorption onto the coal matrix, and basaltic formations may fix CO2 as carbonate minerals through reaction with calcium, magnesium and iron (Hazarika et al., 2024). Retention in any of these settings arises from several mechanisms operating on different timescales: structural and stratigraphic trapping beneath a low-permeability seal, residual or capillary trapping of

disconnected CO2 ganglia within the pore network, dissolution of CO2 into formation brine, and, over much longer periods, mineral trapping (Metz et al., 2005).

Depleted and mature hydrocarbon reservoirs occupy a particular position in this hierarchy. The presence of a hydrocarbon accumulation demonstrates that a reservoir–seal pair existed and functioned over geological time, that a structural or stratigraphic trap was capable of holding a buoyant phase, and that the containment system was not breached during burial and deformation (Yang et al., 2023). These advantages, however, do not amount to proof of suitability. A reservoir that held methane is not automatically a reservoir that will retain CO2: supercritical CO2 differs from natural gas in density, viscosity, interfacial tension and chemical reactivity, and CO2-bearing brine is acidic and may alter mineralogy, and pore structure (Ali et al., 2019a; Hazarika et al., 2024). It is equally important to distinguish hydrocarbon reserves from CO2 storage capacity. Reserves describe recoverable hydrocarbon volumes under economic and technical constraints, whereas storage capacity describes the pore volume that can accept CO2, and the two quantities are related only indirectly through the pore volume vacated by production and the properties of CO2 at reservoir conditions (Bachu et al., 2007). Storage capacity is itself a graded concept, ranging from theoretical capacity, through effective capacity constrained by geological and engineering cut-offs, to practical capacity that additionally reflects regulatory and economic limits (Bachu et al., 2007).

The parameters that govern storage potential are consequently numerous. Depth, pressure and temperature determine the phase state and density of CO2 and therefore the mass that a given pore volume can accommodate (Bachu, 2003). Porosity and net reservoir thickness determine the pore volume itself; permeability, pore connectivity and reservoir continuity determine whether that volume is accessible to an injected plume; and lithology, clay content and diagenetic history exert control on both (Bachu et al., 2007). In situ fluid saturation determines how much of the pore space is already occupied. At the trap scale, structural closure, fault geometry, fault-seal behaviour and the thickness and continuity of the overlying caprock determine whether an injected plume remains confined, while reservoir heterogeneity and compartmentalisation determine how the plume migrates and how much of the reservoir it contacts. Faults deserve particular attention, because the same structures that create closure may, depending on juxtaposition relationships and fault-rock properties, act either as lateral barriers or as vertical migration pathways (Allan, 1989; Yielding et al., 1997). The present study does not evaluate all of these parameters; it addresses the subset that can be constrained from well logs and surface seismic data, namely

lithology, porosity, density, permeability, fluid saturation, reservoir geometry and fault juxtaposition relationships.

Wireline logs provide continuous, high-resolution measurements along the borehole and are the primary basis for quantifying shale volume, porosity, bulk density and water saturation, and for identifying the vertical succession of reservoir and non-reservoir intervals (Ali et al., 2019b). Reflection seismic surveys image structure and stratigraphic architecture over the full extent of a field, define fault geometry and trap configuration, and, through inversion, can be transformed into volumes of acoustic impedance from which reservoir properties may be estimated (Ahmad et al., 2007; Ali et al., 2023).

National CO2 emissions from large industrial point sources are modest by regional standards but are growing, and an early assessment of the subcontinent estimated that Pakistan's gas fields could offer on the order of 1.6 Gt of CO2 storage capacity once depleted, with additional potential in saline formations of the Indus and Potwar basins and a favourable geographic relationship between emission sources and candidate sinks (Holloway et al., 2009). Despite this, no CO2 storage project has been implemented in the country, and field-scale geoscientific assessment remains sparse (Shah et al., 2024). The Indus Basin contains the majority of Pakistan's producing gas fields, and the Cretaceous Lower Goru Formation is the principal clastic reservoir of the Indus platform (Ahmad & Ghazi, 2022; Khan et al., 2024). This thesis therefore assesses the subsurface carbon-storage potential of the Kadanwari Gas Field through reservoir properties derived jointly from well logs and seismic data. The assessment is directed at the Lower Goru B sand, the lowermost of the sand units in the nomenclature used by the field operator. That interval is reached only by the well that penetrates the full Lower Goru succession, and it has not been the subject of a previous storage assessment.

## 1.2 Study Area

The Kadanwari Gas Field lies in District Khairpur, Sindh Province, in southeastern Pakistan, at approximately 27°10′ N and 69°19′ E. Structurally it occupies the southeastern flank of the Jacobabad–Khairpur High, on the platform region east of the Sukkur Rift (Ali et al., 2022; Shah et al., 2024). The basin nomenclature applied to this part of Pakistan is not uniform in the published literature, and the difference is terminological rather than substantive: the same area is described as the Lower Indus Basin by Khan et al. (2024), as the Middle Indus Basin by Ahmad and Chaudhry (2002), Ali et al. (2022) and Shah et al. (2024), and as the Central Indus Basin by Saif-Ur-Rehman et al. (2020). This thesis follows

the usage adopted in its title and refers to the Lower Indus Basin, consistent with Khan et al. (2024), while noting that studies using the alternative terms describe the same geological setting.

The field was discovered in 1989 within the Tajjal exploration licence on the Thar Platform. The trap is a fault-bounded closure developed at two horizons within the Lower Goru Formation, on a north-northwest to south-southeast trending nose east of the Khairpur High. Three appraisal wells were drilled, each of which tested gas, and initial sales-gas reserves were estimated at approximately 728 × 109 SCF. Subsequent development drilling and early production performance showed that the accumulation was substantially smaller than the original four-way-closure model implied, and after seismic reprocessing the reserves were revised downward to less than 200 × 109 SCF (Ahmad & Chaudhry, 2002). Production began in mid-1995, and the field has since been operated in partnership by ENI, OGDCL and UEPL (Raza et al., 2020). Deliverability has declined over the field's life, and the increments achieved through infill drilling and tie-ins have been short-lived and dependent on new well commissioning, not on sustained reservoir energy (Khan et al., 2024). The field is now in a mature stage of development in which primary recovery is largely exhausted while reservoir pressure is reduced and surface and subsurface infrastructure remain in place.

Several operators have applied different sand nomenclatures to the Lower Goru succession; this thesis follows the ENI scheme used by the field operator, in which the sand units are labelled B to H, the H sand uppermost and the B sand at the base of the succession. Production at Kadanwari has come principally from the E and G sands, and published work at the field has concentrated on those units: Ali et al. (2023) benchmarked inversion algorithms on the thin-bedded E sand, Khan et al. (2024) reported net pay within it, and the storage assessment of Shah et al. (2024) covered the interval between the G and E sands. The interval assessed in this thesis is the B sand, which lies beneath all of these and is correspondingly less well described.

The Lower Goru sands were deposited by westerly prograding, river-dominated deltaic to shallow-marine systems draining the Indian Shield to the east and southeast (Raza et al., 2020). Deposition occurred as multiple vertically stacked sand bodies interbedded with shaly packages, so that reservoir quality varies markedly both laterally and vertically (Khan et al., 2024). Trapping consequently reflects a combination of structural closure and stratigraphic loss of reservoir quality through lateral pinch-out, which produces pronounced (Khan et al., 2024). Diagenesis is an additional control on reservoir quality in Lower Goru sandstones of the Indus Basin (Baig et al., 2016).

The structural framework was established by three tectonic episodes: uplift and erosion during the Late Cretaceous; wrench faulting during the Late Paleocene; and renewed uplift from the Late Tertiary to Recent, accompanied by inversion associated with the Jacobabad–Khairpur High (Ahmad & Ghazi, 2022). The resulting fault system trends north-northwest to south-southeast and divides the field into horst and graben blocks; sections through parts of the field have been interpreted as displaying flower-structure geometry associated with wrench deformation, although the relative importance of strike-slip and purely extensional mechanisms in the Kadanwari and neighbouring Miano fields has been debated (Khan et al., 2023; Saif-Ur-Rehman et al., 2020). Independently of that debate, the practical consequence is agreed: the faults partition the reservoir into discrete compartments, and reservoir units are separated across fault planes (Khan et al., 2024; Shah et al., 2024).

For the purposes of this thesis, three attributes of the field are relevant. First, the reservoir–seal pair is established and its behaviour over geological time is documented. Second, the field is data-rich, with two-dimensional seismic coverage and multiple wells carrying the log suites required for petrophysical evaluation. Third, and less favourably, the reservoir is structurally heterogeneous and penetrated by numerous wells, so any assessment of storage potential must consider fault juxtaposition and containment explicitly instead of assuming them. These attributes make Kadanwari a suitable candidate for assessment, but they do not by themselves establish that it is a suitable storage site.

## 1.3 Geological Setting of the Lower Indus Basin

The Indus Basin occupies the northwestern margin of the Indian Plate and contains the greater part of Pakistan's hydrocarbon resources. Its evolution reflects the breakup of Gondwana, the separation of the Indian Plate from Madagascar and the Seychelles, the northward drift of the plate through the Late Cretaceous and Paleogene, and its eventual collision with Eurasia (Kadri, 1995; Kazmi & Jan, 1997). These stages produced a rift-to-drift succession in which Jurassic carbonate platforms were succeeded by Cretaceous siliciclastic systems, and subsequently a foreland setting in which the western and northern margins of the basin were deformed into the Kirthar and Sulaiman fold belts while the eastern part remained a comparatively stable platform (Kazmi & Jan, 1997).

Terminology for the subdivisions of this basin is inconsistent in the literature, and the reader should treat the difference as one of naming, not of geology. The area containing Kadanwari is described as the Lower Indus Basin by Khan et al. (2024), as the Middle Indus Basin by Ahmad and Chaudhry (2002), Ali et al. (2022) and Shah et al. (2024), and as the

Central Indus Basin by Saif-Ur-Rehman et al. (2020). This thesis follows the usage of Khan et al. (2024) and refers to the Lower Indus Basin, consistent with the title of the research.

Within the basin, a series of north-northwest to south-southeast trending basement highs and intervening depressions controls the distribution of Cretaceous reservoirs. Kadanwari lies on the southeastern flank of the Jacobabad–Khairpur High, on the platform east of the Sukkur Rift (Ali et al., 2022; Shah et al., 2024). Saif-Ur-Rehman et al. (2020) placed the Kadanwari and Miano fields on the Pano Aqil graben and Kadanwari High, between the Jacobabad–Khairpur and Mari–Kandhkot highs. The same structural province hosts the Miano, Sawan and Qadirpur fields, and the substantial literature on those fields provides useful analogues for reservoir quality and depositional style (Berger et al., 2009; Krois et al., 1998; Razaq et al., 2025). The platform setting is important for storage assessment for two reasons: it is tectonically quieter than the fold belts to the west, and it is densely drilled, so the subsurface is comparatively well constrained by existing data.

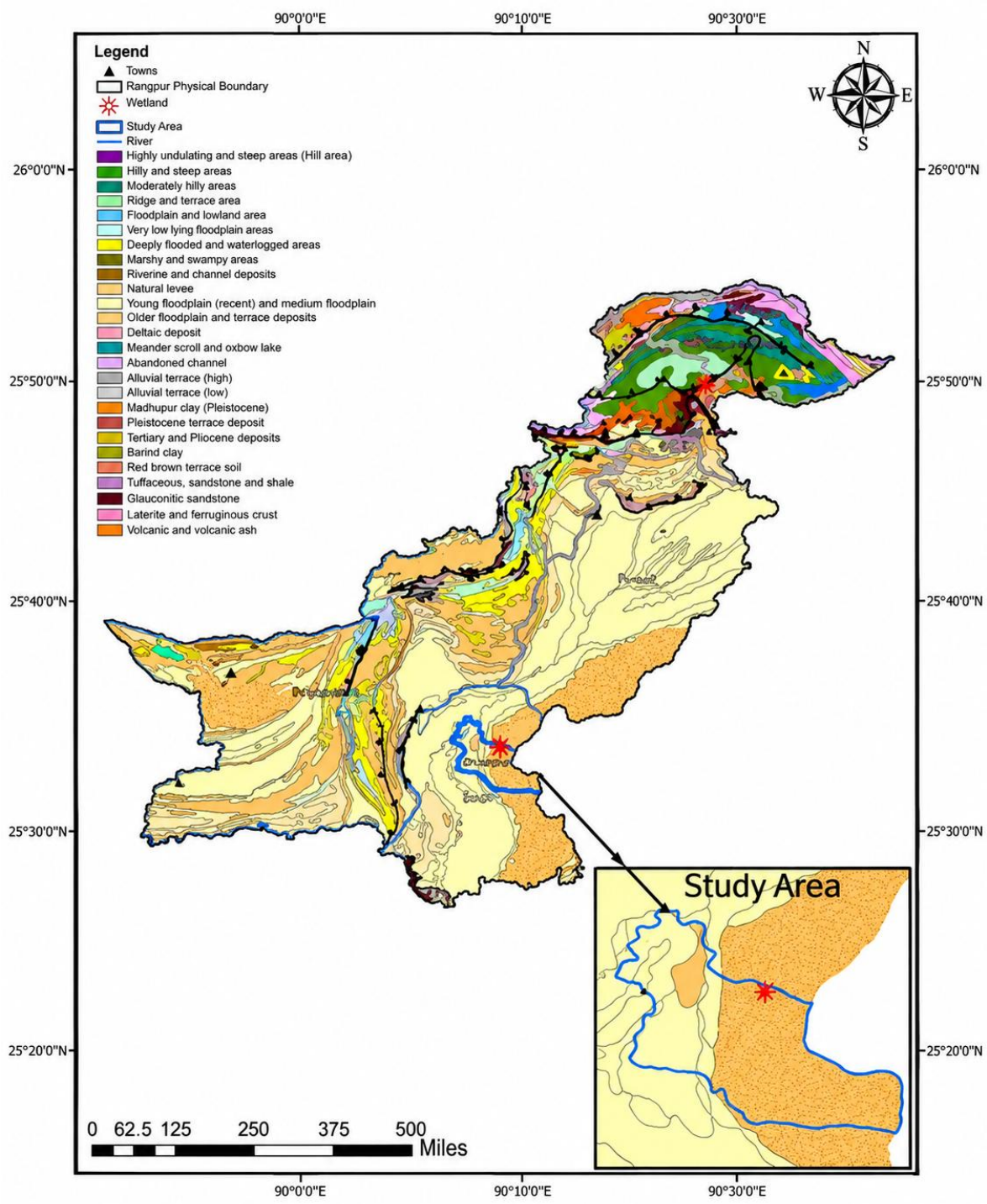



Figure 1. 1 Location of the Kadanwari Gas Field in Sindh Province, Lower Indus Basin, Pakistan, shown on the regional geological map with the study area inset (after Ali et al., 2019b).

## 1.4 Structural Framework of the Study Area

Published accounts agree that the present structure of the Kadanwari area records three tectonic episodes: uplift and erosion during the Late Cretaceous, expressed on seismic

sections as truncation at the base-Tertiary unconformity; wrench faulting during the Late Paleocene; and renewed uplift from the Late Tertiary to Recent associated with inversion of the Jacobabad–Khairpur High (Ahmad & Ghazi, 2022; Shah et al., 2024). The resulting fault system trends north-northwest to south-southeast and divides the Lower Goru reservoir into horst, graben and half-graben blocks (Khan et al., 2024; Shah et al., 2024).

The kinematic interpretation of this fault system is not settled. Several authors describe wrench-related deformation and flower-structure geometry in cross-section (Ahmad & Ghazi, 2022; Khan et al., 2023). Saif-Ur-Rehman et al. (2020), interpreting fourteen seismic lines across the Kadanwari and Miano fields, reached a different conclusion: they described the area as dominantly extensional, with tilted fault blocks of half-graben geometry arranged in a bookshelf pattern and produced by northwest–southeast extension related to the northward drift of the Indian Plate from Madagascar, and they reported that a wrench fault system is largely absent apart from a probable strike-slip fault at Kadanwari, with average fault displacement of about 50 m. Shah et al. (2024) modelled the faults as predominantly normal and observed that fault density and complexity are greatest in the central part of their seismic cube and decrease towards its margins, with the E-sand interval more strongly deformed than the G-sand.

For the purposes of this thesis the kinematic debate matters less than its shared consequence, but it is not without consequence altogether. On every published interpretation the reservoir is divided into discrete fault blocks and reservoir units are placed against non-reservoir units across fault planes, and that makes juxtaposition analysis relevant. Whether those faults formed under simple extension or under wrench deformation nevertheless bears on how they behave as seals, because strike-slip movement produces fault-zone architectures, clay-smear continuity and stress states different from those of a purely dip-slip normal fault. The average displacement of about 50 m reported by Saif-Ur-Rehman et al. (2020) is moreover of the same order as the thickness of the individual Lower Goru sand units, so modest differences in throw change which units are placed against which. The disagreement in the literature is a source of uncertainty for containment, not a matter of structural nomenclature. The methods used to evaluate such configurations were established by Allan (1989), who introduced fault-plane sections on which the cutoffs of hanging-wall and footwall stratigraphy are projected to identify cross-fault juxtaposition and spill points, and were extended by Knipe (1997) through juxtaposition and triangle diagrams and by Yielding et al. (1997) through lithology-dependent attributes such as shale gouge ratio and shale smear factor. No published study has applied these methods at Kadanwari, although

Shah et al. (2024) identified the fault network as a possible pathway for the vertical migration of injected CO2.

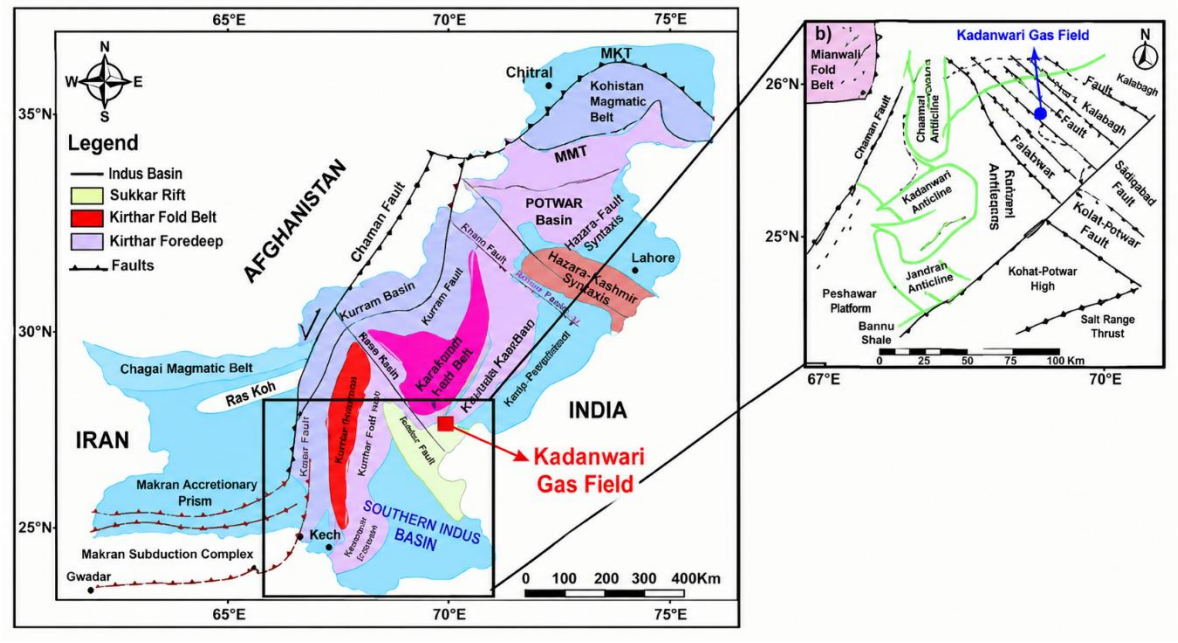



Figure 1. 2 Tectonic setting of the Kadanwari Gas Field, bounded by the Sulaiman Fold Belt to the north and the Sukkur Rift and Kirthar Foredeep to the south, with the structural elements of the platform (Khan et al., 2024).

## 1.5 Stratigraphy of the Lower Indus Basin

The stratigraphic succession of the Lower Indus Basin ranges from Triassic and Jurassic strata at depth through a thick Cretaceous section to Paleogene and Neogene cover (Kadri, 1995; Khan et al., 2024). Jurassic carbonates of the Chiltan Formation are overlain by the Cretaceous Sembar Formation and the Goru Formation, which together constitute the principal petroleum system of the platform. The Goru Formation is divided into a lower, sand-bearing part and an upper, shale-dominated part, and the succession is capped by the Parh, Mughal Kot and Pab units before the Paleocene and Eocene carbonates and clastics of the Ranikot, Dunghan, Ghazij and Kirthar groups, and finally the Neogene Nari, Gaj and Siwalik sequences (Khan et al., 2024).

The Lower Goru Formation is of Early Cretaceous age and comprises alternating sandstone and shale packages deposited by westerly prograding, river-dominated deltaic to shallow-marine systems draining the Indian Shield to the east and southeast (Raza et al., 2020). Ahmad et al. (2004) applied sequence stratigraphy as a predictive tool across the Lower Goru fairway of the Lower and Middle Indus platform, and Ahmad and Ghazi (2022) subsequently used a sequence-stratigraphic framework to describe depositional trends and

reservoir geometries within the formation. Raza et al. (2020) noted that successive reservoir units display a backstepping arrangement produced by overall relative sea-level rise, and that regressive sand bodies were subsequently flushed during transgressive episodes. The practical consequence of this depositional history is that reservoir quality varies both vertically, between stacked sand units, and laterally, through facies change and pinch-out.

A recurring difficulty in the Lower Goru literature is nomenclature. Different operators have applied different sand-unit schemes to the same succession, and Khan et al. (2024) tabulated the correlations between the classifications used by OGDCL, UTP, LASMO/ENI and OMV. This thesis follows the ENI scheme, in which the Lower Goru sand units are labelled B to H, because ENI operates the field. Where earlier studies use an alternative scheme, care is required before their reported values are compared with results expressed in ENI terms.

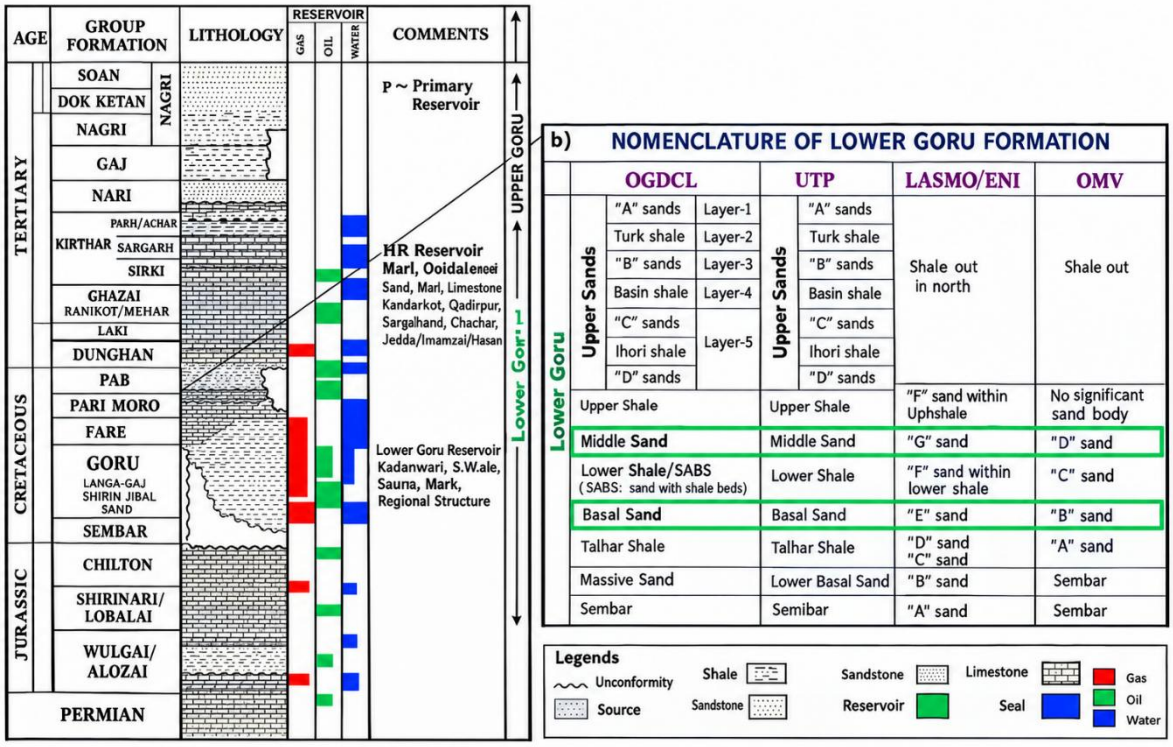



Figure 1. 3 Generalised stratigraphy of the Lower Indus Basin showing source, reservoir and seal intervals (a), together with the Lower Goru sand nomenclature adopted by different operators (b). The ENI scheme followed in this thesis is shown in the LASMO/ENI column (Khan et al., 2024).

## 1.6 Petroleum System of the Lower Indus Basin

The Sembar–Goru composite system is the dominant petroleum system of the Indus platform and supplies the reservoirs at Kadanwari, Miano, Sawan and neighbouring fields (Khan et al., 2024). Its elements are reviewed below, with attention to the properties that

### 1.6.1 Source Rocks

Organic-rich marine shales of the Early Cretaceous Sembar Formation are identified as the principal source rock for the Sembar–Goru play across the platform (Khan et al., 2024; Shah et al., 2024). Ahmad and Ghazi (2022) additionally reported that shales at deeper levels in the basin carry Type II–III kerogen with adequate maturity and total organic carbon, and act as an indigenous source. The gas-prone character of the charge is consistent with the dry to slightly wet gas produced at Kadanwari. Source-rock maturity is not directly relevant to storage capacity, but the source interval is relevant in two indirect ways: it constrains the burial and thermal history that shaped reservoir diagenesis, and it lies beneath the reservoir, so that the reservoir–seal pair rather than the source interval governs containment of anything injected.

### 1.6.2 Reservoir Rocks

The sand units of the Lower Goru Formation constitute the principal reservoir of the Indus platform and the producing interval at Kadanwari (Ahmad & Chaudhry, 2002; Khan et al., 2024). Reservoir quality is controlled jointly by depositional facies and by diagenesis. Baig et al. (2016) examined diagenetic controls on Lower Goru sandstone reservoirs of the Lower Indus Basin, and Berger et al. (2009) demonstrated at the nearby Sawan field that early diagenetic, grain-coating chlorite cements inhibited quartz overgrowth and preserved anomalously high porosity in Cretaceous volcaniclastic sandstones at reservoir temperatures near 175 °C and depths of 3000 to 3500 m. Because Kadanwari produces from the same formation at comparable depths, this mechanism is relevant to the interpretation of porosity there, although it has not been demonstrated at Kadanwari itself.

A second characteristic of the Lower Goru reservoir has direct methodological consequences. The producing sands are thin relative to seismic resolution and are interbedded with shales, which is why several studies at Kadanwari and elsewhere in the basin have concentrated on selecting inversion algorithms and attributes capable of resolving them (Ali et al., 2023; Shakir et al., 2022). The finding that bears most directly on the present work is a negative one: in the benchmark of Ali et al. (2023), model-based inversion did not

resolve the thin-bedded E sand clearly, whereas linear-programming sparse-spike inversion did. Any property model built from seismic data at Kadanwari inherits this limitation, and a study that adopts model-based inversion on these sands, as the present one does for the reasons given in Chapter 3, is obliged to treat the lateral variation of its result as better constrained than its absolute values and to say so.

### 1.6.3 Seal Rocks

Sealing in the Kadanwari play operates at two scales. Regionally, the transgressive shales of the Upper Goru Formation provide the top seal for the entire Sembar–Goru system (Khan et al., 2024; Shah et al., 2024). Locally, shale packages interbedded within the Lower Goru separate individual sand units and act as intraformational seals, so that the field contains several vertically stacked, hydraulically distinct reservoirs, not a single continuous one (Khan et al., 2024). The demonstrated retention of gas over geological time establishes that these seals have functioned. It does not, however, establish that they would perform identically for CO2, since capillary entry pressure depends on interfacial tension and wettability, and CO2-bearing brine is chemically reactive (Ali et al., 2019a; Bachu et al., 2007; Metz et al., 2005). Seal evaluation for storage therefore requires assessment in its own terms, not inference from the hydrocarbon accumulation. That assessment has not been made here. No measurement of capillary entry pressure, mineralogy or thickness continuity has been published for the Upper Goru shale at Kadanwari, so the regional seal is at present asserted from the presence of the accumulation, not characterised, and the same is true of the intraformational shales on which compartment-scale containment depends.

### 1.6.4 Traps and Hydrocarbon Migration Pathways

Trapping at Kadanwari combines structural and stratigraphic elements. Ahmad and Chaudhry (2002) recorded that the field was initially interpreted as a relatively simple four-way closure with continuous sand, and that development drilling and early production showed this model to be wrong: reserves were revised downward substantially and the reservoir proved to be strongly compartmentalised. Khan et al. (2024) described trapping as a combination of structural closure and stratigraphic loss of reservoir quality by lateral pinch-out, with the north-northwest to south-southeast horst and graben system compartmentalising the reservoir facies. In the same study, low values of the frequency attribute below about 10 Hz along faulted zones were interpreted as indicating trapped gas-bearing sands. That inference is plausible but not unique, since low-frequency shadows can also arise from

attenuation, from tuning, or from processing, and it is offered without independent calibration; it is best read as consistent with fault control on accumulation, not as evidence of it.

This makes the faults the central question for both migration and containment. Under the model of Allan (1989), a fault is neither inherently a seal nor a conduit; its effect depends on the rock properties juxtaposed across it and on the attitude of the juxtaposed blocks, so that cross-fault and synclinal spill points define the limits of trapping and the paths of vertical migration. Knipe (1997) and Yielding et al. (1997) developed this into a workflow in which juxtaposition is assessed first and fault-rock capacity second. Shah et al. (2024) noted that the Kadanwari faults compartmentalise the reservoir and could serve as pathways for CO2 migration, and recommended that future work address leakage risk and fault reactivation, but did not carry out juxtaposition analysis. The trapping configuration at Kadanwari is described in the literature but not tested against the criteria that storage assessment requires.

## 1.7 Geological and Petrophysical Characteristics of the Kadanwari Gas Field

Several studies have reported petrophysical properties for Kadanwari, but they used different wells, different intervals, different methods and different cut-offs. The values summarised below should be read as a range of published estimates, not as agreed field averages. A second limitation runs through all of them. The published petrophysical work concentrates on the E and G sands, which are the producing units, and reports almost nothing for the B sand at the base of the succession, which is the interval assessed in this thesis. Where a figure below is quoted for a different unit it is identified as such, and none of the values reported can be transferred to the B sand without the fresh petrophysical evaluation carried out in Chapter 4.

### 1.7.1 Reservoir Lithology

The reservoir consists of Lower Goru sandstones interbedded with shales. Under the ENI classification the sand units are labelled B to H; the main gas-bearing units in the study area are the E and G sands, with production also reported from the D and F units in some wells (Raza et al., 2020). Lithological discrimination in published work is based principally on the gamma-ray response. Shah et al. (2024) classified gamma-ray values above 80 API as shale facies, values between 50 and 80 API as shaly sand, and values below 50 API as sand, and used the gamma-ray index to compute shale volume. Khan et al. (2024) used facies modelling to distinguish clean sand from intermixed sand–shale reservoir zones, and reported that gas-bearing sands appear on the neutron–density crossplot with low bulk

density below about 2.3 g/cm3. Regionally, Lower Goru sandstones of equivalent age at Sawan were described as feldspathic litharenites with abundant altered volcanic rock fragments (Berger et al., 2009), pointing to a volcaniclastic component in the sediment supply, although comparable petrographic work has not been published for Kadanwari.

### 1.7.2 Porosity

Porosity at Kadanwari has been estimated from logs, from seismic inversion and from geostatistical modelling. Ali et al. (2019b) interpreted thirteen reservoir zones across four wells over a depth range of 2886 to 3797 m and reported average effective porosities between 0.11 and 0.44 as fractional values. Khan et al. (2024) reported good porosity of about 12 per cent for the gas-bearing E-sand from the neutron–density crossplot, together with net pay of 14 m within that interval. Ahmad et al. (2007) predicted porosity from three-dimensional seismic inversion at the field, and Ali et al. (2023) compared five post-stack inversion algorithms for the delineation of the thin-bedded E-sand and its porosity, concluding that linear-programming sparse-spike inversion resolved the interval better than band-limited or coloured inversion, while maximum-likelihood sparse-spike and model-based inversion did not resolve it clearly. Shah et al. (2024) computed total porosity from the density log, arguing that the relatively uniform sandstone mineralogy of the Lower Goru makes the density log more reliable than the acoustic log for this purpose, corrected for shale volume to obtain effective porosity, and distributed the result by sequential Gaussian simulation; their models showed porosity increasing towards the central faulted zone of the field.

The spread between these figures is wide, and part of it reflects genuine differences of method and target, not disagreement about the rock: values derived from different wells, different sand units, different porosity transforms and different shale-volume corrections are not directly comparable. Part of it, however, should not be accepted at face value. An effective porosity of 0.44 in a sandstone at more than 3,000 m of burial is not physically credible, and the upper end of the range reported by Ali et al. (2019b) is more likely to reflect a reporting or unit convention than a measured pore fraction; a figure of that order cannot be carried into a capacity calculation. What a storage assessment requires is the effective porosity of a defined interval within a defined fault block, computed on a stated basis and reported with the well and depth from which it comes, and no published figure for Kadanwari meets that description for the B sand.

### 1.7.3 Permeability

Permeability is the least well constrained of the reservoir properties at Kadanwari, because published work has not had access to core measurements. Ali et al. (2019b) reported permeability ranging from approximately 10.5 to 477.8 mD across the interpreted zones. Shah et al. (2024) stated explicitly that in the absence of core data they used a Wyllie–Rose type empirical relation, computing permeability from total porosity and irreducible water saturation, and then simulated the result across the model grid. Permeability at the field is therefore a derived quantity rather than a measured one, and its uncertainty propagates into any statement about injectivity. This matters more for storage than for production assessment, because injectivity determines the rate at which CO2 can be emplaced and the pressure response of the reservoir, and because a permeability field inferred from a porosity transform cannot capture the effect of shale interbeds and fault-related barriers on flow. There is a further difficulty in treating such a field as evidence. Since the Wyllie–Rose form computes permeability from porosity and irreducible water saturation, the permeability model is a monotonic re-expression of the porosity model, not an independent measurement: agreement between the two carries no confirmatory weight. The spatial pattern of predicted permeability is the spatial pattern of predicted porosity. Statements about injectivity at Kadanwari rest on a transform whose coefficients have never been calibrated against core from the field.

### 1.7.4 Fluid Saturation

Water saturation at Kadanwari has consistently been computed using the Indonesian equation instead of the Archie relation, because the Lower Goru sands contain thin interbedded shales that render the clean-sand assumption invalid (Ali et al., 2019b; Shah et al., 2024). Ali et al. (2019b) reported average water saturations between 0.18 and 0.45 and hydrocarbon saturations between 0.59 and 0.86 across the interpreted zones, with water saturation below 60 per cent in each of the four wells examined. Khan et al. (2024) reported gas saturation of approximately 68 per cent within the 14 m net pay of the E-sand. Shah et al. (2024) treated low water saturation as favourable for storage, on the reasoning that it indicates pore space not already occupied by formation water.

These values need two qualifications before they are used in a storage assessment. First, saturation in a producing field is not static: gas is withdrawn and water may encroach, so saturations reported from wells logged at different times describe different states of the

reservoir. Second, the quantity that governs how much CO2 a pore volume can actually accept is not the in-place hydrocarbon saturation but the irreducible water saturation together with the storage efficiency factor, which is why capacity formulations treat these terms separately (Bachu et al., 2007; Shah et al., 2024). A third qualification concerns the inputs to the calculation itself. The Indonesian equation requires the tortuosity, cementation and saturation exponents together with the formation water resistivity, and published work at Kadanwari adopts standard sandstone values for the exponents instead of deriving them from core, so the reported saturations carry a systematic uncertainty that is not quantified in addition to the differences of well and interval already noted.

## 1.8 Problem Statement

Evaluating a depleted field for CO2 storage requires knowing how much accessible pore volume it holds and whether that volume is sealed. At Kadanwari neither is established. The Lower Goru sands are laterally and vertically heterogeneous and divided by a north-northwest to south-southeast fault system into horst and graben compartments (Khan et al., 2024), so porosity, density, lithology, permeability and saturation measured in one fault block cannot be assumed to represent another. Well logs quantify these properties precisely, but only at discrete well locations. Seismic data cover the field, but respond to elastic contrast, not to porosity or saturation, and resolve the thin Lower Goru sands poorly (Ali et al., 2023). Neither dataset alone can describe the reservoir volume, which is why well- and seismic-derived properties must be integrated. The bounding faults compound the problem: they create the closures that trapped gas, yet they also juxtapose reservoir against non-reservoir and have been identified as possible migration pathways for injected CO2 (Shah et al., 2024). Whether they seal can be tested only by juxtaposition analysis, not inferred from structure maps (Allan, 1989). This thesis addresses that absence. It assesses storage potential rather than assuming it.

## 1.9 Research Gap

Work at Kadanwari has been directed almost entirely at hydrocarbons: field development history (Ahmad & Chaudhry, 2002), seismic inversion for porosity and thin-bed delineation (Ahmad et al., 2007; Ali et al., 2023), petrophysical evaluation and reservoir-zone prediction (Ali et al., 2019b; Ali et al., 2022; Khan & Khan, 2018), structural interpretation (Saif-Ur-Rehman et al., 2020), and integrated hydrocarbon assessment (Khan et al., 2024). Storage has been addressed once. Shah et al. (2024) estimated the CO2 storage

potential of the interval between the G- and E-sands from three-dimensional structural and petrophysical modelling, distributing properties by sequential Gaussian simulation over a small seismic cube and three wells. Three gaps remain. First, containment is untested: Shah et al. (2024) identified the faults as possible CO2 migration pathways and left leakage and fault reactivation to future work, and no Kadanwari study has performed juxtaposition or Allan-diagram analysis of the bounding faults (Allan, 1989; Knipe, 1997). Second, no storage assessment at the field has derived reservoir properties from seismic inversion combined with machine-learning attribute transforms; that combination has been applied in Pakistan only at Qadirpur, in a carbonate reservoir (Razaq et al., 2025). Third, the existing estimate covers a single interval within a small cube and has not been tested across the wider field or against an independent dataset. These three gaps map directly onto the objectives of this thesis.

## 1.10 Research Objectives

The objectives of this research, as approved in the thesis proposal, are:

1. To interpret seismic and well data to identify subsurface structures, identify reservoir interval and estimate key reservoir properties
2. To predict and validate the reservoir attributes using machine-learning algorithms to further incorporate in inversion process.
3. To assess the sealing capacity of the reservoir through fault seal analysis, and to estimate storage capacity in Kadanwari gas field.

## 1.11 Research Questions

The research questions correspond directly to the three approved objectives stated in Section 1.5:

1. What subsurface geological structures and reservoir zone can be identified from the integrated interpretation of seismic data and well logs at Kadanwari, and what are the key reservoir properties, including porosity, density and lithology, of that zone?
2. What is the sealing integrity of the subsurface reservoir when evaluated by triangular/juxtaposition fault seal analysis?
3. Can machine-learning techniques calculate and predict the porosity and permeability models, density and saturation, and thereby demarcate on the seismic data the potential reservoir zone initially identified from the well data?

## 1.12- Research Significance

The significance of this research operates at several levels, and it is stated here in terms proportionate to what the study actually undertakes.

For geological carbon-storage research, the thesis contributes a property-based assessment of a mature onshore gas field in a compartmentalised clastic reservoir. Such settings are common among candidate storage sites worldwide but are more difficult to evaluate than laterally continuous saline formations, because capacity and containment are both governed by fault geometry as much as by rock properties. By treating fault juxtaposition as an explicit object of analysis instead of a boundary condition, the study addresses a component of storage assessment that is frequently identified as a source of uncertainty and less frequently quantified (Allan, 1989; Yielding et al., 1997).

For subsurface characterisation and petroleum geophysics, the study applies an integrated well-and-seismic workflow to a question other than hydrocarbon prospectivity. The methods employed, structural interpretation, petrophysical evaluation, model-based seismic inversion and machine-learning prediction of reservoir properties from inverted impedance, are established in reservoir characterisation, but their combination in a storage requires different interpretive criteria: reservoir quality is assessed for injectivity and pore volume, not for producible hydrocarbon, and the seal is evaluated for its capacity to retain a buoyant, chemically reactive phase over long timescales. Demonstrating that the workflow transfers to this question, and identifying where it does not, has methodological value independent of the specific result obtained.

For the understanding of the Kadanwari Gas Field, the study extends the existing knowledge base in two directions. It provides an independent assessment of storage-relevant reservoir properties from a two-dimensional seismic grid covering the field, rather than from the three-dimensional cube used by Shah et al. (2024), and it does so for a different reservoir interval; it also supplies the fault-seal evaluation that earlier work identified as necessary but did not perform.

For carbon-storage research in Pakistan, the study adds to a small evidence base. Field-scale geoscientific assessments in the country remain few, and national estimates rest largely on regional-scale approximations (Holloway et al., 2009). Systematic evaluation of individual mature fields, using data that already exist, is a prerequisite for any future ranking of candidate sites, and the workflow developed here is transferable to other Lower Goru fields of the Indus Basin and, with modification, to other reservoir types.

The limits of these contributions should be stated as clearly as the contributions themselves. It is not a feasibility study for a CCS project. It does not demonstrate commercial viability, does not establish injectivity through dynamic simulation or well testing, does not model plume migration or pressure evolution over time, does not evaluate wellbore integrity across the field's existing penetrations, does not assess geomechanical risk or the potential for fault reactivation under injection, and does not establish long-term storage security or the absence of leakage. A favourable outcome would indicate that the field warrants further, more detailed investigation; it would not indicate that CO2 can be injected safely or economically.

### 1.13- Thesis Outline

Chapter 1 – Introduction sets out the background to the study. It explains why geological carbon storage matters, why depleted hydrocarbon reservoirs are good places to store $CO_2$, and which reservoir properties decide whether a site is suitable. It then introduces the Kadanwari Gas Field and its geology, describes the research problem and the gap this study fills, and lists the objectives and research questions. It ends with the significance of the work and the limits of its scope.

Chapter 2 – Literature Review covers the published work this study builds on. It starts with the geology of the Lower Indus Basin: its structure, stratigraphy and petroleum system. It then reviews what has been reported on the geology and petrophysics of Kadanwari, and how those results were obtained. After that it looks at geological carbon storage and at how well and seismic data are used to assess it, and it considers earlier reservoir characterisation studies in the basin and elsewhere in Pakistan. The chapter closes by drawing this work together and showing where the gap lies.

Chapter 3 – Methodology describes the data and how they were analysed. It lists the 2D seismic lines, the wells and their logs, the navigation and formation-top data, and the software used. It then works through each step of the workflow in turn: petrophysical evaluation of shale volume, porosity and water saturation; structural interpretation, the seismic-to-well tie, and time and depth mapping; model-based seismic inversion; machine-learning prediction of reservoir properties from the inverted impedance; fault-seal analysis by juxtaposition; and volumetric estimation of storage capacity.

Chapter 4 – Results and Interpretation presents what each step produced and what it means. It covers the petrophysical results at the three wells, the well ties, the interpreted seismic sections, and the time and depth structure maps. It then covers the inversion results

along the well-tied lines and the reservoir properties predicted from them, the fault-seal assessment of the main bounding fault, and the storage capacity of the closures mapped on the B sand. The uncertainty at each stage is stated as it comes up.

Chapter 5 – Discussion and Conclusions brings the findings together and considers what they mean for $CO_2$ storage in the B sand at Kadanwari. It then sums up the conclusions against each research objective.

# CHAPTER 2
# LITERATURE REVIEW

This chapter reviews the literature that underpins the assessment of subsurface carbon-storage potential at the Kadanwari Gas Field. Literature review draws geological and petrophysical characteristics of Kadanwari itself, with attention to how reported values were obtained and how consistent they are. And review geological carbon storage as a subject, the role of well and seismic data in assessing it, and the operational and field-scale studies that define current practice. And also examines previous reservoir-characterisation work in the Indus Basin and in Pakistan more widely, and synthesises the review and relates it to the research gap and objectives set out in Chapter 1. Throughout, a distinction is maintained between properties that published work has measured, properties it has estimated from empirical relations, and properties that remain unconstrained, because that distinction determines how much weight the present assessment can place on existing results. The review is selective in one further respect. Almost all published work at Kadanwari concerns the E and G sands, which are the producing units, whereas the interval assessed in this thesis is the B sand at the base of the Lower Goru succession; where a result is quoted for a different unit the difference is stated rather than smoothed over.

## 2.1 Literature Review

Geological carbon storage is the injection of CO2 into porous and permeable rock at depths sufficient for the CO2 to exist as a dense supercritical phase, generally below about 800 m, where a given pore volume accommodates a much larger mass than would be possible at shallower depths (Bachu, 2003; Metz et al., 2005). Retention arises from four mechanisms operating over different timescales: structural and stratigraphic trapping beneath a low-permeability seal, residual or capillary trapping of disconnected CO2 within the pore network, dissolution into formation brine, and mineral trapping through reaction with the rock matrix (Metz et al., 2005). Security generally increases with time as the more permanent mechanisms take effect.

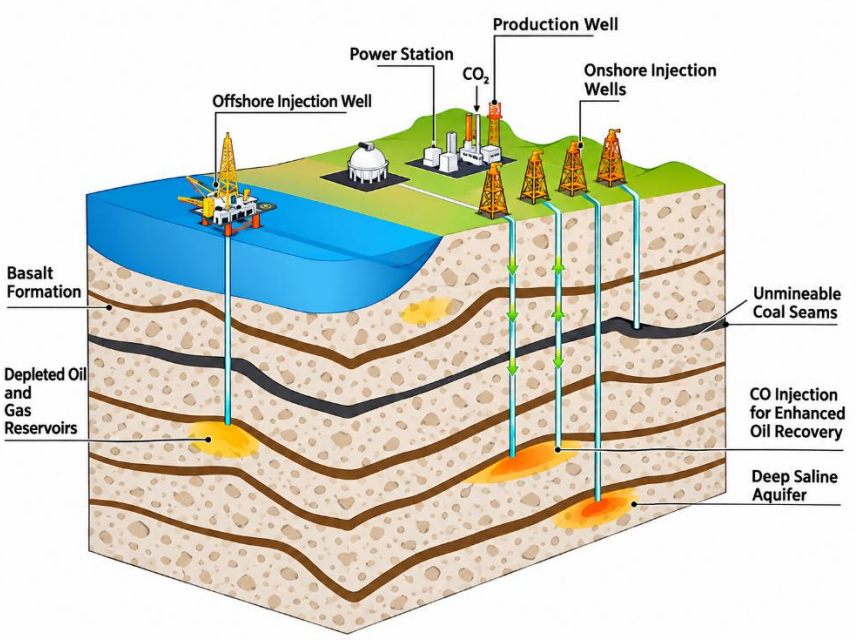



Figure 2. 1 Principal geological storage options for CO2, comprising depleted oil and gas reservoirs, deep saline aquifers, unmineable coal seams and basalt formations, with onshore and offshore injection configurations.

Candidate settings comprise deep saline formations, depleted oil and gas reservoirs, unmineable coal seams and basaltic formations, and review papers have compared their capacity, maturity and constraints (Bashir et al., 2024; Yang et al., 2023). Saline formations offer the largest theoretical pore volume but are the least characterised. Depleted hydrocarbon fields are better documented and have demonstrated retention of buoyant fluids, and Yang et al. (2023) reviewed the growing set of storage projects that use them. Coal seams store CO2 by adsorption, and basalts by carbonate mineralisation. Hazarika et al. (2024) examined the pore structure of shale formations and reported that CO2 injection alters that structure, which is relevant both where shales are considered as storage media and where they act as seals.

Site evaluation and capacity estimation have an established methodological basis. Bachu (2003) developed a set of criteria for ranking sedimentary basins, showing among other things that warm basins are less favourable than cold basins because higher temperature reduces CO2 density and increases buoyancy. Bachu et al. (2007) set out the capacity framework now in general use, distinguishing theoretical capacity from effective capacity, which applies geological and engineering cut-offs, and from practical capacity, which additionally reflects regulatory and economic constraints; they also noted that capacity estimation in depleted fields proceeds from recoverable reserves, reservoir properties and in

situ CO2 characteristics. In practice the distinction is cited more often than it is observed. Published capacity figures, including those for depleted fields, are commonly reported as single numbers without stating which of the three categories they belong to or what storage efficiency factor was assumed, which makes them difficult to compare with one another; because the efficiency factor is not a measured quantity and can vary by an order of magnitude between settings, it is usually the dominant term in the uncertainty of any such figure.

Rock–fluid interaction is a further consideration that distinguishes CO2 storage from gas storage. Ali et al. (2019a) showed experimentally that exposure to traces of organic acids alters the CO2 wettability of sandstones, with consequences for capillary trapping efficiency and long-term retention. Mohamed and Nasr-El-Din (2013) found that CO2 interaction with carbonate rocks can increase permeability through dissolution in some cases while reducing injectivity through precipitation and heterogeneity in others, illustrating that geochemical response is not uniformly favourable or unfavourable. Vo Thanh et al. (2020) demonstrated that the geological modelling method chosen materially changes the storage assessment obtained for a given field, a reminder that capacity estimates are model-dependent.

Storage assessment reuses the datasets and much of the toolkit of petroleum reservoir characterisation, but applies different interpretive criteria. Wireline logs supply shale volume, porosity, bulk density and water saturation along the borehole, and these are the quantities from which pore volume and, indirectly, injectivity are estimated. Razaq et al. (2025) and Shah et al. (2024) both built their storage assessments on conventional log suites of this kind. The difference from hydrocarbon evaluation lies in what the interpreter is looking for: high porosity and permeability remain desirable, but low water saturation is read as available pore space, not as producible hydrocarbon, and shale intervals are evaluated as potential seals instead of being dismissed as non-reservoir.

Seismic data contribute the spatial dimension. They define the geometry of the closure, the continuity of the seal and the position and throw of faults, all of which bear on containment. Through inversion they also yield impedance volumes from which reservoir properties can be estimated between wells. The Indus Basin literature provides a well-developed precedent for this: Ahmad et al. (2007) predicted porosity at Kadanwari from three-dimensional seismic inversion; Shakir et al. (2022) compared post-stack model-based and pre-stack simultaneous inversion attributes for the characterisation of thin gas-bearing sands and identified which attributes are most sensitive; and Ali et al. (2023) benchmarked five post-stack algorithms specifically on the thin-bedded Kadanwari E-sand. Khan et al.

(2023) applied Bayesian stochastic inversion with a petro-elastic relation to quantify thin gas sands at Zamzama, an approach that carries uncertainty explicitly.

Machine-learning methods extend inversion by relating multiple seismic attributes to log-derived properties. Razaq et al. (2025) used such approaches for petrophysical analysis, lithofacies prediction and impedance and effective-porosity estimation at Qadirpur, coupling the result with thermodynamic assesment and caprock evaluation to assess CO2 storage. Geostatistical simulation performs a complementary role by populating a three-dimensional grid and quantifying uncertainty: Shah et al. (2024) used sequential Gaussian simulation with 200 realisations at Kadanwari to derive a probabilistic pore volume and hence a probabilistic storage estimate. Comparable integrated workflows have been reported elsewhere, including sedimentological and petrophysical characterisation of the Bokabil Formation in the Surma Basin for storage capacity estimation (Hossain et al., 2024) and three-dimensional seismic and petrophysical modelling of the Amal field in the Gulf of Suez (Amer et al., 2025).

Fault-seal analysis is the component of this toolkit least often applied in storage studies, although its inputs are exactly the mapped horizons, fault surfaces and log-derived shale volumes that such studies already produce (Allan, 1989; Knipe, 1997; Yielding et al., 1997). The omission is hard to justify on grounds of data or effort, and it matters most in the settings where storage in depleted fields is most often proposed, since there the structures that create the closure also define the compartments and the possible migration paths. The limits of the method should be stated alongside its neglect: juxtaposition analysis establishes which units are placed against which and no more, and the fault-rock attributes that extend it were calibrated against hydrocarbon columns, so their transfer to a buoyant and chemically reactive phase such as CO2 is an assumption rather than a demonstrated result. A final distinction should be noted. Time-lapse seismic methods used to track a CO2 plume, such as those applied over two decades at Sleipner (Furre et al., 2017), belong to the monitoring phase that follows injection. The present thesis, like the studies reviewed above, addresses the prior stage of static characterisation, in which the question is whether a site merits consideration at all.

Operational projects supply the strongest evidence that geological storage functions at scale, and each has contributed a distinct lesson. At Sleipner in the Norwegian North Sea, CO2 separated from produced natural gas has been injected into the Utsira Sand since 1996 at a rate approaching one million tonnes per year; Furre et al. (2017) reviewed twenty years of monitoring, during which repeated time-lapse seismic surveys, supported by gravimetry,

imaged the growth and migration of the plume. Sleipner established both that a saline formation can retain injected CO2 and that geophysical monitoring can track it.

The In Salah project in central Algeria, by contrast, injected CO2 into a deep, thin and low-permeability Carboniferous sandstone, and Ringrose et al. (2013) documented the lessons drawn from it, including those arising from the geomechanical response of the reservoir and caprock system. In Salah demonstrated that injectivity and geomechanical behaviour, rather than pore volume alone, can determine whether a site performs as intended. Ringrose (2020) synthesised the experience of these and other early-mover projects into a general treatment of storage capacity, trapping, injection design and monitoring. At Gorgon on Barrow Island, Australia, naturally occurring CO2 separated from offshore gas is injected into the Dupuy Formation at approximately 2000 m; Yang et al. (2023) recorded that some 7 Mt had been injected since operations began in 2019, with more than 100 Mt anticipated over the life of the system.

Alongside these operating projects, a substantial body of field-scale assessment work exists for sites that have not been developed. Vo Thanh et al. (2020) assessed the E sequence of the Nam Vang field offshore Vietnam and showed the sensitivity of the result to the geological modelling method employed. Hossain et al. (2024) characterised the Bokabil Formation of the Surma Basin for storage capacity, and Amer et al. (2025) evaluated the depleted Amal field in the southern Gulf of Suez using integrated three-dimensional geological modelling, seismic interpretation and petrophysical analysis, identifying a fault-bounded horst block as the most favourable part of the structure. At the regional scale, Bachu (2003) provided the assesment framework and Holloway et al. (2009) applied a comparable logic to the Indian subcontinent. Taken together, these studies indicate that assessment of a candidate site proceeds through a common sequence: structural definition, petrophysical characterisation, property distribution with uncertainty, and evaluation of containment. The operational record is nevertheless a weaker analogue for Kadanwari than its prominence in the literature suggests. Sleipner and Gorgon inject into laterally extensive saline formations and In Salah into a single low-permeability sandstone unit; none of the three is a depleted, strongly compartmentalised, thin-bedded clastic gas field penetrated by numerous wells. What these projects establish is that storage works and can be monitored, not that it works in the setting considered here, and the lesson most directly transferable to Kadanwari is the negative one from In Salah, that pore volume alone does not determine whether a site performs as intended.

Reservoir characterisation in the Indus Basin is a mature field of study, and the Lower Goru Formation is among its most examined targets. At Kadanwari specifically, Ahmad and Chaudhry (2002) established the development history and the compartmentalised character of the reservoir; Ahmad et al. (2007) predicted porosity from three-dimensional seismic inversion; Khan and Khan (2018) and Ali et al. (2019b) evaluated the productive sands petrophysically; Ali et al. (2022) used petrophysical modelling to predict the Cretaceous reservoir zone; Saif-Ur-Rehman et al. (2020) interpreted the structural styles of the field and of neighbouring Miano; Ali et al. (2023) benchmarked post-stack inversion algorithms on the thin-bedded E-sand; and Khan et al. (2024) integrated seismic interpretation, attribute extraction, well-based facies modelling and petrophysical evaluation to assess hydrocarbon potential, reporting the discontinuity attribute as effective for resolving fault geometry and instantaneous amplitude and sweetness as effective for illuminating gas-bearing deposits.

Beyond Kadanwari, comparable work has been carried out across the basin. Azeem et al. (2017) combined petrophysical and rock-physics analysis to improve characterisation of Cretaceous sand intervals in the Middle Indus Basin. Shakir et al. (2022) characterised thin gas sands of the Lower Ranikot Formation at the Mehar gas field using sensitive post-stack and pre-stack inversion attributes. Khan et al. (2023) quantified thin gas sands of the Khadro Formation at Zamzama by Bayesian stochastic inversion. Raza et al. (2020) characterised the B-interval of the Lower Goru Formation in the Miano area, and Krois et al. (1998) documented model-driven exploration at Miano. On reservoir quality, Baig et al. (2016) addressed diagenetic controls in Lower Goru sandstones and Berger et al. (2009) established the porosity-preserving role of chlorite cements at Sawan. This body of work has produced a well-developed methodological base for the region, but its objectives are consistently those of hydrocarbon exploration and production.

Research focused on CO2 storage in Pakistan remains limited. Holloway et al. (2009) presented an early national-scale estimate, suggesting that the country's gas fields could provide approximately 1.6 Gt of CO2 storage capacity once depleted, with further potential in the saline formations of the Indus and Potwar basins. Fareed et al. (2023) simulated CO2 sequestration and its effect on enhanced gas and oil recovery in a fractured reservoir of the Eastern Potwar Basin. Razaq et al. (2025) assessed the Sui Main Limestone at Qadirpur using machine-learning reservoir characterisation, thermodynamic evaluation and caprock validation. At Kadanwari, the only field-scale storage assessment is that of Shah et al. (2024), who estimated the storage potential of the interval between the G and E sands through a probabilistic pore-volume calculation based on a small seismic cube and three wells. The

probabilistic nature of this estimate needs careful interpretation. The two hundred sequential Gaussian realisations reflect the variability produced by a single geological model and one set of variogram parameters, and therefore measure precision rather than accuracy. They do not account for uncertainty in the structural framework, in the porosity transform, or in the assumption that the bounding faults are sealing, and it is this last uncertainty that determines whether the estimated volume could be retained at all. Overall, these studies rely mainly on static evaluation, only one includes dynamic simulation, and none carries out an explicit fault-seal assessment.

# CHAPTER 3
# METHODOLOGY

## 3.1 Adopted Methodology

The methodology adopted in this research integrates two independent subsurface datasets, two-dimensional (2D) seismic reflection profiles and wireline logs, and converts them into the structural and reservoir properties required to assess carbon storage potential. The workflow is organised as two parallel streams that converge at later stages. In the seismic stream, the data are loaded, horizons and faults are interpreted, the interpretation is calibrated to the wells through a seismic-to-well tie, and time and depth structure maps are generated. In the well stream, petrophysical analysis is carried out to determine shale volume, porosity, permeability and water saturation, and these log-derived properties form the training data for the machine-learning prediction. The two streams are integrated at two stages. The first is model-based seismic inversion, in which the log-derived properties constrain the low-frequency component of the impedance model. The second is the machine-learning prediction, in which the relationship between inverted impedance and the log properties, established at the wells, is propagated along the well-tied seismic lines. The resulting property sections, together with the fault-seal evaluation, are then combined to estimate storage capacity. The complete workflow is presented in Figure 3.1.

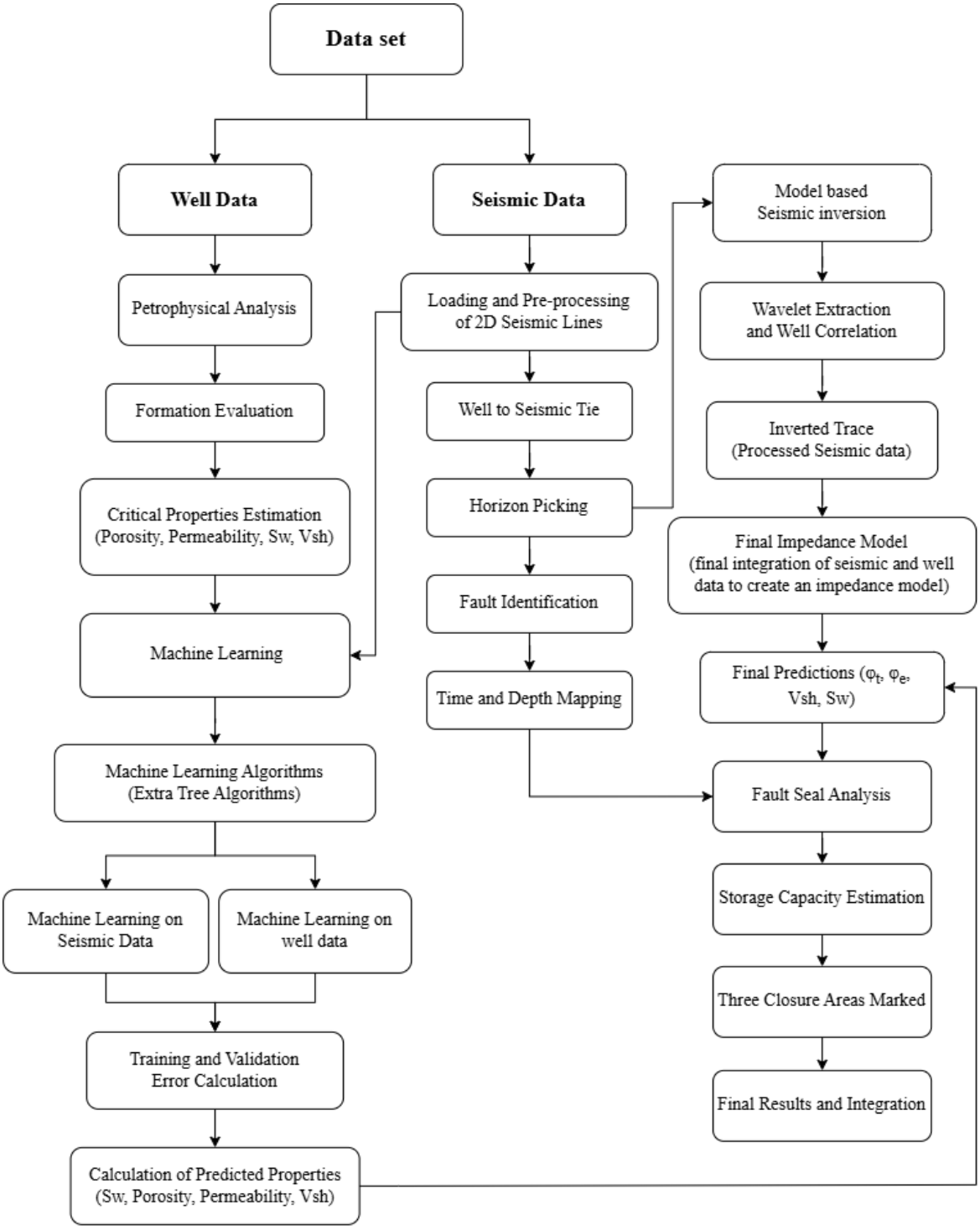



Figure 3. 1 Methodology Workflow

Five software environments were used, each for the task to which it is suited. Structural interpretation of the two-dimensional seismic lines, including horizon and fault picking, seismic-to-well tie, and time and depth structure mapping, was carried out in GVERSE Geophysics. Petrophysical evaluation of the wireline logs was carried out in GVERSE Petrophysics. Model-based seismic inversion was carried out in the Hampson-

Russell (HRS) software suite. The machine-learning prediction that follows it was carried out in Python using the scikit-learn library, the inverted impedance being exported from Hampson-Russell for that purpose. Keeping the interpretation, petrophysics and volumetrics within a single environment preserves a common project database, well header and datum definition, which reduces the risk of positional or datum inconsistencies when results from the inversion package are brought back into the structural framework.

## 3.2 Dataset

The dataset comprises two-dimensional seismic reflection profiles, digital wireline logs, navigation files and formation-top files for the Kadanwari Gas Field. Ten two-dimensional seismic lines were incorporated: TJ-88-207, TJ-89-510, TJ-89-512, TJ-89-516, TJ-89-518, TJ-89-520, TJ-89-522, TJ-89-524, TJ-89-526 and TJ-91-803 (Table 3.1). These lines form a grid across the field and provide dip and strike control across the north-northwest to south-southeast fault trend that compartmentalises the Lower Goru reservoir (Khan et al., 2024). Navigation files supply the surface geometry of each line, and formation-top files supply the stratigraphic control used to relate the seismic reflections to the Lower Goru sand units.

| **Seismic line** | **Well intersection** | **Analysis performed** |
|---|---|---|
| TJ-88-207 | — | Structural interpretation only |
| TJ-89-510 | — | Structural interpretation only |
| TJ-89-512 | Kadanwari-3 | Inversion and machine-learning prediction |
| TJ-89-516 | Kadanwari-1 | Inversion and machine-learning prediction |
| TJ-89-518 | — | Structural interpretation only |
| TJ-89-520 | — | Structural interpretation only |
| TJ-89-522 | — | Structural interpretation only |
| TJ-89-524 | — | Structural interpretation only |
| TJ-89-526 | Kadanwari-4 | Inversion and machine-learning prediction |
| TJ-91-803 | — | Structural interpretation only |

Table 3. 1 Two-dimensional seismic lines used in this study, their well control and the analysis carried out on each.

Three of these lines carry well control. Kadanwari-3 lies on line TJ-89-512, Kadanwari-1 on line TJ-89-516, and Kadanwari-4 on line TJ-89-526. Each of the three wells provides a log suite comprising gamma ray, resistivity, density, porosity, photoelectric factor and formation pressure test data. The remaining seven lines, TJ-88-207, TJ-89-510, TJ-89-518, TJ-89-520, TJ-89-522, TJ-89-524 and TJ-91-803, have no well intersection, so the interpretation on these lines is carried by correlation and three tied lines.

The stratigraphic coverage of the logs is not the same in all three wells. Upper Goru Formation is present and identifiable in all three wells and so provides the common correlation reference used throughout the interpretation. Within the Lower Goru, Kadanwari-1 is logged down to the B sand, Kadanwari-3 covers the section down to the H sand, and Kadanwari-4 reaches the top of the Lower Goru Formation without penetrating the individual sand units. The description of the B sand, which is the reservoir target of this study, is therefore constrained directly by Kadanwari-1, while the other two wells contribute the shallower correlation framework and the calibration of the seismic response above the target (Table 3.2).

| **Well** | **Seismic line** | **Log suite available** | **Stratigraphic coverage of the logs** |
|---|---|---|---|
| Kadanwari-1 | TJ-89-516 | Gamma ray, resistivity, density, porosity, photoelectric factor, formation pressure test | Upper Goru to Lower Goru B sand |
| Kadanwari-3 | TJ-89-512 | Gamma ray, resistivity, density, porosity, photoelectric factor, formation pressure test | Upper Goru to Lower Goru H sand |
| Kadanwari-4 | TJ-89-526 | Gamma ray, resistivity, density, porosity, photoelectric factor, formation pressure test | Upper Goru to top of Lower Goru; individual sands not penetrated |

Table 3. 2 Wells used in this study, the seismic lines on which they lie, the log suite available in each and the stratigraphic interval covered

The gamma-ray log provides volume of shale the discrimination of sand from shale facies. The resistivity log provides the formation resistivity required for water saturation. The density log provides bulk density, from which porosity is computed and which, with the

sonic response, generates the reflectivity series used in the seismic-to-well tie. The porosity log supports and cross-checks the density-derived porosity and, when cross-plotted against density, indicates gas-bearing intervals. The photoelectric factor log constrains lithology and confirms the matrix density adopted in the porosity calculation. Formation pressure test data provide the in-situ pressure information used in Section 3.8. All three wells supply training data for the machine-learning prediction of Section 3.6, and each is withheld in turn during cross-validation so that its logs serve as an independent check on a result they did not constrain.

First, the seismic coverage is two-dimensional, not a three-dimensional volume, so properties are resolved along the interpreted lines and are interpolated, not imaged, between them; mapped surfaces depend on the gridding algorithm in the inter-line areas, and seven of the ten lines are constrained only indirectly. Second, no core measurements are available, so porosity is derived from logs and permeability cannot be calibrated against laboratory data, a limitation that also applies to the previously published work on the field (Shah et al., 2024). Third, the recorded suite includes compressional but not shear sonic data, so no shear-derived elastic property is available. The inversion is therefore restricted to post-stack acoustic impedance, and the property prediction of Section 3.6 rests on that single elastic attribute rather than on the impedance pairs that a pre-stack inversion would supply. These constraints do not invalidate the assessment, but they define it as a preliminary assessment-level exercise and are carried through to the interpretation of results.

### 3.3 Petrophysical Analysis

Petrophysical analysis was performed in GVERSE Petrophysics and provides the quantitative description of the reservoir at each well. The logs were first loaded, depth-matched and conditioned: curve units and null values were checked, obvious washout intervals identified from the caliper and density-correction responses were flagged, and the analysis was restricted to the Lower Goru interval defined by the formation tops. Zonation followed the sand units of the ENI classification used by the field operator, in which the Lower Goru sands are labelled B to H. The units present at Kadanwari are, in stratigraphic order from the top downward, the H, E, D, C and B sands; the B sand is the lowermost of these and is the reservoir target selected for this study (Raza et al., 2020). Three properties were computed in sequence, since each depends on the one before: shale volume, porosity and water saturation.

### 3.3.1 Volume of Shale (Vsh)

Shale volume was estimated from the gamma-ray log, which responds to the naturally radioactive minerals concentrated in shales. The gamma-ray index is first computed as

$$I_{GR} = \frac{GR_{log} - GR_{min}}{GR_{max} - GR_{min}} \quad \text{(Asquith et al., 2004)} \qquad (3.1)$$

where GRlog is the recorded gamma-ray value at the depth of interest, and GRmin and GRmax are the minimum and maximum readings taken from clean sand and shale intervals respectively within the zone of interest (Asquith et al., 2004). Selecting these two end members is the principal judgement in the calculation, and they were picked from the histogram of the gamma-ray response within the Lower Goru interval instead of from the whole logged section, so that the baseline reflects the formation being evaluated.

The gamma-ray index was used as the estimate of shale volume, an approach consistent with previous work at Kadanwari, where gamma-ray thresholds have been used to separate sand, shaly sand and shale facies within the Lower Goru (Shah et al., 2024).

### 3.3.2 Porosity Estimation (φ)

Total porosity was computed from the average of density log, sonic log and neutron log, which is the more reliable basis for this formation because the Lower Goru reservoir consists of sandstones of relatively uniform mineralogy, and a single matrix density can be applied with confidence; the acoustic response, by contrast, is affected by texture and by fluid content (Shah et al., 2024). Density porosity is given by

$$\phi_D = \frac{\rho_{ma} - \rho_b}{\rho_{ma} - \rho_f} \quad \text{(Asquith et al., 2004)} \qquad (3.2)$$

where ρb is the bulk density recorded by the log, ρma is the matrix density and ρf is the density of the fluid occupying the pore space (Asquith et al., 2004). A sandstone matrix density was adopted, supported by the photoelectric factor log, which discriminates lithology and confirms a quartz-dominated matrix where the gamma ray indicates clean sand.

Total porosity was then corrected for the shale fraction to obtain effective porosity, which represents the interconnected pore space available to fluid and is therefore the quantity relevant to storage:

$$\phi_e = \phi_t(1 - V_{sh}) \quad \text{(Asquith et al., 2004)} \qquad (3.3)$$

Total porosity includes clay-bound water and overstates the volume accessible to an injected phase. Effective porosity is the value carried into the volumetric calculation of

Section 3.8. Because gas in the pore space suppresses the density-derived porosity less than it suppresses neutron porosity, the neutron and density curves were also cross-plotted to identify gas-bearing intervals, following the approach used at the field by Khan et al. (2024).

### 3.3.3 Water Saturation (Sw)

Water saturation was computed using the equation of Poupon and Leveaux (1971) in preference to the Archie (1942) relation. the Archie equation assumes a clean formation in which the rock matrix is non-conductive, whereas the Lower Goru sands at Kadanwari are interbedded with thin shales that provide an additional conductive path and cause the Archie equation to overestimate water saturation. This equation accounts for this shale conductivity explicitly and has been the model of choice in previous petrophysical work at the field (Ali et al., 2019b; Shah et al., 2024). It takes the form

$$\left(\frac{1}{R_t}\right)^{0.5} = \left[\frac{V_{sh}^{(1-V_{sh}/2)}}{(R_{sh})^{0.5}} + \left(\frac{\phi_e^m}{a \cdot R_w}\right)^{0.5}\right] \cdot S_w^{n/2} \quad \text{(Poupon \& Leveaux, 1971)} \qquad (3.4)$$

where Rt is the true formation resistivity from the deep resistivity log, Rsh is the resistivity of the adjacent shale, Rw is the formation water resistivity, φe is effective porosity, cementation and saturation exponents. Values appropriate to sandstone were adopted for the exponents, consistent with the parameters applied in previous Kadanwari studies (Shah et al., 2024). Formation water resistivity was established from the resistivity response in water-bearing intervals within the logged section. Hydrocarbon saturation follows as the complement of water saturation.

## 3.4 Structural Interpretation

Structural interpretation was carried out in GVERSE Geophysics and establishes the geometric framework within which the reservoir properties are subsequently distributed. Its purpose in a storage study is twofold: to define closure and the extent of the potential storage interval, and to map the faults whose sealing behaviour is examined in Section 3.7.

### 3.4.1 Data Loading

The seismic data were loaded in SEG-Y format and their trace headers verified against the navigation files, confirming that shot-point numbering, line geometry and coordinate system agree between the two. Line intersections were checked for consistency of reflection character and travel time, which is an essential quality check in a two-

dimensional (2D) survey because mis-tied intersections propagate directly into the mapped surfaces. Wireline logs were loaded in LAS format together with well headers giving surface coordinates, kelly bushing elevation and total depth, and the formation-top files were loaded to provide stratigraphic control. All data were referenced to a common datum and coordinate system before interpretation began. Polarity and phase were established from the well ties described below, not assumed from the header convention.

### 3.4.2 Seismic-to-Well Tie

The seismic-to-well tie converts the wells from the depth domain to the two-way time domain of the seismic data and is the step that gives the interpretation its stratigraphic meaning. A reflectivity series was computed from the product of the sonic and density logs, and convolved with an extracted wavelet to generate a synthetic seismogram at each well. The synthetic was then correlated with the seismic trace at the well location, and the time-depth relationship adjusted until an acceptable match of reflection character was obtained across the interval of interest. Bulk shifts and stretch or squeeze were applied conservatively and only where justified by the log response, since excessive manipulation produces an apparently good correlation that is not physically meaningful. Synthetic seismograms were generated at all three wells and used to position the three horizons carried through the interpretation. The Upper Goru and Lower Goru horizons were tied directly to the formation tops recorded in the wells; the Chiltan horizon lies below the logged intervals and could not be tied in the same way, so it was positioned by following the regional stratigraphic succession reported in the published literature. The resulting time-depth relationships serve three later purposes: they position the formation tops on the seismic sections, they provide the velocity control for the depth conversion of Section 3.4.5, and they supply the calibration between logs and seismic data required by the inversion of Section 3.5.

### 3.4.3 Fault and Horizon Marking

Faults were identified on the seismic sections from reflector discontinuities showing a consistent sense and amount of displacement, and were correlated between lines using their trend and throw. The interpreted faults are normal; faults the system trends north-northwest to south-southeast and divides the reservoir into horst and graben blocks, consistent with published interpretations of the field (Khan et al., 2024; Saif-Ur-Rehman et al., 2020; Shah et al., 2024). Fault polygons were generated for each mapped horizon so that the mapping honours the discontinuities.

Horizons were then picked on the reflections corresponding to the Lower Goru reservoir units identified at the wells, with the formation tops projected onto the seismic sections through the time-depth relationships established in Section 3.4.2. Three horizons were carried across the grid: the Upper Goru Formation, which provides the shallow correlation reference and is present in all three wells; the B sand of the Lower Goru Formation, which is the reservoir target of this study; and the Chiltan Formation, which was taken as the basal horizon of the interpretation. Picking proceeded from lines with well control outward to lines without it, and loop ties were closed around the grid so that each horizon is internally consistent. Where a reflection could not be followed with confidence across a fault, the pick was terminated at the fault and not forced across it, since a forced correlation would suppress precisely the compartmentalisation that this study seeks to characterise.

### 3.4.4 Time-Structure Mapping

The interpreted horizon picks were gridded to produce time-structure maps in two-way travel time, using the fault polygons as internal boundaries so that displacement across faults is preserved as a discontinuity in the mapped surface. Grid increment and search radius were selected with reference to the line spacing; because control exists only along the interpreted lines, the maps are best constrained near the lines and progressively less so between them. The time-structure maps identify the culminations and closures of the reservoir horizons and show how these are segmented by the fault system.

### 3.4.5 Depth-Structure Mapping

Time-structure maps cannot be used directly for volumetric calculation, because vertical distances in time are not proportional to distances in depth where velocity varies. The time-structure maps were therefore converted to depth using a velocity model built from the time-depth relationships derived at the three wells during the seismic-to-well tie. The resulting depth-structure maps give the true structural configuration of the reservoir horizons and provide two inputs used later: the closure area and gross thickness required for the volumetric estimation of Section 3.8, and the horizon cut-off depths on either side of each fault required for the juxtaposition analysis of Section 3.7. The accuracy of the depth conversion is limited by the number of wells available to constrain the velocity field, and this is treated as a source of uncertainty in the volumetric result, not as an exact conversion.

## 3.5 Machine Learning

Inversion returns acoustic impedance, but the properties a storage assessment requires are shale volume, porosity and water saturation. Machine learning bridges that gap. A regression model is trained at the wells on the relationship between inverted impedance and the log properties computed in Section 3.3, and the trained model is then applied trace by trace along the seismic lines, which yields a property estimate at every trace instead of one that is assumed. Predicting log properties from seismic data in this way is long established (Hampson et al., 2001), and tree-based ensemble methods have since been shown to suit the problem, because the relationship between an elastic property and a petrophysical one is seldom linear and is not known in advance (Priezzhev et al., 2019; Zou et al., 2021). The algorithm used here is Extra Trees regression, implemented in Python using the scikit-learn library (Pedregosa et al., 2011).

The predictor is the inverted P-impedance of Section 3.5. Because impedance is the product of density and compressional velocity it responds jointly to lithology and porosity, and in the Lower Goru the porous sands are expected to appear as impedance lows against the interbedded shales (Ali et al., 2023). It is therefore a physically meaningful predictor rather than an arbitrary one, which matters because the algorithm itself imposes no functional form on the relationship it learns. Four properties were predicted from it, each taken from the petrophysical analysis of Section 3.3 at the three wells: shale volume, total porosity, effective porosity and water saturation. A separate model was trained for each, so that four independent transforms of the form Y = f(Zp) were established instead of a single multi-output model.

### 3.5.1 Extra Trees Regression

Extra Trees, or extremely randomised trees, is an ensemble method that grows a large number of regression trees and averages their predictions (Geurts et al., 2006). A single regression tree partitions the training data by repeatedly splitting on threshold values of the predictor: the samples at a node are divided according to whether impedance falls above or below a cut-point, and the division continues until a stopping condition is reached, at which point each terminal node carries the mean of the target values of the samples remaining within it (Breiman et al., 1984).

What distinguishes Extra Trees from a conventional decision tree, and from a random forest, is the way that cut-point is chosen. Rather than searching every candidate threshold

for the one that best separates the data, the algorithm draws candidate cut-points at random from a uniform distribution spanning the range of the predictor present at the node,

$$C \sim U\left(Z_{p,min},\, Z_{p,max}\right) \quad \text{(Geurts et al., 2006)} \qquad (3.6)$$

and retains the best of those candidates according to the splitting criterion. The criterion adopted here is the reduction in squared error, which judges a split by how far it reduces the spread of target values within the resulting groups:

$$MSE = \frac{1}{n}\sum_{i=1}^{n}(Y_i - \bar{Y})^2 \quad \text{(Breiman et al., 1984)} \qquad (3.7)$$

where n is the number of samples in the group, Yi is an observed target value and $\bar{Y}$ is their mean. Randomising the cut-point makes each individual tree a weaker predictor than one grown by exhaustive search, but it also leaves the trees far less correlated with one another, and averaging over a decorrelated ensemble reduces variance by more than the loss of individual accuracy costs (Geurts et al., 2006; Hastie et al., 2009). The prediction of the ensemble is the mean of the individual trees:

$$\hat{Y} = \frac{1}{B}\sum_{b=1}^{B} T_b\left(Z_p\right), \quad b = 1,2,\ldots,B \quad \text{(Geurts et al., 2006)} \qquad (3.8)$$

where B is the number of trees and Tb(Zp) is the prediction returned by the bth tree. This behaviour is the reason the method was selected for the present dataset. Training samples are drawn from three wells only, and a flexible non-linear model fitted to so small a sample will otherwise reproduce the noise in the logs along with the signal; the averaging inherent in the ensemble suppresses that noise without requiring the form of the relationship to be specified beforehand (Breiman, 2001).

### 3.5.2 Machine Learning on Seismic Data

The seismic data carry the prediction beyond the wells. Each trained model was applied trace by trace to the inverted P-impedance along lines TJ-89-512, TJ-89-516 and TJ-89-526. This gives a property estimate at every trace. Prediction is confined to these lines because the impedance is calibrated only at wells.

### 3.5.3 Machine Learning on Well Data

The wells supply the training data. Inverted impedance was paired sample by sample with the log-derived shale volume, porosity and water saturation over the Lower Goru interval. A separate Extra Trees model was fitted to each of the four properties. Each well was withheld in turn as a blind test.

### 3.5.4 Training, Prediction and Validation

Training pairs were assembled at the three wells by co-locating the inverted impedance with the log-derived property at the same sample, over the analysis window spanning the Lower Goru interval. The trained models were then applied along the three well-tied lines, TJ-89-512, TJ-89-516 and TJ-89-526, to produce predicted sections of shale volume, total porosity, effective porosity and water saturation. Prediction is confined to these lines for the same reason as the inversion of Section 3.5: the impedance that drives it can only be calibrated where log control exists.

Performance is judged on data the model has not seen, since a sufficiently flexible model will reproduce its training data whether or not it has learned anything that generalises. Each well was accordingly withheld in turn, the model retrained on the remaining wells, and its prediction at the withheld well compared with the logs recorded there, a blind test, not a check at a well that helped constrain the result (Kohavi, 1995). Agreement was measured by the coefficient of determination,

$$R^2 = 1 - \frac{\sum_{i=1}^{n}(Y_i - \hat{Y}_i)^2}{\sum_{i=1}^{n}(Y_i - \bar{Y})^2} \quad \text{(Hastie et al., 2009)} \qquad (3.9)$$

in which a value approaching unity indicates close agreement between the predicted and the observed values, together with the root-mean-square error, which retains the units of the property predicted and is easier to weigh against the accuracy expected of the log itself. Because the predictions derive directly from the inverted impedance, this comparison also serves as an independent check on the inversion of Section 3.5: agreement between the predicted and the measured properties supports the interpretation that the inverted impedance carries reservoir information, not an artefact of the low-frequency model.

The prediction has two limitations, and both bear on how the results are interpreted. First, three wells is a small training set, so the withheld-well test is a demanding one, and a modest coefficient of determination should not by itself be read as a failure of the method. Second, a tree ensemble predicts by averaging observed target values and cannot extrapolate beyond the range of impedance encountered in training; where the inverted section carries

values outside that range the prediction flattens at the limit of the training data instead of continuing to trend, and such intervals were treated as unconstrained. The predicted effective porosity is the property carried into the pore-volume calculation of Section 3.8, and it is used quantitatively only within the calibrated impedance range.

### 3.5.5 Limitation

Machine learning was used to estimate shale volume, porosity, water saturation, and permeability. However, the reliability of the predicted properties is influenced by the quality and availability of the input data. The well data were not equally consistent throughout the study area, and some datasets showed skewness or variability that could affect the learning process. In addition, some wells contained good-quality and effective logs, whereas other intervals had missing, noisy, or less reliable log responses. These differences in data quality introduced uncertainty into the machine-learning predictions, and therefore, the estimated properties should be considered as approximate representations rather than exact measurements. To improve the interpretation, the machine-learning results were integrated with the seismic inversion results, which provide a continuous subsurface representation based on seismic data and well constraints. The comparison between the two approaches helped identify the major trends and distribution of the reservoir properties and provided additional support for the interpretation where well control was limited. Therefore, the combined use of machine learning and seismic inversion provides a more comprehensive understanding of the spatial variation of reservoir properties than relying on well data alone.

## 3.6 Model-Based Seismic Inversion

Seismic inversion converts the reflectivity recorded by the seismic data into a layer property, acoustic impedance, which relates more directly to rock properties than reflection amplitude does. Impedance is the product of density and compressional velocity,

$$Z_p = \rho \cdot V_p \quad \text{(Russell \& Hampson, 1991)} \qquad (3.5)$$

The model-based approach was adopted, in which an initial impedance model built from the well logs and the interpreted horizons is iteratively perturbed, forward-modelled by convolution with the extracted wavelet, and compared with the recorded seismic trace until the misfit is minimised (Russell & Hampson, 1991). This approach was selected because it incorporates the low-frequency component that the seismic data do not record and which is essential if absolute rather than relative impedance is required for property estimation. Inversion of the Lower Goru sands is not trivial: the reservoir units are thin relative to seismic

resolution, and Ali et al. (2023) showed at this field that the choice of algorithm materially affects whether the B-sand is resolved. The inversion was carried out in the Hampson-Russell suite.

Soft constraints were applied during the inversion using a smooth low-frequency model generated through a 15-sample moving average rather than strictly enforcing the well-log values. The low-frequency model provides the required impedance trend because the low-frequency seismic content is missing. The impedance model was then updated iteratively, typically over 10–20 iterations, to minimize the difference between the synthetic and real seismic data. The inversion achieved a good match between the two datasets, with a high correlation of approximately 0.99, indicating a good convergence of the inversion**.**

### 3.6.1 Wavelet Extraction and Well Correlation

The wavelet describes the seismic pulse and controls the entire inversion, since an incorrect wavelet produces an impedance model that fits the data for the wrong reason. A statistical wavelet was first extracted from the seismic data alone to establish the frequency content and approximate length. A well-based wavelet was then extracted using the sonic and density logs over an analysis window spanning the reservoir interval, which additionally recovers the phase. Wavelet length and analysis window were chosen to be long enough for stable estimation but short enough to remain representative of the interval of interest. The extracted wavelet was assessed from its amplitude and phase spectra and from the quality of the correlation it produced between the synthetic and the recorded seismic trace at each well. This correlation is the same measurement made during the seismic-to-well tie of Section 3.4.2, and the two steps were iterated until the tie and the wavelet were mutually consistent.

### 3.6.2 Inverted Trace

An initial low-frequency model was constructed by interpolating impedance from the well logs along the interpreted horizons, so that the model follows the mapped structure instead of a horizontal layering. The model was then filtered to retain only the low frequencies absent from the seismic bandwidth, which prevents the well data from imposing detail that the seismic data cannot support. Inversion analysis was run at each well to select the inversion parameters, comparing the inverted result with the measured impedance log and examining the residual between the synthetic and the recorded trace. The parameters governing the number of iterations and the permitted deviation of the result from the initial model were adjusted until the inverted impedance reproduced the log response without the

solution simply reverting to the input model. The parameters established at the wells were then applied to invert every trace along the three lines carrying well control, TJ-89-512, TJ-89-516 and TJ-89-526, producing the inverted trace sections. The inversion was confined to these lines because the wavelet and the low-frequency model can only be calibrated where log control exists. The remaining seven lines are carried forward as structural interpretation, contributing the fault and horizon framework but not property estimates.

### 3.6.3 Final Impedance Model

The final impedance model is the set of inverted sections along the seismic grid, expressed in absolute acoustic impedance. Quality control was carried out in two ways. The inverted impedance at each well was compared with the impedance computed independently from the logs, and the analysis was repeated with one well excluded so that its impedance log served as an independent check on a result it had not helped to constrain, a more demanding test than comparison at the wells used in the inversion. The final model provides the impedance sections from which reservoir zones are identified, and it is also the predictor supplied to the machine-learning stage described in Section 3.6.

## 3.7 Fault Seal Analysis

A fault is neither inherently a barrier nor inherently a conduit; its behaviour depends on the rock properties juxtaposed across it (Allan, 1989), and the question is central at Kadanwari because the faults that create the closures also segment the reservoir and have been identified as possible pathways for the vertical migration of injected CO2 (Shah et al., 2024). The assessment was made by juxtaposition, following Allan (1989) and Knipe (1997), and applied to F3, the major bounding fault and the one carrying the largest throw. Its inputs are the fault surface of Section 3.4.3, the depth-converted horizon cut-offs of Section 3.4.5, and the assignment of each unit to reservoir or non-reservoir from the formation tops and the shale volume of Section 3.3.1.

Nine positions were taken along the trace of F3, and at each the contour value was read separately on the upthrown and the downthrown side for the D sand, the C sand, and the top and base of the B sand. Reading both sides at the same position converts a map into a fault-plane section: the difference between the two values is the throw, and the pair fixes the depth interval each block occupies on the fault there. The profiles were then plotted against position with depth increasing downwards, the top of the B sand taken as the top of

the reservoir and its base as the top of the underlying shale, so that the interval between the two lines on either side represents the sand itself.

The diagram is read by looking for overlap between the reservoir intervals of the two blocks. Where they overlap, sand is placed against sand and the juxtaposition provides no seal in itself; where the throw carries the reservoir of one block clear of the other, the sand stands against the enclosing fine-grained section and seals without any requirement on the fault rock. Positions at which reservoir is placed against non-reservoir were annotated as possible sealing areas, and the spill points limiting the trap were read from the same construction (Allan, 1989).

The analysis has three limits. The analysis establishes juxtaposition and nothing more: a sand-against-sand window is not proof of leakage, since entrained clay may still support a pressure difference, and a sand-against-shale window is not proof of seal. Quantifying the fault rock would require that entrained fraction calibrated against measured across-fault pressure differences (Yielding et al., 1997; Bretan et al., 2003) and an assessment of whether any smear is continuous (Færseth, 2006), and neither the pressure data nor the along-fault shale-volume control was available here. The cut-off depths are only as accurate as the depth conversion, although a systematic velocity error displaces both profiles together and leaves the throws better constrained than the absolute depths. And the analysis is static, saying nothing about whether a fault would remain stable under the pressure increase caused by injection. The result is carried into Section 3.8, where each fault-bounded closure is treated as a separate storage compartment.

## 3.8 Storage Capacity Estimation

Storage capacity was estimated volumetrically. The quantity sought is the mass of CO2 that the pore space of a given structural closure could hold, and it is obtained in two steps: the pore volume of the closure is calculated from its mapped area, its effective reservoir thickness and its effective porosity, and that pore volume is then reduced to the fraction available to CO2 and converted to a mass. The calculation was carried out independently for each of the three closures delineated on the Lower Goru B sand, so that capacity is reported for each structural compartment instead of as a single field-wide figure. What the method produces is a static estimate intended for evaluation and for comparison between closures (Bachu et al., 2007).

Pore volume follows from the geometry of the closure and the quality of the rock within it,

$$V_{pore} = A \cdot h \cdot \phi_e \quad \text{(Bachu et al., 2007)} \qquad (3.10)$$

where A is the area enclosed by the closure in map view, h is the effective reservoir thickness and φe is effective porosity. The area of each closure was obtained by delineating a polygon around the closing contours on the gridded B sand surface of Section 3.4.5 and measuring the area the polygon encloses. Using separate polygons instead of a single field outline lets the fault blocks be compared with one another, and it also keeps the capacity figures consistent with the fault-seal result of Section 3.7, since each polygon lies within one fault-bounded compartment. The effective thickness is the part of the interpreted reservoir interval considered to contribute to storage, not the gross stratigraphic thickness, non-reservoir intervals within the succession being excluded from it. Effective porosity is that computed from the logs in Section 3.3.2 and predicted between the wells in Section 3.6, which lets lateral variation in reservoir quality enter the estimate in place of a single well-averaged value.

Pore volume is not itself storage capacity. Part of the pore space remains occupied by formation water, only part of what remains would be contacted by an injected plume, and the volume has to be converted to a mass at the density CO2 takes in the reservoir:

$$M_{CO_2} = V_{pore} \cdot (1 - S_w) \cdot \rho_{CO_2} \cdot E \quad \text{(Bachu et al., 2007)} \qquad (3.11)$$

where Sw is water saturation, ρCO2 is the density of CO2 at the adopted reservoir condition and E is the storage efficiency factor. Water saturation is taken from the Indonesian-equation result of Section 3.3.3 and supported by the predicted saturation sections of Section 3.6, so that the term (1 − Sw) represents the fraction of the pore space not occupied by formation water.

A CO2 density of 600 kg/m³ was adopted. This is treated throughout as an adopted calculation parameter, not a physical constant, because the density of CO2 varies strongly with pressure and temperature and would be obtained in a more detailed treatment from the reservoir pressure and temperature through an equation of state (Span & Wagner, 1996). The value used here is representative of the dense phase at the depth of the Lower Goru B sand, and applying it uniformly to all three closures keeps them comparable with one another. The storage efficiency factor accounts for the proportion of the theoretical pore volume that an injected plume would in practice contact, and is required because heterogeneity, incomplete displacement and limited connectivity all restrict the volume actually accessible. It is not a

measured quantity and remains the largest single source of uncertainty in any capacity figure (Bachu et al., 2007).

Permeability was estimated as part of the reservoir characterisation but does not appear in the equations above. It governs how readily fluid moves through the rock and bears directly on injectivity, whereas the volumetric result is controlled by area, thickness, porosity, saturation, density and efficiency alone. Its role here is as a supporting indicator of reservoir quality, weighed alongside the capacity figures when the closures are compared with one another.

The resulting estimate is a preliminary assessment. It quantifies the storage resource contained within the three delineated closures, and it does so for each closure separately so that the more favourable can be identified. It does not establish injectivity, model the movement of a plume over time, evaluate the integrity of the existing wellbores, or demonstrate long-term containment, each of which would require dynamic simulation and data beyond those available for this study. The capacity figures are read together with the fault-seal result of Section 3.7, on the principle that capacity which cannot be retained is not storage.

# CHAPTER 4
# RESULTS AND INTERPRETATION

## 4.1 Introduction

This chapter presents the results obtained from the workflow set out in Chapter 3 and interprets them in terms of the carbon-storage potential of the Lower Goru B sand at the Kadanwari Gas Field. The results are reported in the order in which they were produced, because each stage supplies the input to the one that follows: the petrophysical evaluation describes the reservoir at the three well locations, the structural interpretation places those wells within a mapped framework of horizons and faults, and the seismic inversion with the machine-learning prediction that follows it extends the well-based description along the tied seismic lines.

Section 4.2 presents the petrophysical results for Kadanwari-01, Kadanwari-03 and Kadanwari-04, comprising shale volume, total and effective porosity and water saturation computed from the wireline logs. Section 4.3 presents the seismic-to-well ties, the interpreted seismic sections for the ten two-dimensional lines and the time and depth structure maps generated from the gridded horizon picks. Section 4.4 presents the model-based inversion results along the three lines carrying well control, and Section 4.5 the reservoir property sections predicted from the inverted impedance. Section 4.6 presents the fault-seal analysis of the major bounding fault, and Section 4.7 the volumetric $CO_2$ storage-capacity estimates for the three structural closures delineated on the Lower Goru B sand.

Throughout the chapter the Lower Goru B sand is treated as the interval of interest, and the Upper Goru and Chiltan horizons are used as the bounding references for the interpretation. Results are described first and interpreted immediately afterwards, with each figure discussed in the text that precedes it. The implications of these results for containment and for storage capacity are drawn together in the sections that follow the property predictions.

## 4.2 Petrophysical Results

The petrophysical evaluation was carried out in GVERSE Petrophysics using the workflow described in Section 3.3. The results for each well are presented as a composite log display in which the tracks are arranged in the order in which the calculation proceeds. The correlation track carries the gamma ray, spontaneous potential and caliper curves; the depth track is in measured depth; the resistivity track carries the micro-spherically focused,

shallow and deep laterolog responses; the porosity track carries the neutron and bulk density curves with the crossover shaded to indicate gas effect; and the remaining tracks carry the sonic and photoelectric factor responses, the computed shale volume with a sand and shale lithology fill, the total and effective porosity, and the water saturation obtained from the Indonesian equation with the hydrocarbon and water fractions shaded separately.

### 4.2.1 Kadanwari-01

Kadanwari-01 is the only well of the three that penetrates the full Lower Goru sand succession. The formation tops recorded in this well place the H sand at 3,079.0 m, the G sand at 3,153.0 m, the F sand at 3,268.0 m, the E sand at 3,340.0 m, the D sand at 3,369.0 m, the C sand at 3,420.0 m and the B sand at 3,528.0 m, with the underlying Sembar Formation encountered at 3,819.5 m. The tops are listed in Table 4.1. The B sand, which is the reservoir target of this study, therefore occupies the interval between 3,528.0 m and the Sembar top, giving a gross thickness of approximately 291 m and making it by a considerable margin the thickest of the Lower Goru sand units in this well.

| **Sand unit / formation** | **Top depth (m)** |
|---|---|
| H sand | 3,079.0 |
| G sand | 3,153.0 |
| F sand | 3,268.0 |
| E sand | 3,340.0 |
| D sand | 3,369.0 |
| C sand | 3,420.0 |
| B sand | 3,528.0 |
| Sembar Formation | 3,819.5 |

Table 4. 1 Formation tops recorded in Kadanwari-01 for the Lower Goru sand units and the underlying Sembar Formation.

The petrophysical display presented here covers the interval from approximately 3,520 m to 3,770 m. Within this interval the gamma-ray response is strongly serrated and alternates repeatedly between clean and shaly readings, and the computed shale volume follows it: the lithology track is dominated by interbedded sand and shale, not by thick clean

sand bodies. The neutron and density curves show a pronounced and laterally persistent crossover through most of the displayed interval, shaded in the porosity track. This indicates gas in the pore space and confirms that the section is hydrocarbon bearing. Total porosity exceeds effective porosity throughout, and the separation between the two curves widens over the shalier beds, as expected once the correction for clay-bound water is applied. Water saturation computed from the Indonesian equation is low over the cleaner sand intervals and rises towards unity in the interbedded shales, and the hydrocarbon-bearing intervals appear as discrete, relatively thin units rather than one continuous reservoir (Figure 4.1).

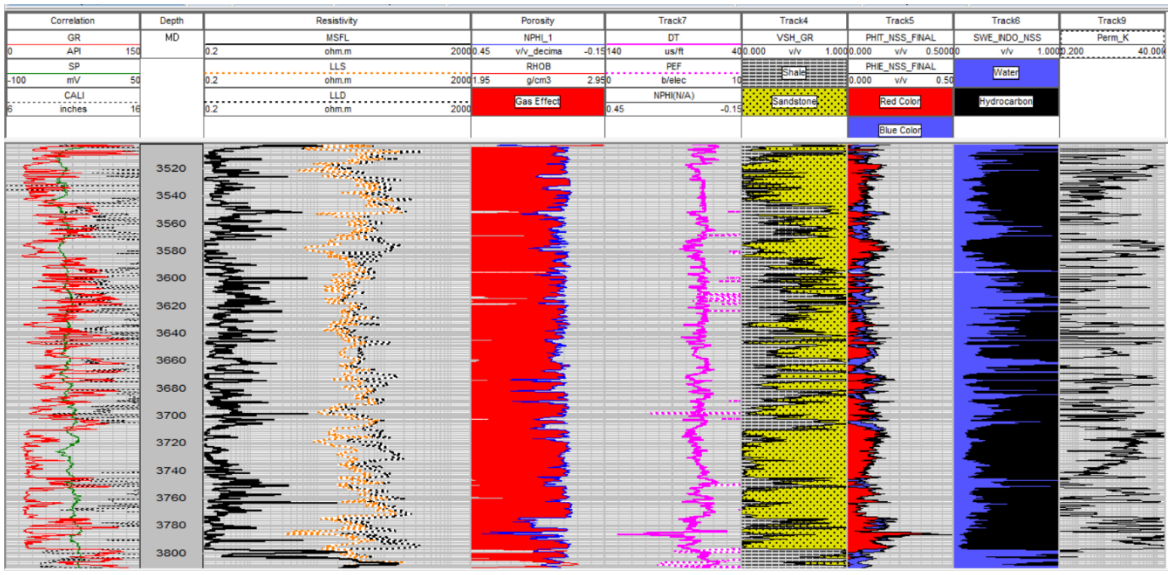



Figure 4. 1 Composite petrophysical display for Kadanwari-01 showing the correlation, resistivity, porosity, sonic and photoelectric factor tracks together with the computed volume of shale, total and effective porosity and water saturation over the Lower Goru Sand B interval.

### 4.2.2 Kadanwari-03

The evaluated interval in Kadanwari-03 extends from approximately 3,320 m to 3,470 m measured depth. Compared with Kadanwari-01 the gamma-ray character is blockier: the lithology track shows thicker and more continuous sand units separated by shale breaks, and the computed shale volume is lower over the sand-prone intervals. The deep and shallow resistivity curves separate markedly over these intervals, and the neutron-density crossover is well developed and coincident with the low shale-volume intervals. Together these indicate porous, gas-bearing sands, not a resistivity response driven by lithology alone. Effective porosity remains close to total porosity through the cleaner sands and departs from

it across the shale breaks. Water saturation is correspondingly low through the sand units, with the hydrocarbon-filled fraction occupying most of the saturation track over the best-developed sands. The results for this well describe the more favourable reservoir character of the three, although the logged section here does not extend to the B sand (Figure 4.2).

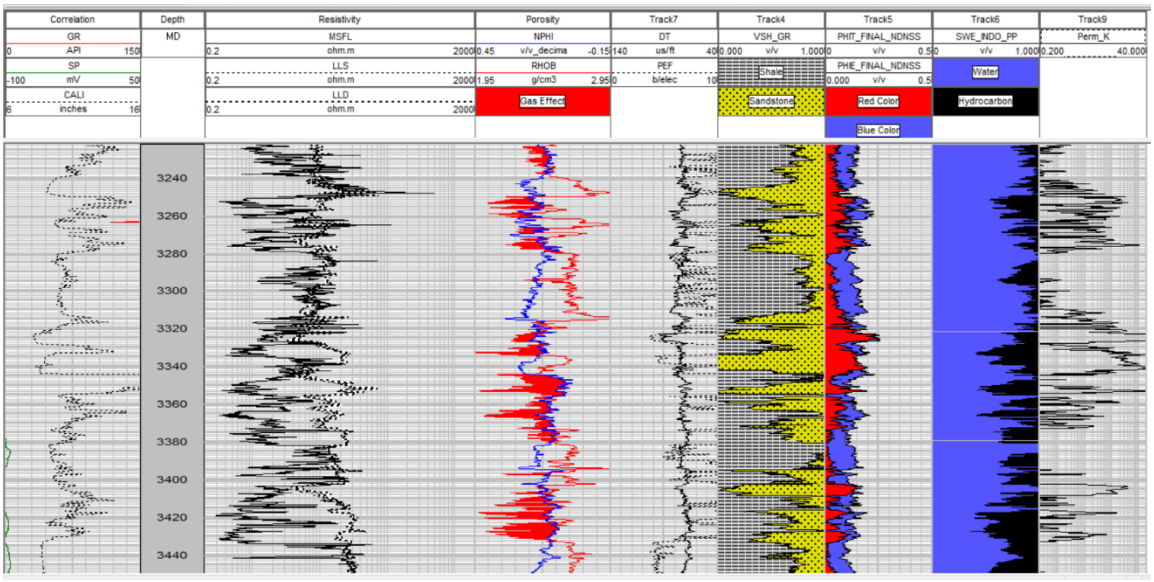



Figure 4. 2 Composite petrophysical display for Kadanwari-03 showing the computed volume of shale, total and effective porosity and water saturation over the logged Lower Goru H-Sand interval.

### 4.2.3 Kadanwari-04

The evaluated interval in Kadanwari-04 extends from approximately 3,100 m to 3,280 m measured depth. The gamma-ray and shale-volume responses indicate a section of intermediate character, with sand units that are well developed but more frequently interrupted by shale than in Kadanwari-03. Neutron-density crossover is present over the cleaner intervals and is accompanied by elevated deep resistivity, and the effective porosity curve tracks the total porosity closely where shale volume is low. Water saturation is variable through the displayed interval: several intervals return low values with a substantial hydrocarbon fraction, while the intervening beds approach full water saturation. Because this well does not penetrate the individual Lower Goru sand units, the results are used here to characterise the Lower Goru section in general and to supply the log control required for the inversion along line TJ-89-526; they are not used to describe the B sand directly (Figure 4.3).

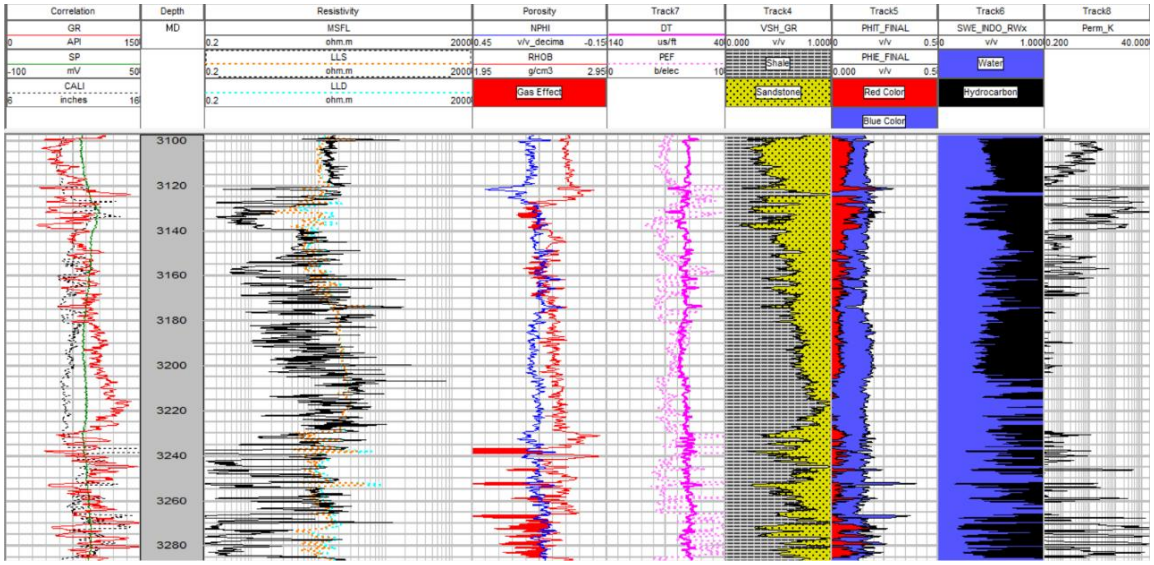



Figure 4. 3 Composite petrophysical display for Kadanwari-04 showing the computed volume of shale, total and effective porosity and water saturation over the logged Lower Goru interval.

### 4.2.4 Summary of the Petrophysical Results

The three wells together describe a Lower Goru section of interbedded sands and shales in which reservoir quality is developed in discrete units rather than uniformly. In every well the neutron-density crossover coincides with the intervals of lowest shale volume and lowest water saturation, so the three independent indications of reservoir quality agree. The persistent separation between total and effective porosity confirms that clay-bound water accounts for an appreciable fraction of the total pore volume, and it is the effective porosity that is carried forward into the volumetric estimation. For a storage assessment the low water saturations are read as pore space not presently occupied by formation water and therefore potentially available to injected $CO_2$, subject to the irreducible water saturation and storage efficiency terms discussed in Section 3.8.

## 4.3 Seismic Interpretation

The structural interpretation was carried out in GVERSE Geophysics on all ten two-dimensional lines. Three horizons were carried across the grid: the Upper Goru Formation, the B sand of the Lower Goru Formation and the Chiltan Formation. The Upper Goru and Lower Goru horizons were tied directly to the wells, whereas the Chiltan horizon was positioned from the regional stratigraphic succession and followed on the basis of its reflection character. The interpreted faults are predominantly normal and divide the section into horst and graben blocks, in agreement with published interpretations of the field.

### 4.3.1 Seismic-to-Well Ties

The seismic-to-well ties provide the depth-to-time calibration on which the horizon picks depend. In Kadanwari-01, on line TJ-89-516, the synthetic seismogram generated from the sonic and density logs reproduces the reflection character of the extracted seismic trace over the interval of interest, and the formation tops listed in Table 4.1, from the H sand at 3,079.0 m through to the B sand at 3,528.0 m and the Sembar Formation at 3,819.5 m, project onto consistent seismic events. The cross-correlation between the synthetic and the extracted trace reaches a maximum of 0.585 over the 1,270 to 2,500 ms window. The strong reflection at the Upper Goru level and the group of high-amplitude events at the B sand level provide the two anchors used when the horizons were carried away from the well. Figure 4.4 shows the tie.

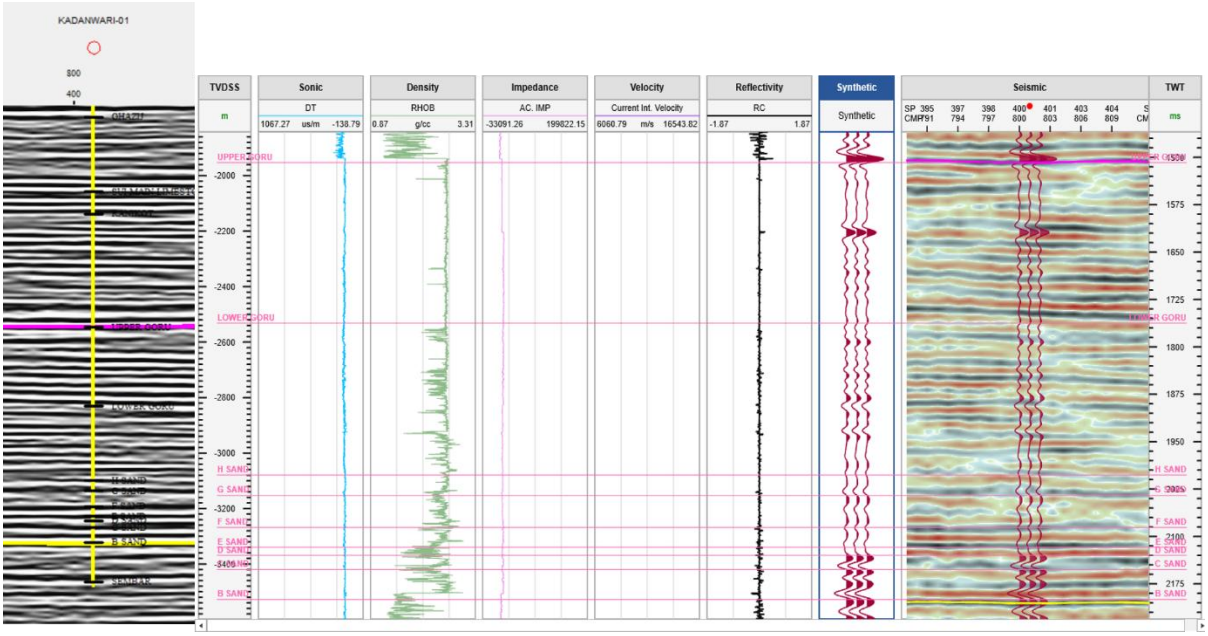



Figure 4. 4 Seismic-to-well tie for Kadanwari-01 on line TJ-89-516, showing the sonic, density, impedance, velocity and reflectivity tracks, the synthetic seismogram and the extracted seismic trace with the Lower Goru sand tops posted.

In Kadanwari-03, on line TJ-89-512, the tie returns the highest correlation of the three wells, with a maximum cross-correlation of 0.69 over the 1,100 to 2,400 ms window. The match is good across the Upper Goru and Lower Goru intervals, and the H sand top is clearly resolved. The higher correlation obtained at this well follows from the more blocky log character described in Section 4.2.2, which produces a reflectivity series with stronger and more distinctive events (Figure 4.5).

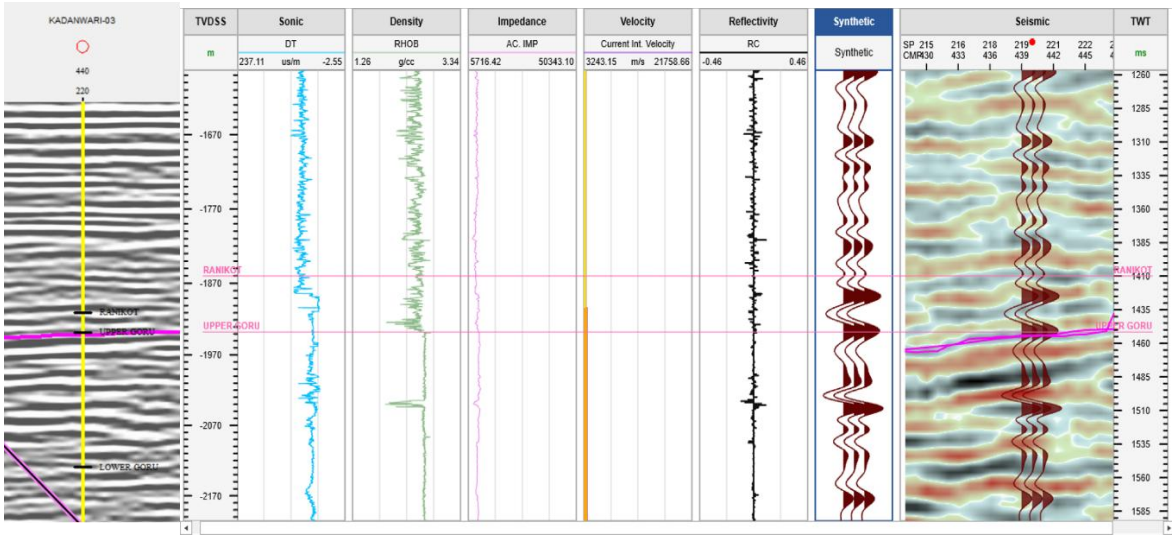



Figure 4. 5 Seismic-to-well tie for Kadanwari-03 on line TJ-89-512, showing the synthetic seismogram against the seismic trace extracted at the well location.

In Kadanwari-04, on line TJ-89-526, the maximum cross-correlation is 0.594 over the 1,500 to 2,360 ms window. The tie is acceptable across the Upper Goru and Lower Goru levels, although the correlation is lower than at Kadanwari-03; this is attributed to the shorter logged section available at this well and to the absence of the individual Lower Goru sand tops, which reduces the number of independent events available for matching (Figure 4.6).

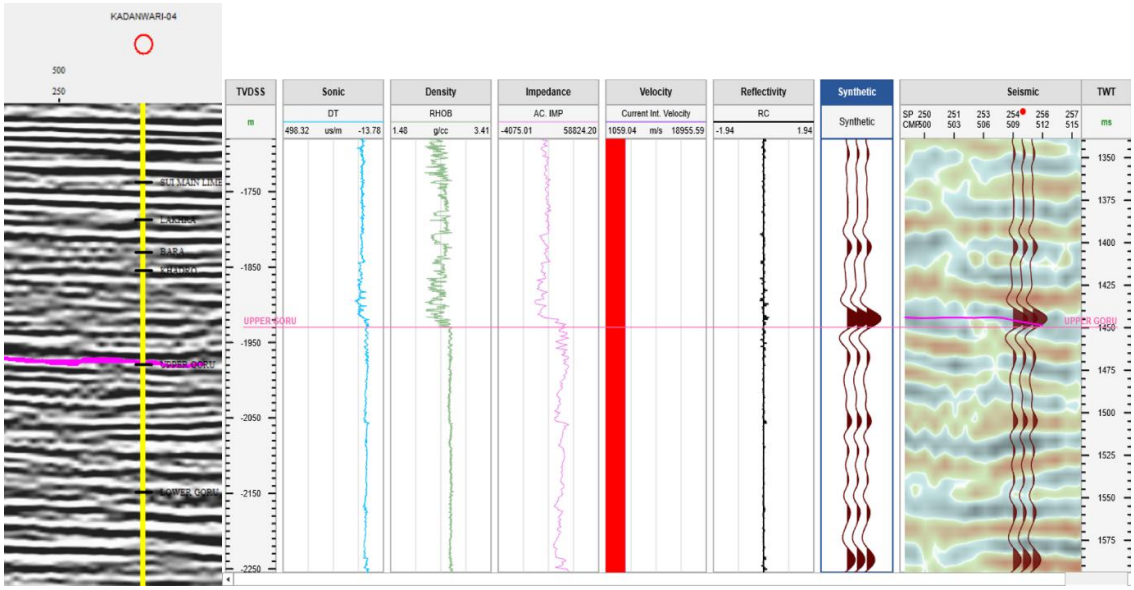



Figure 4. 6 Seismic-to-well tie for Kadanwari-04 on line TJ-89-526, showing the synthetic seismogram against the extracted seismic trace.

### 4.3.2 Interpreted Seismic Sections

The interpreted sections are displayed in two-way travel time with the Upper Goru horizon in magenta, the Lower Goru B sand in yellow and the Chiltan horizon in red. The

three horizons are laterally continuous across the grid and maintain an approximately constant separation, the Upper Goru arriving at about 1,450 to 1,500 ms, the B sand at about 2,150 to 2,200 ms and the Chiltan at about 2,700 to 2,750 ms. The faults are shown in colours that are carried consistently from line to line so that individual fault planes can be correlated across the survey.

Line TJ-89-510 crosses the western part of the survey and shows three faults cutting the interpreted interval. Two of these are steeply dipping and extend from above the Upper Goru level down through the B sand, while the third is developed in the eastern part of the section and terminates near the Chiltan level. The B sand horizon is close to horizontal across the section, with a subtle rise towards the east where it is offset by the faults (Figure 4.7).

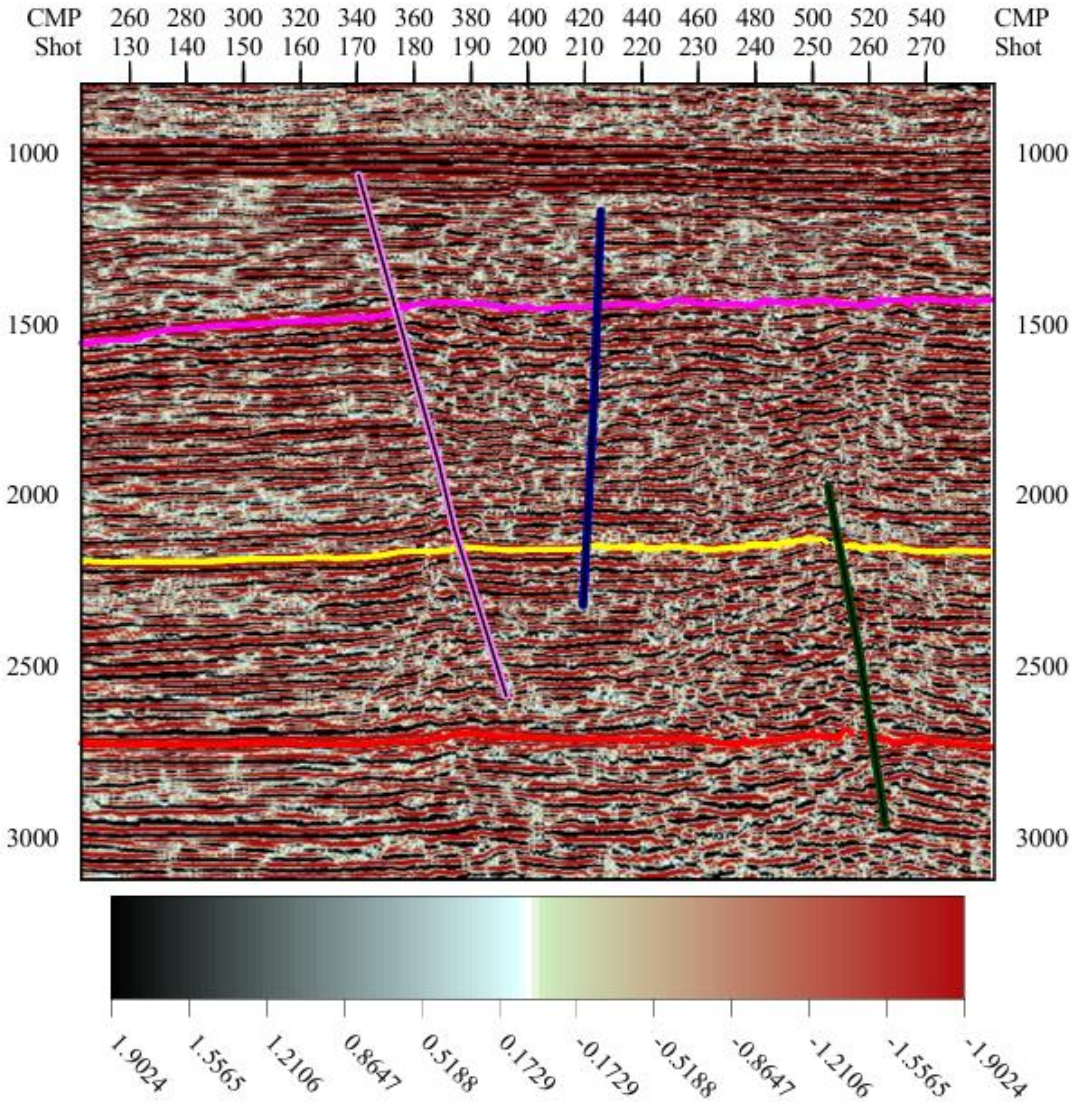



Figure 4. 7 Interpreted seismic section along line TJ-89-510 showing the Upper Goru, Lower Goru B sand and Chiltan horizons and the interpreted faults.

Line TJ-89-512 carries Kadanwari-03 at approximately CDP 440, and the formation tops projected from the well confirm the horizon picks. Three faults are interpreted on this line. The two central faults dip towards each other and define a downthrown block between them at the B sand level, while the fault to the west of the well displaces the section above and below the Upper Goru horizon. The B sand horizon is continuous across the section and is disrupted rather than displaced by large throws, indicating moderate compartmentalisation along this line (Figure 4.8).

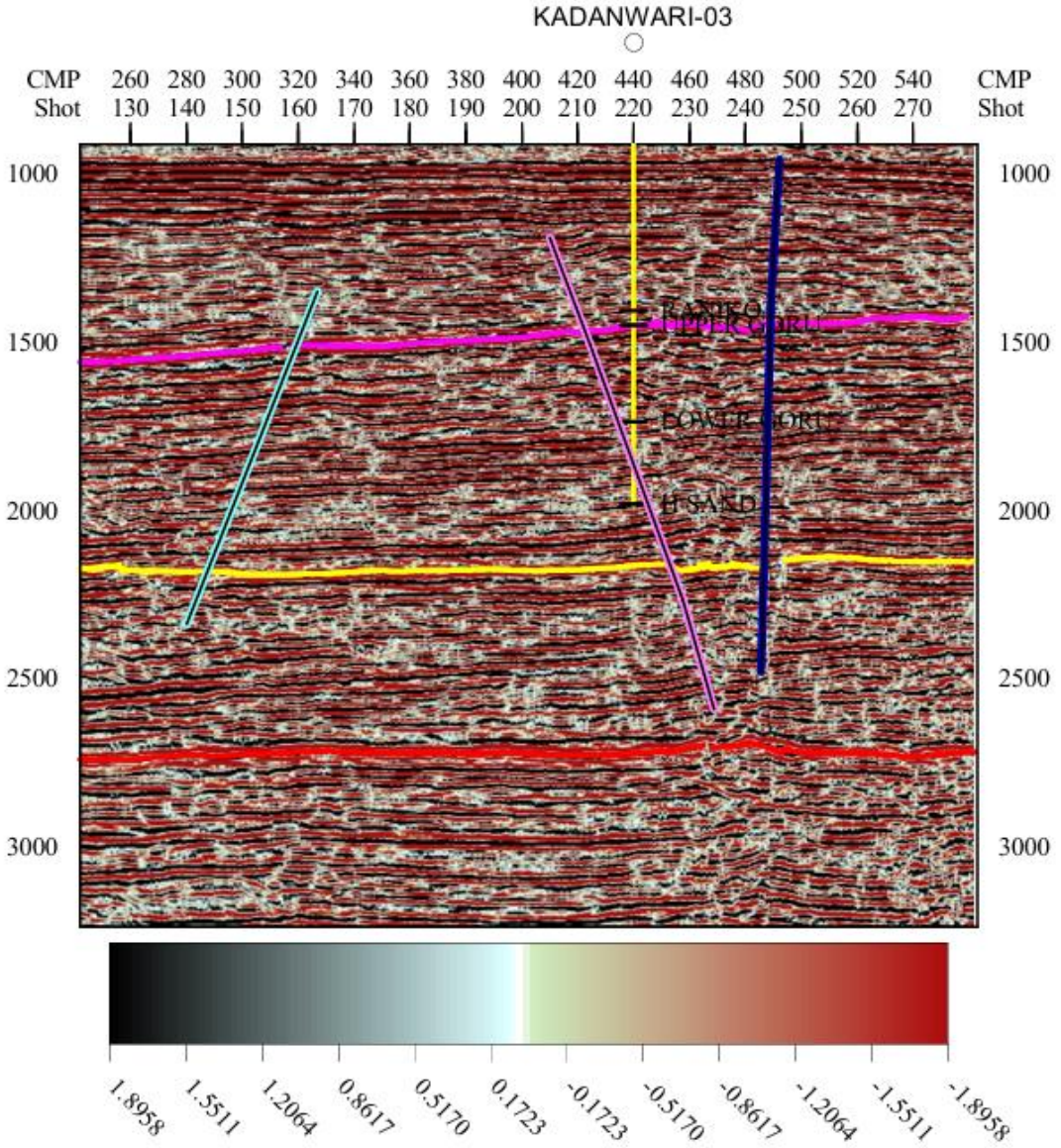



Figure 4. 8 Interpreted seismic section along line TJ-89-512 with Kadanwari-03 projected onto the section, showing the interpreted horizons and faults.

Line TJ-89-516 carries Kadanwari-01 near the eastern end of the line and is the most heavily faulted of the interpreted sections, with six faults identified. The two faults in the

central and eastern parts of the section have the largest throws and extend from above the Upper Goru level to below the Chiltan horizon; the B sand shows a clear offset across both. The remaining faults are shorter and are restricted to the interval above or below the reservoir level. The block bounded by the two major faults is downthrown relative to its neighbours and forms one of the compartments carried forward into the mapping. Figure 4.9 shows the interpreted section.

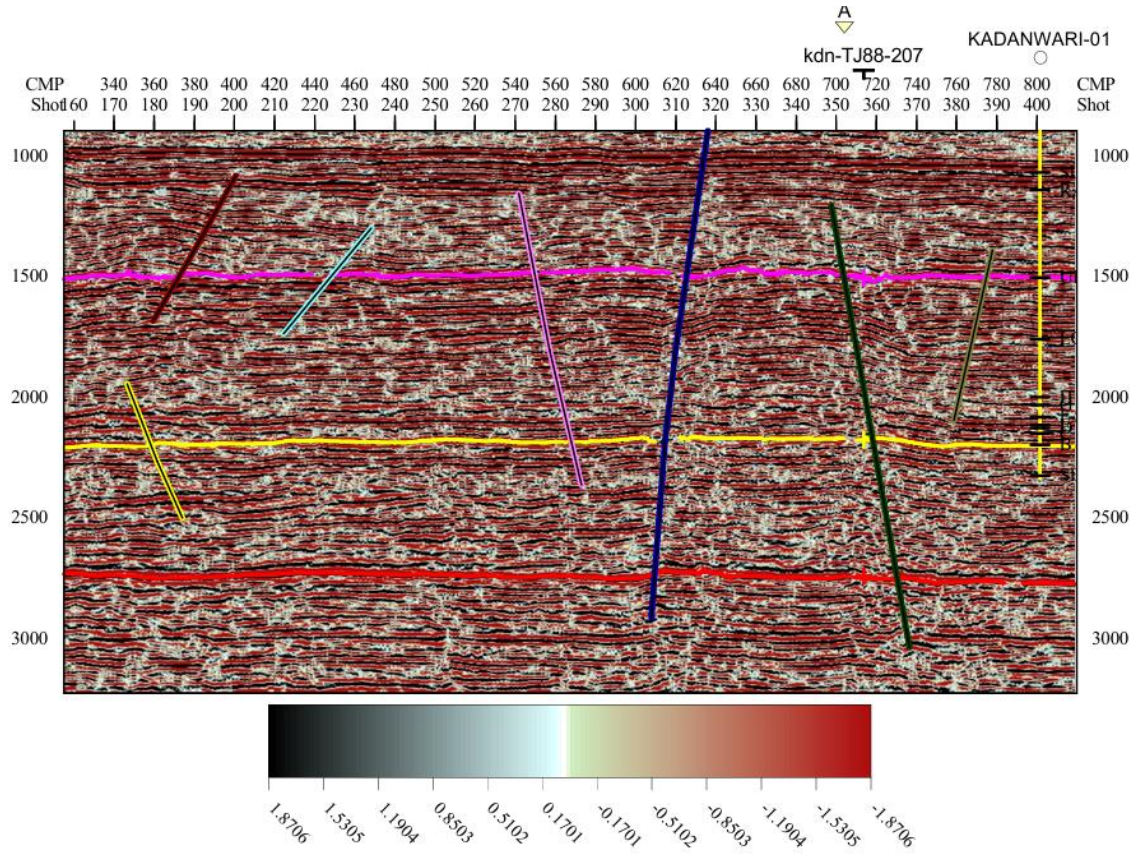



Figure 4. 9 Interpreted seismic section along line TJ-89-516 with Kadanwari-01 projected onto the section, showing the interpreted horizons and the major bounding faults.

Line TJ-89-518 intersects lines TJ-88-207 and TJ-91-803 and shows seven faults. Two closely spaced faults in the west form a narrow graben at the B sand level, while the faults in the centre and east of the section define a horst block bounded by oppositely dipping planes. The Upper Goru and B sand horizons are offset across the major faults, whereas the Chiltan horizon is displaced by a smaller amount, suggesting that displacement decreases with depth on these planes (Figure 4.10).

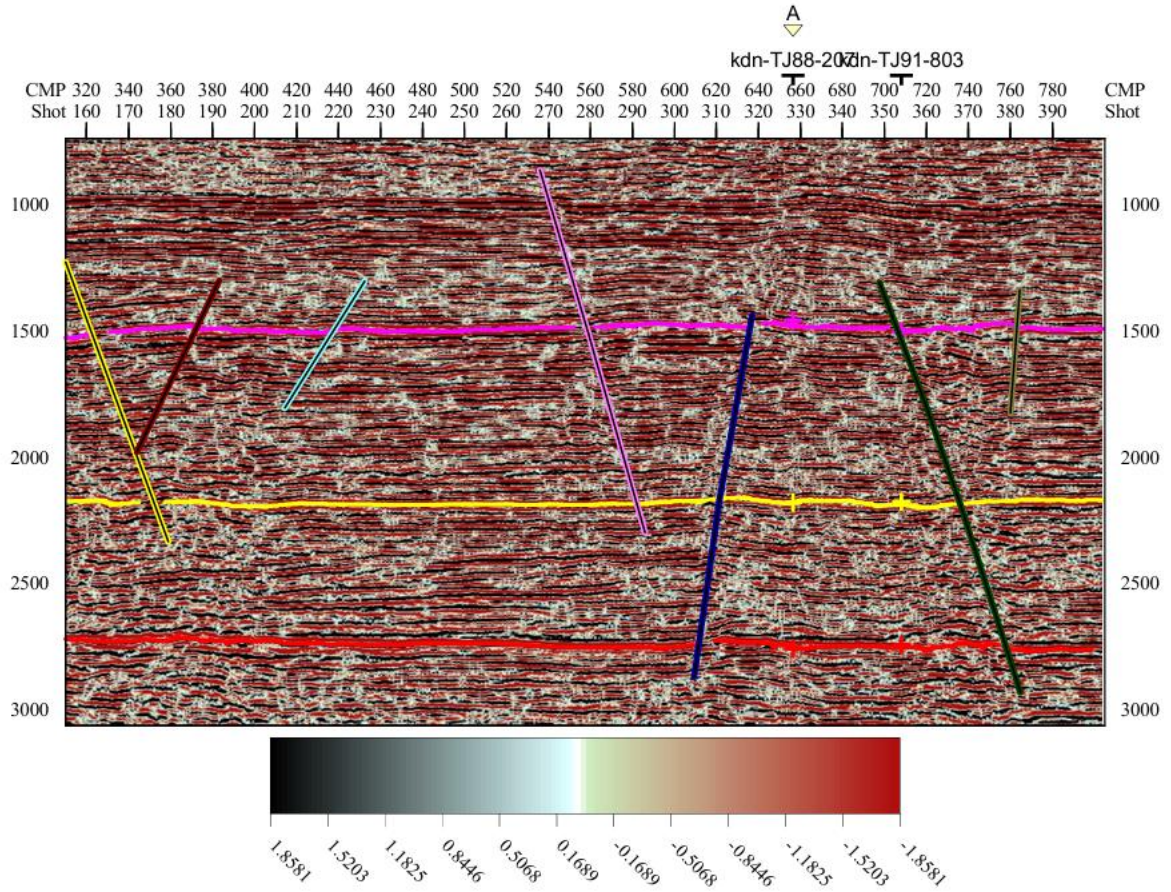



Figure 4. 10 Interpreted seismic section along line TJ-89-518 showing the interpreted horizons, the graben in the western part of the line and the horst block in the east.

Line TJ-89-520 shows seven faults, of which the two in the east extend from the shallow section through the reservoir interval. The B sand horizon is offset across the faults in the western half of the line and is comparatively undisturbed beneath the intersection with line TJ-88-207. The pattern of oppositely dipping planes on either side of the centre of the section defines a broad structural high at the B sand level (Figure 4.11).

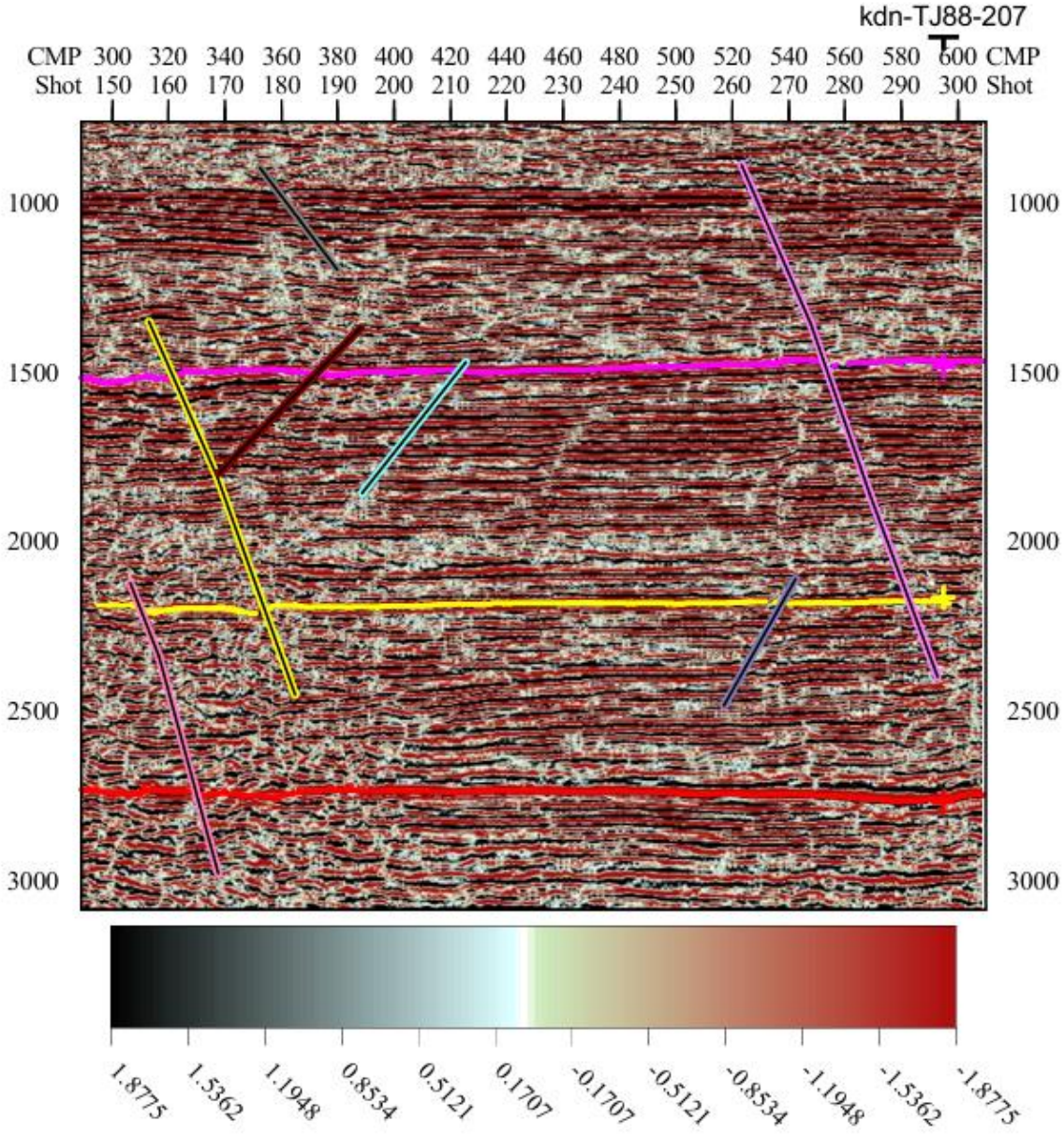



Figure 4. 11 Interpreted seismic section along line TJ-89-520 showing the interpreted horizons and faults, with the intersection with line TJ-88-207 marked.

Line TJ-89-522 shows six faults. Three of these are restricted to the interval around the Upper Goru horizon and do not reach the reservoir level, whereas the faults in the west and east of the section cut the B sand horizon. The B sand is close to horizontal along most of the line and rises slightly towards the east (Figure 4.12).

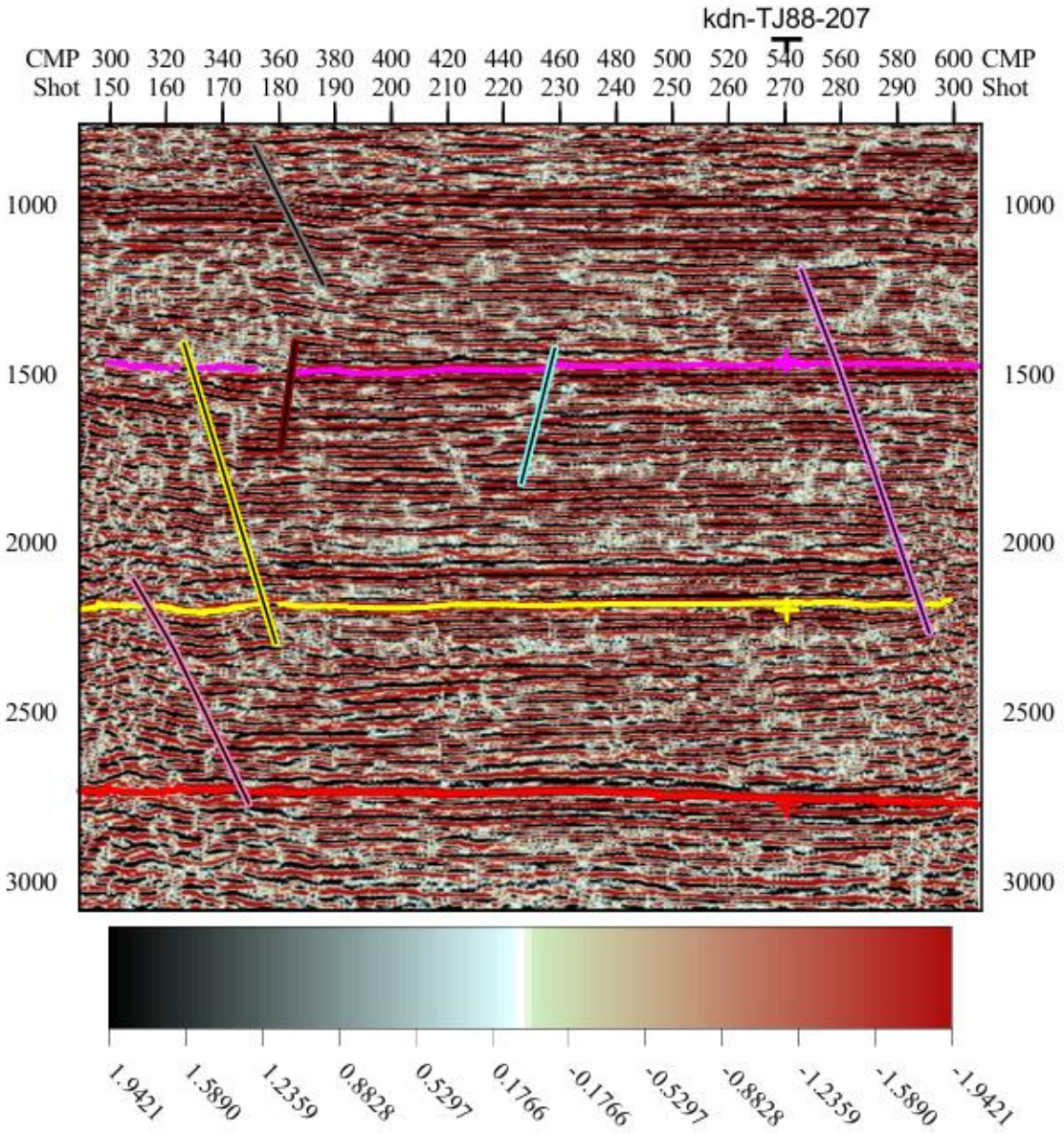



Figure 4. 12 Interpreted seismic section along line TJ-89-522 showing the interpreted horizons and faults.

Line TJ-89-524 intersects lines TJ-88-207 and TJ-91-803 and shows six faults, two of which have substantial throws and extend from the shallow section through the Chiltan horizon. These two faults bound the block in which the B sand reaches its shallowest travel time along the line. The remaining faults are shorter and are confined either to the interval above the Upper Goru or to the section below the reservoir. The interpreted section is given in Figure 4.13.

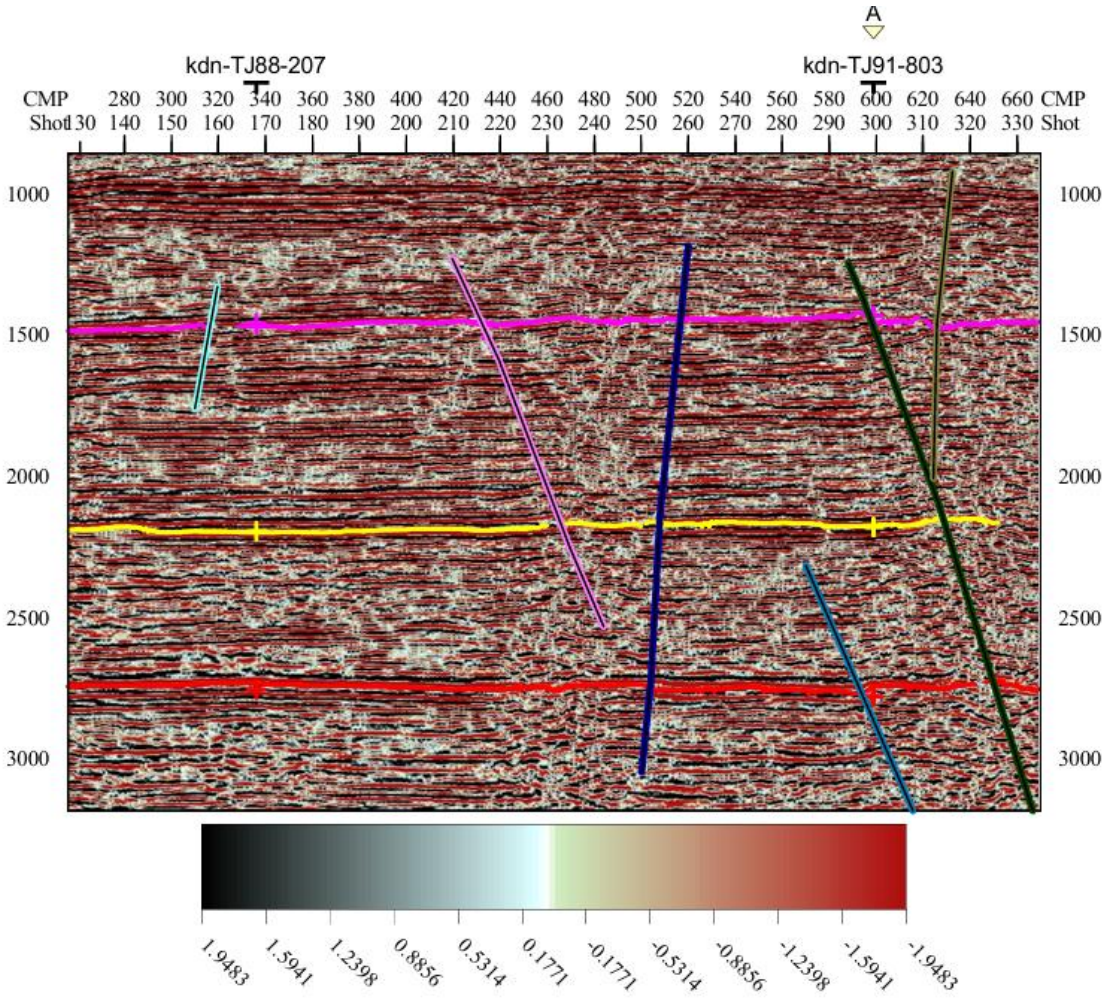



Figure 4. 13 Interpreted seismic section along line TJ-89-524 showing the interpreted horizons and faults, with the intersections with lines TJ-88-207 and TJ-91-803 marked.

Line TJ-89-526 carries Kadanwari-04 at approximately CDP 510 and shows four faults. The fault immediately to the west of the well and the fault to the east are the more significant of these; both cut the B sand horizon and extend below the Chiltan level, and they bound the block in which Kadanwari-04 is located. The formation tops projected from the well confirm the position of the Upper Goru and Lower Goru horizons on this line (Figure 4.14).

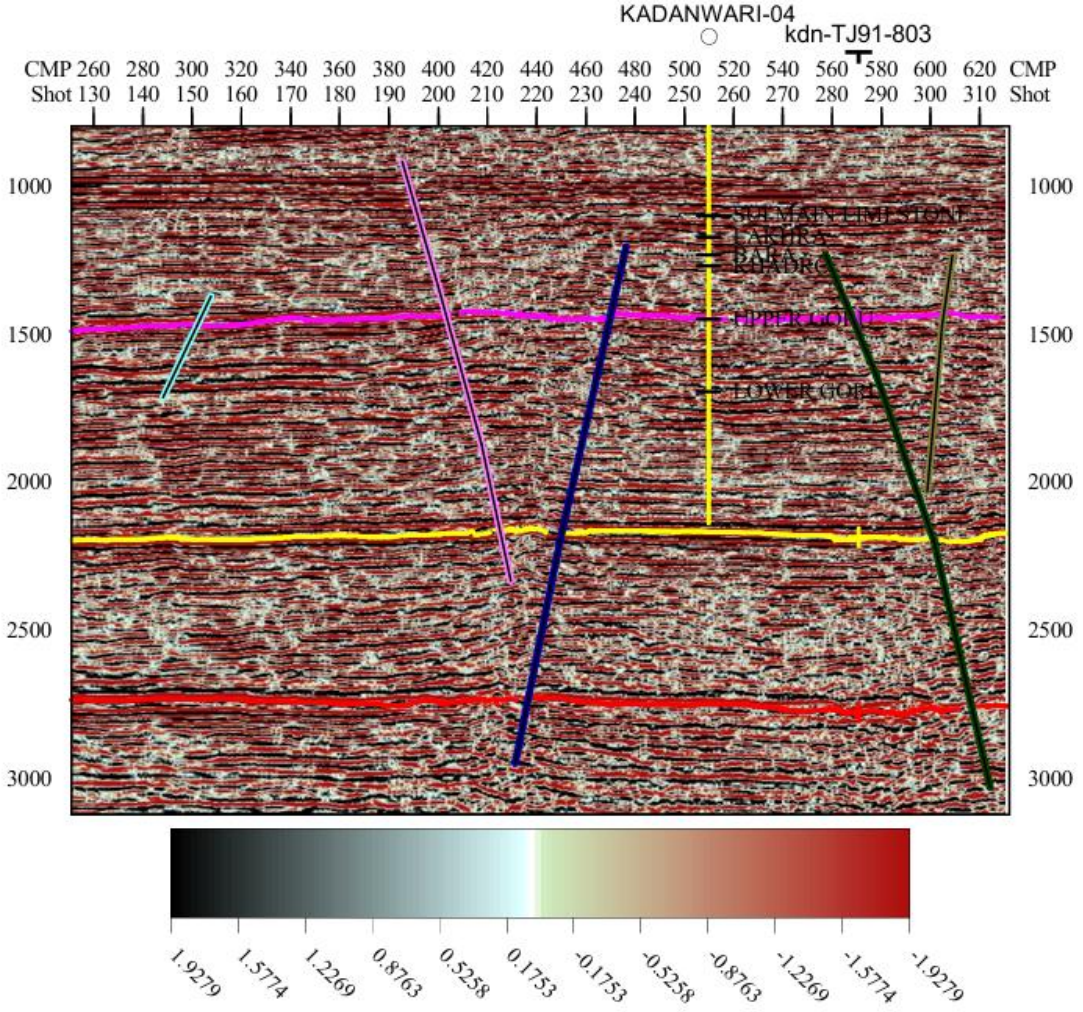



Figure 4. 14 Interpreted seismic section along line TJ-89-526 with Kadanwari-04 projected onto the section, showing the interpreted horizons and the faults bounding the well block.

### 4.3.3 Time and Depth Structure Maps

The interpreted horizon picks were gridded to produce time-structure maps, and these were converted to depth using the velocity control derived from the three well ties, as described in Sections 3.4.4 and 3.4.5. The maps cover the area enclosed by the seismic grid and carry the three well locations for reference. The fault traces appear on the maps as the north-northwest to south-southeast lineations along which the contours are displaced.

The Lower Goru B sand time-structure map is the more important of the four for this study, because it defines the geometry of the reservoir interval. The horizon is contoured between approximately 2,131 and 2,210 ms, and its grain is strongly north-northwest to south-southeast, parallel to the fault trend. The shallowest part of the map is a narrow fault-bounded block immediately north and north-east of Kadanwari-03, where values fall to about

2,150 ms and below and the contours close around the culmination; this is the structure on which the storage closures of Section 4.7 were subsequently delineated. From there the horizon deepens westwards and southwards to about 2,200 ms in the western and south-western part of the survey, where several closed lows are developed between the fault traces, and Kadanwari-01 in the east lies within a separate closed low. The segmentation of the surface into narrow elongate blocks is the map expression of the horst and graben pattern seen on the interpreted sections (Figure 4.17).

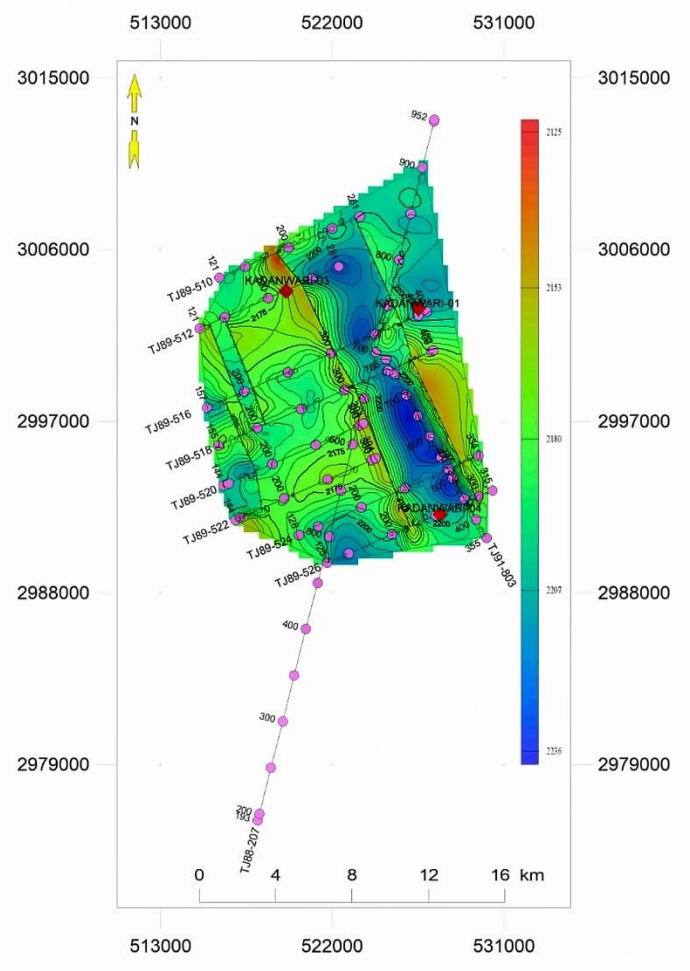



Figure 4. 15 Time-structure map of the Lower Goru B sand, contoured in two-way travel time, with the three well locations posted.

The Lower Goru B sand depth-structure map is the surface on which the fault-seal analysis and the volumetric estimation are performed, and it reproduces the configuration of the time map. The horizon lies at approximately 3,438 to 3,462 m over the culmination north of Kadanwari-03 and falls to about 3,540 m in the south-west of the survey, a relief of roughly 150 m, while Kadanwari-01 sits within a closed low at about 3,522 m. The contour offsets

across the bounding faults provide the upthrown and downthrown cut-off depths required for the juxtaposition analysis described in Section 3.7 (Figure 4.18).

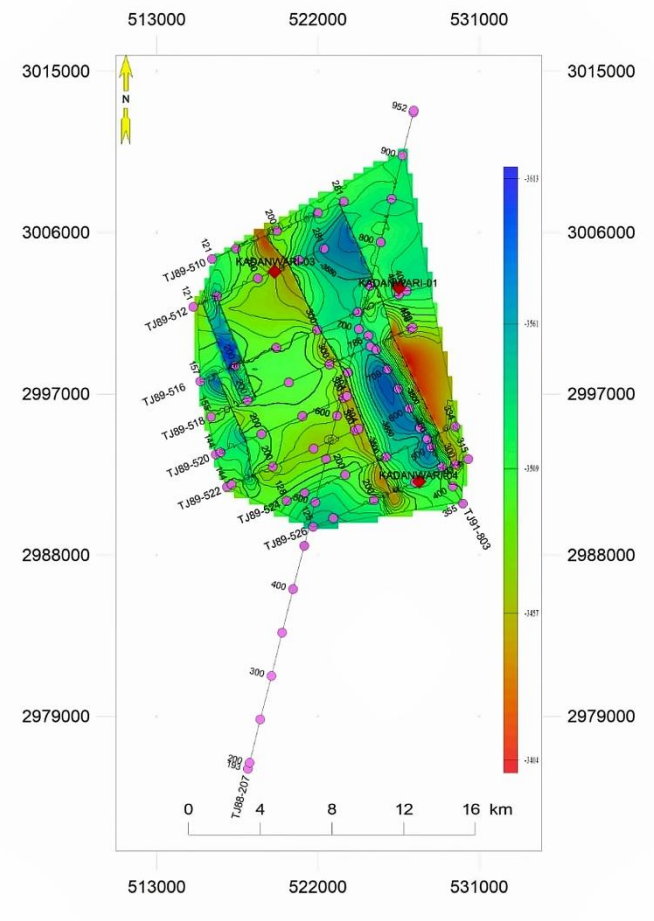



Figure 4. 16 Depth-structure map of the Lower Goru B sand, converted from the time-structure map and used as the basis for the fault-seal analysis.

## 4.4 Machine Learning

The inverted P-impedance of Section 4.4 was used as the single predictor in the Extra Trees regression described in Section 3.6, and separate models were trained at each well to predict volume of shale, total porosity, effective porosity and water saturation. The trained models were applied trace by trace along the three well-tied lines, giving twelve predicted sections in all. The results are presented line by line below, and each section is displayed on its own colour scale.

These sections should be read with two points in mind. First, the four properties on any one line are all derived from the same impedance section, so they are not four independent measurements. Each is a transform of one input, and their agreement over a given interval is a property of the transforms, not independent corroboration of the interpretation. Second, as noted in Section 3.6, a tree ensemble cannot extrapolate beyond

the range of impedance present in its training data, and the training data are confined to the logged intervals. Predictions above the logged section are therefore unconstrained, and the uniform, featureless bands that appear in the shallow part of several sections are artefacts of that limitation rather than geological observations. Interpretation below is confined to the Lower Goru interval.

### 4.4.1 Line TJ-89-512 (Kadanwari-03)

The predicted shale-volume section along TJ-89-512 is displayed on a scale from 0.15 to 0.70. Above approximately 800 ms the section is uniform and carries no detail, which marks the interval above the logged section where the prediction is unconstrained. Below that level the section is layered, with shale volume varying between roughly 0.35 and 0.60 in bands that are continuous along the full length of the line. The most shale-rich interval lies between about 1,900 and 2,200 ms, and values fall to approximately 0.42 to 0.50 through the Lower Goru interval between 2,200 and 2,500 ms. The reduction in shale content at reservoir level is real but modest, and the predicted section does not resolve a clean sand at this location (Figure 4.33).

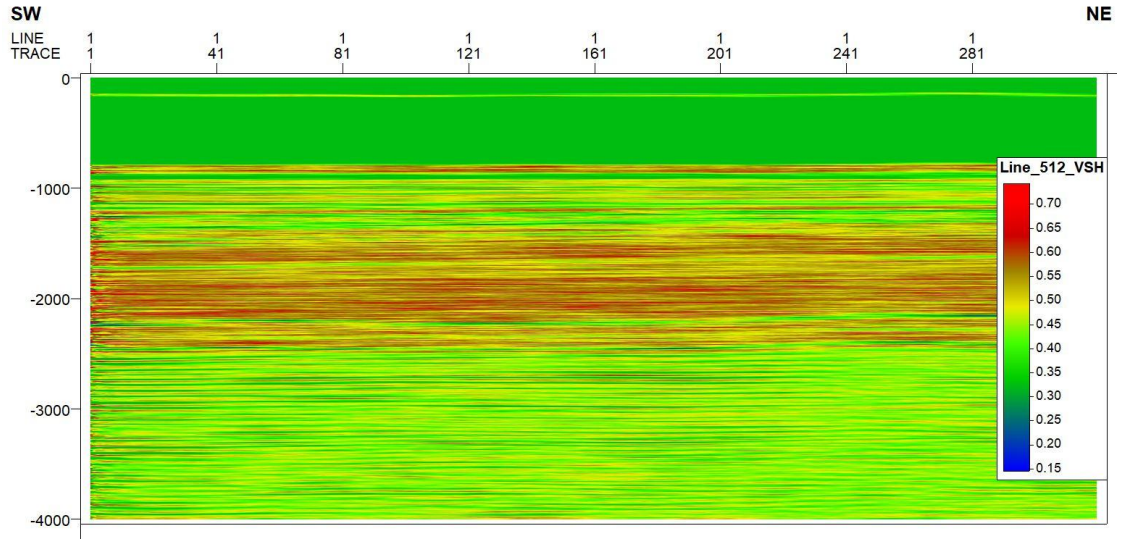



Figure 4. 17 Predicted volume of shale along line TJ-89-512, calibrated at Kadanwari-03, displayed on a scale from 0.15 to 0.70.

Total porosity along the same line, displayed from 0.10 to 0.30, shows a clearly banded response below 800 ms. Two low-porosity bands, with values of approximately 0.14, are developed between about 1,200 and 1,500 ms and between about 2,200 and 2,450 ms, and these are separated by an interval of higher porosity of approximately 0.22 centred near 1,700 ms. Below 2,500 ms total porosity rises again to approximately 0.23. The banding

follows the interpreted layering instead of cutting across it, as expected where the transform is tracking lithology (Figure 4.36).

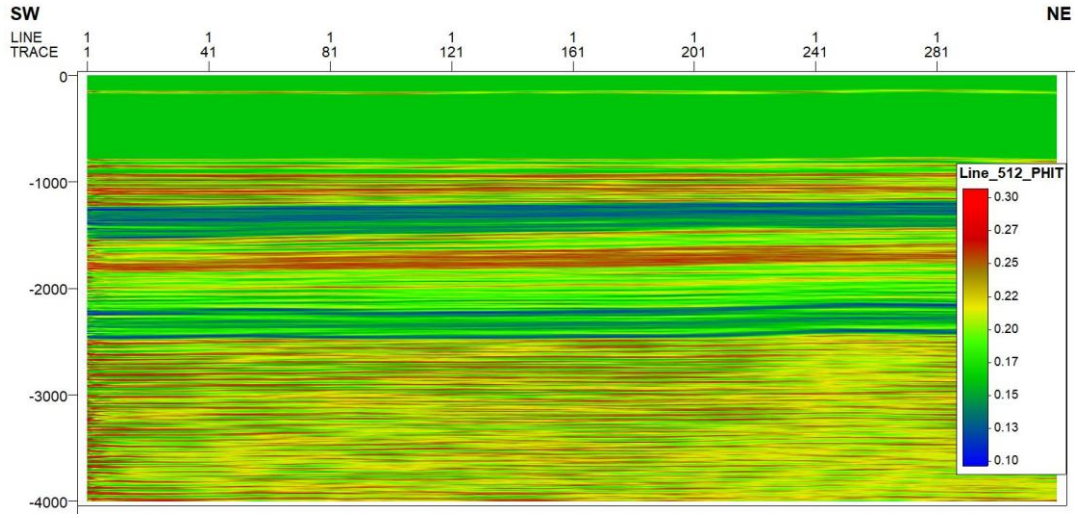



Figure 4. 18 Predicted total porosity along line TJ-89-512, calibrated at Kadanwari-03, displayed on a scale from 0.10 to 0.30.

The effective-porosity section is displayed from 0.04 to 0.20 and reproduces the same banding, as it must, since effective porosity is derived from total porosity and shale volume and is predicted from the same impedance. Effective porosity through the Lower Goru interval between 2,200 and 2,500 ms is approximately 0.07 to 0.08, against values of approximately 0.12 to 0.13 in the intervals immediately above and below. The reservoir interval on this line is predicted as a relative porosity low rather than a high, which does not agree with the low-impedance zone identified over the same interval in Figure 4.24 and is examined further in Section 4.5.4 (Figure 4.37).

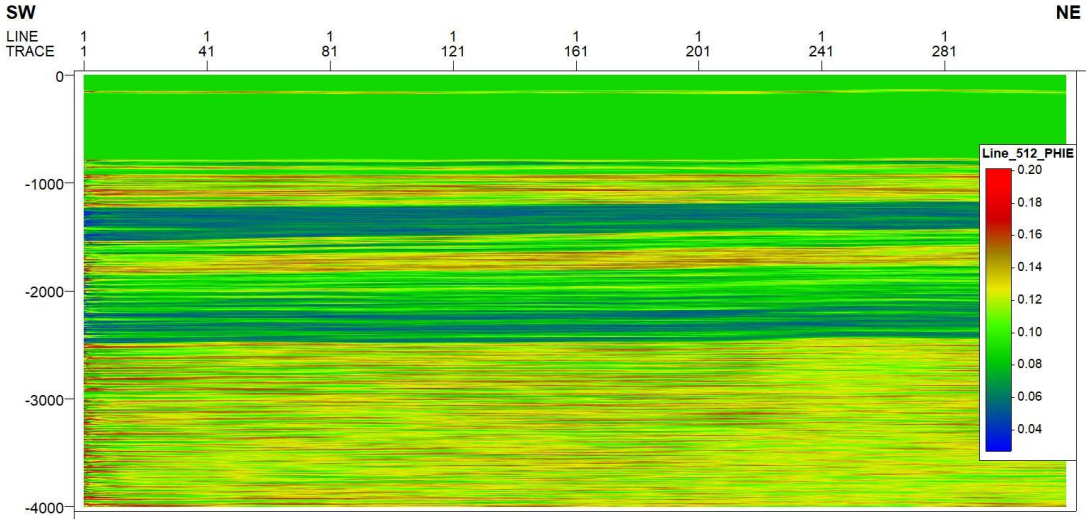



Figure 4. 19 Predicted effective porosity along line TJ-89-512, calibrated at Kadanwari-03, displayed on a scale from 0.04 to 0.20.

Water saturation is displayed from 0.30 to 1.00, with the highest saturations in blue. Most of the section stands at or close to the upper limit of the scale, and the only intervals in which saturation falls appreciably are the two low-porosity bands identified above, where values decrease to approximately 0.83 to 0.88. Saturation decreases where porosity decreases along this line (Figure 4.38).

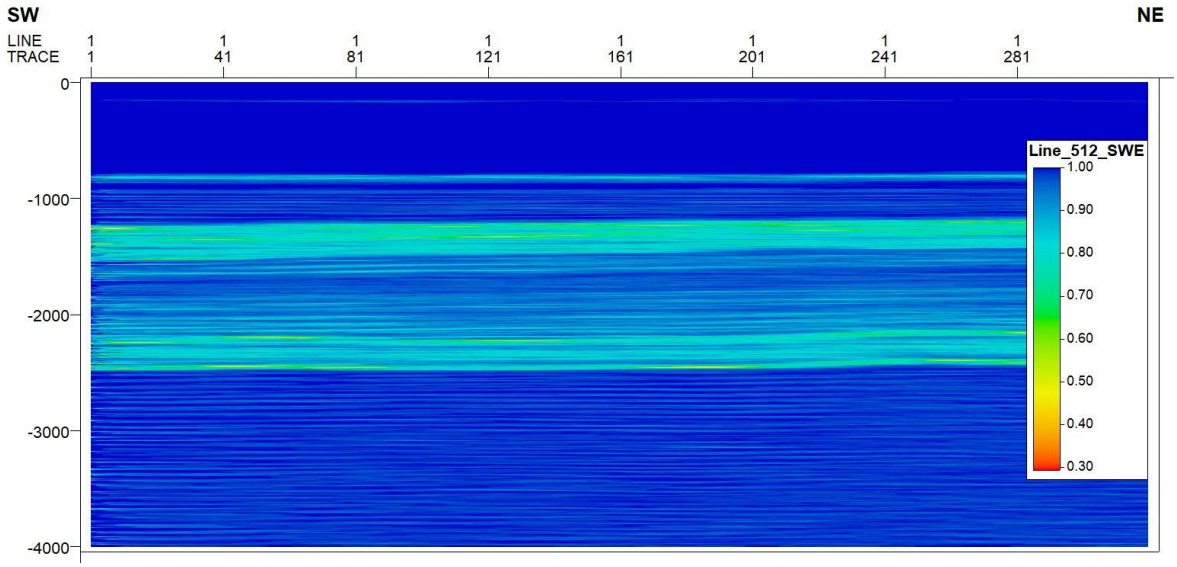



Figure 4. 20 Predicted water saturation along line TJ-89-512, calibrated at Kadanwari-03, displayed on a scale from 0.30 to 1.00; blue denotes the highest saturations.

The Premeability section is displayed from 0.0 to 42.000 and and is calculated in between from Upper Goru to Chiltan. Permeability through the Lower Goru interval shows relatively high permeability zone. These results are unreliable due to skewness of data.

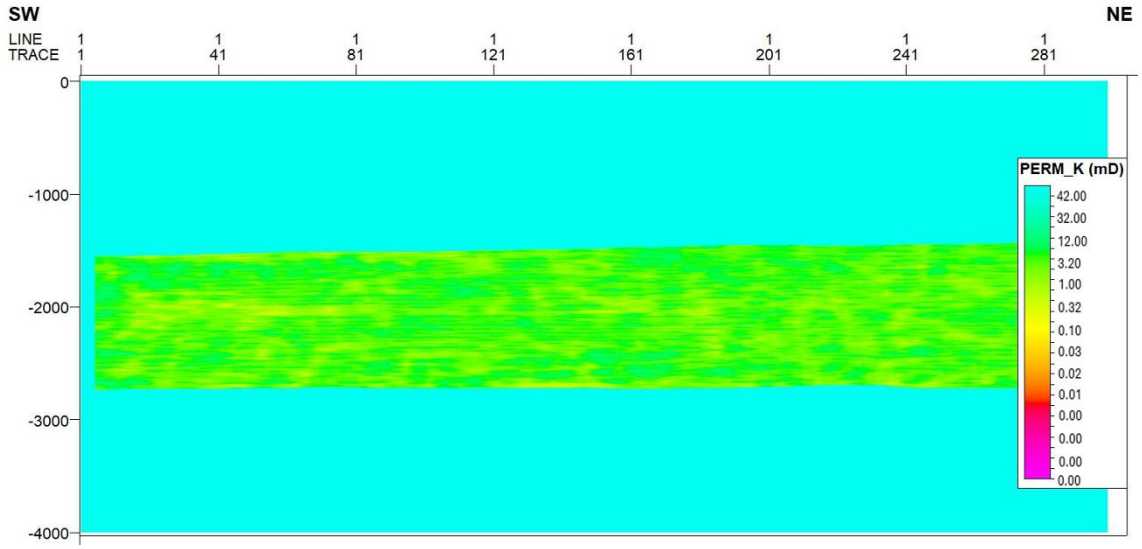



Figure 4. 21 Predicted Premeability along line TJ-89-512, calibrated at Kadanwari-03, displayed on a scale from 0.00 to 42.00.

### 4.4.2 Line TJ-89-516 (Kadanwari-01)

The shale-volume section along TJ-89-516 is displayed from 0.25 to 0.75. Below about 1,300 ms the section is strongly layered, with shale volume of approximately 0.58 through the interval from 1,500 to 2,200 ms. Between about 2,400 and 2,500 ms shale volume falls to approximately 0.40, the lowest value in the Lower Goru interval on this line, and the reduction can be followed along the full length of the section. This is the cleanest interval predicted on any of the three lines and it lies at the level of the reservoir target (Figure 4.40).

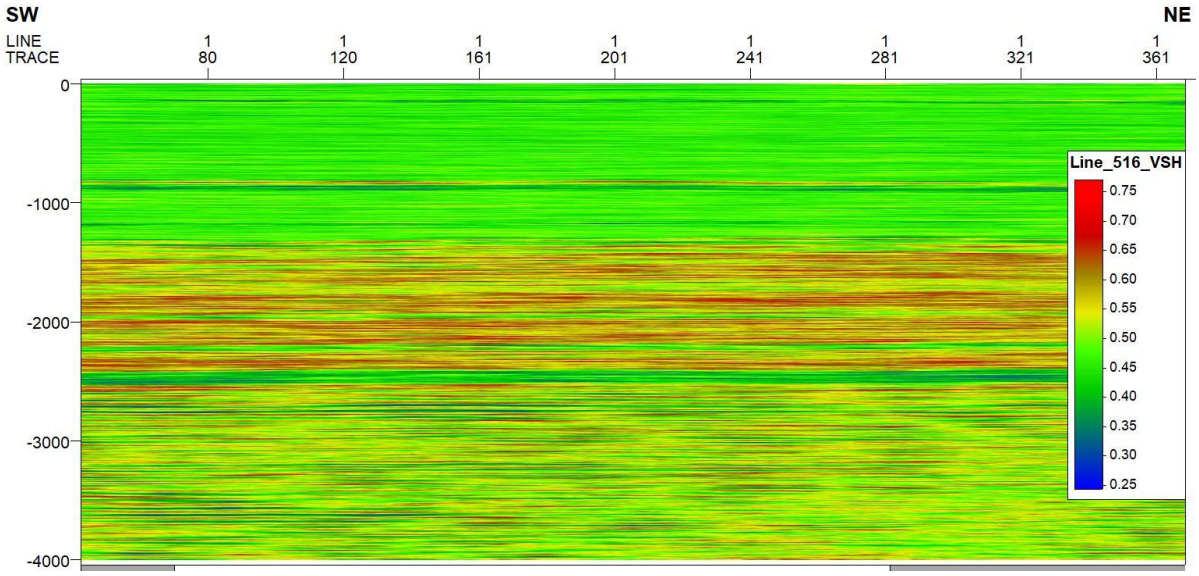



Figure 4. 22 Predicted volume of shale along line TJ-89-516, calibrated at Kadanwari-01, displayed on a scale from 0.25 to 0.75.

Total porosity on this line runs from 0.15 to 0.65 on the display scale. The upper part of the section, above approximately 1,300 ms, carries values between 0.39 and 0.54, which are far above any porosity that a consolidated sandstone at this depth could support and which are read as an artefact of prediction outside the calibrated impedance range, not as a result. Below 1,500 ms the values become physically reasonable and stabilise at approximately 0.17 to 0.19, with a slight increase to approximately 0.19 between 2,400 and 2,500 ms (Figure 4.41).

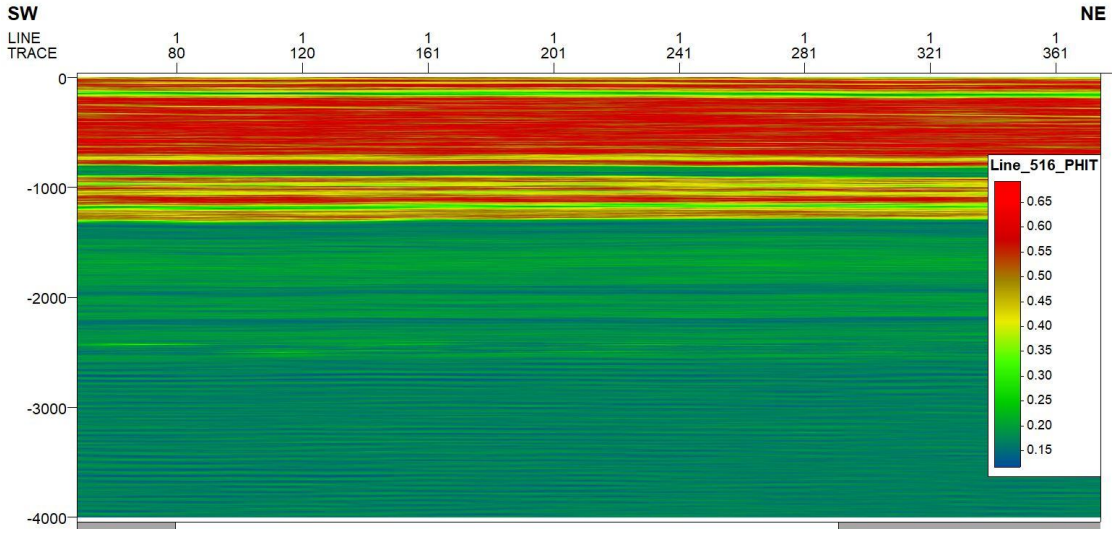



Figure 4. 23 Predicted total porosity along line TJ-89-516, calibrated at Kadanwari-01, displayed on a scale from 0.15 to 0.65; values above approximately 1,300 ms lie outside the calibrated range.

The effective-porosity section, displayed from 0.10 to 0.60, shows the same unconstrained response in the shallow section and the same stabilisation below 1,500 ms, where values of approximately 0.09 predominate. Between about 2,400 and 2,500 ms effective porosity rises to approximately 0.13, coincident with the shale-volume minimum of Figure 4.37 and with the low-impedance zone reported between 2,400 and 2,600 ms in Figure 4.32. This is the clearest reservoir response obtained from the machine-learning prediction on any line (Figure 4.42).

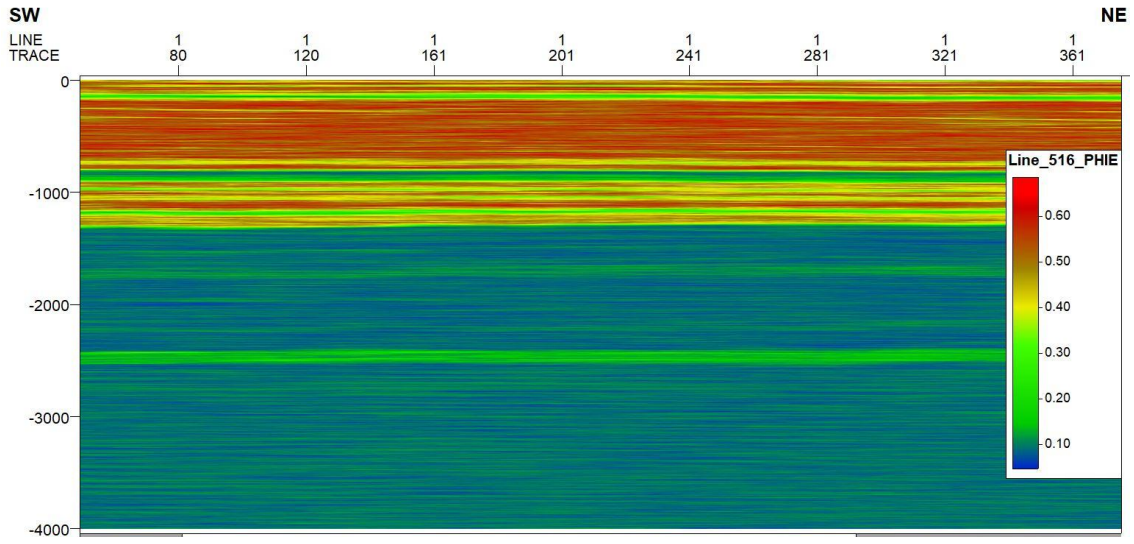



Figure 4. 24 Predicted effective porosity along line TJ-89-516, calibrated at Kadanwari-01, displayed on a scale from 0.10 to 0.60; the elevated values between approximately 2,400 and 2,500 ms coincide with the low-impedance zone of Figure 4.32.

The water-saturation section is displayed from 0.30 to 0.85. Saturation is approximately 0.74 through the interval from 1,500 to 2,200 ms and falls to approximately 0.53 between 2,400 and 2,500 ms, over the same interval in which shale volume is lowest and effective porosity highest. On this line the three properties combine into the configuration expected of a reservoir sand, with the qualification that all three are transforms of the same impedance and are not independent of one another (Figure 4.43).

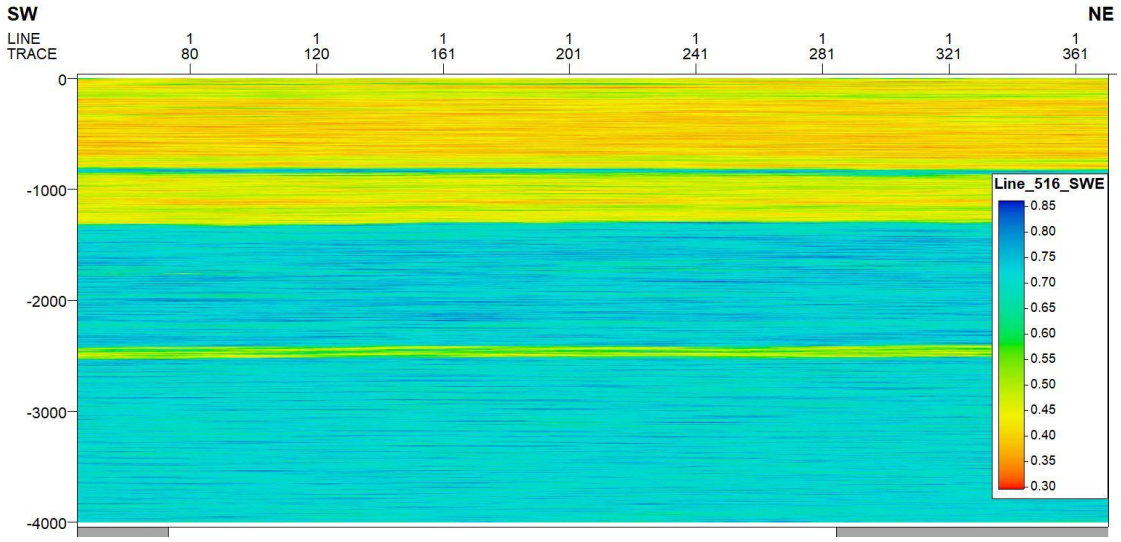



Figure 4. 25 Predicted water saturation along line TJ-89-516, calibrated at Kadanwari-01, displayed on a scale from 0.30 to 0.85; blue denotes the highest saturations.

The Premeability section is displayed from 0.0 to 42.000 and and is calculated in between from Upper Goru to Chiltan. Permeability in the Lower Goru Sand interval showing predominantly 10–35 mD, indicating relatively good reservoir quality. These results are unreliable due to the skewness of the log data.

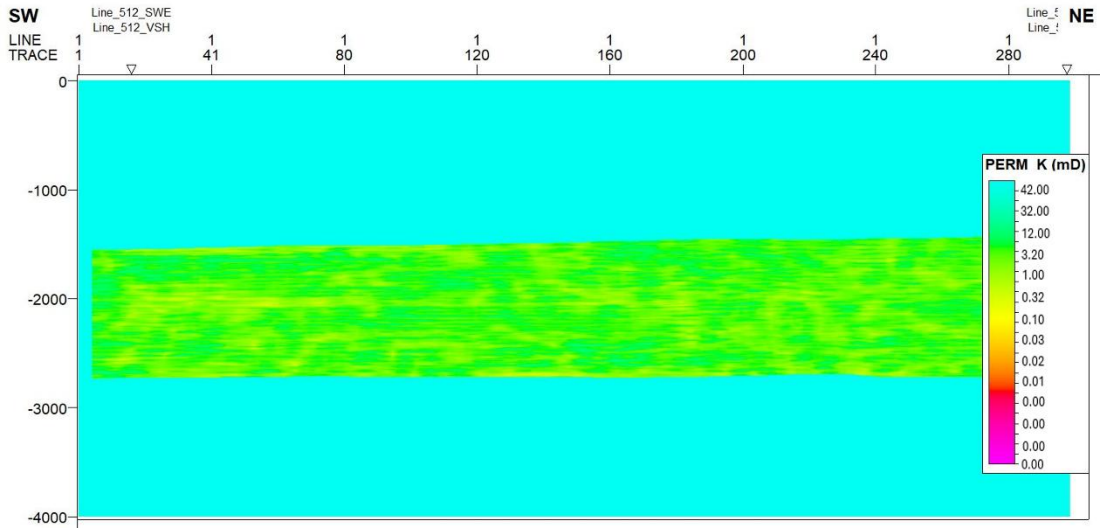


Figure 4. 26 Predicted Permeability along line TJ-89-516, calibrated at Kadanwari-01, displayed on a scale from 0.00 to 42.00.

### 4.4.3 Line TJ-89-526 (Kadanwari-04)

The shale-volume section along TJ-89-526 is displayed from 0.25 to 0.75. Above approximately 850 ms the section is saturated at the lower limit of the scale and carries no information. Below that level shale volume varies between approximately 0.50 and 0.59, and from about 1,900 ms downward the section becomes almost uniform at approximately 0.56, with no variation that can be related to the Lower Goru sand units (Figure 4.45).

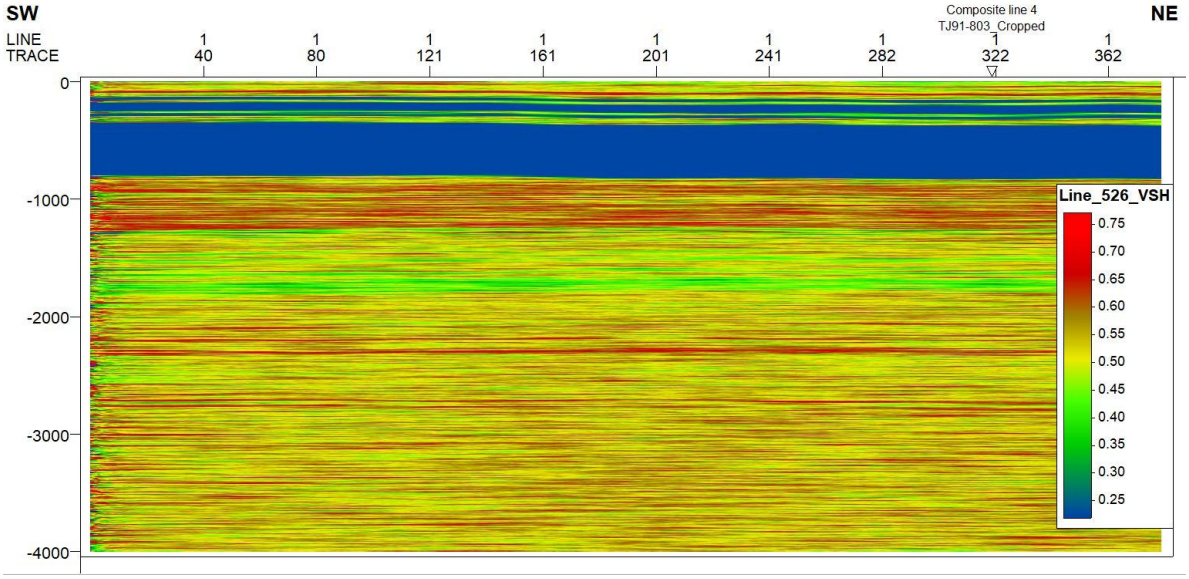



Figure 4. 27 Predicted volume of shale along line TJ-89-526, calibrated at Kadanwari-04, displayed on a scale from 0.25 to 0.75.

The total-porosity section, displayed from 0.15 to 0.40, shows the same behaviour. Values of approximately 0.32 are predicted between 900 and 1,200 ms, decreasing through the interval from 1,200 to 1,900 ms, and below approximately 1,900 ms the section stabilises at approximately 0.18 and remains effectively constant to the base of the display (Figure 4.46).

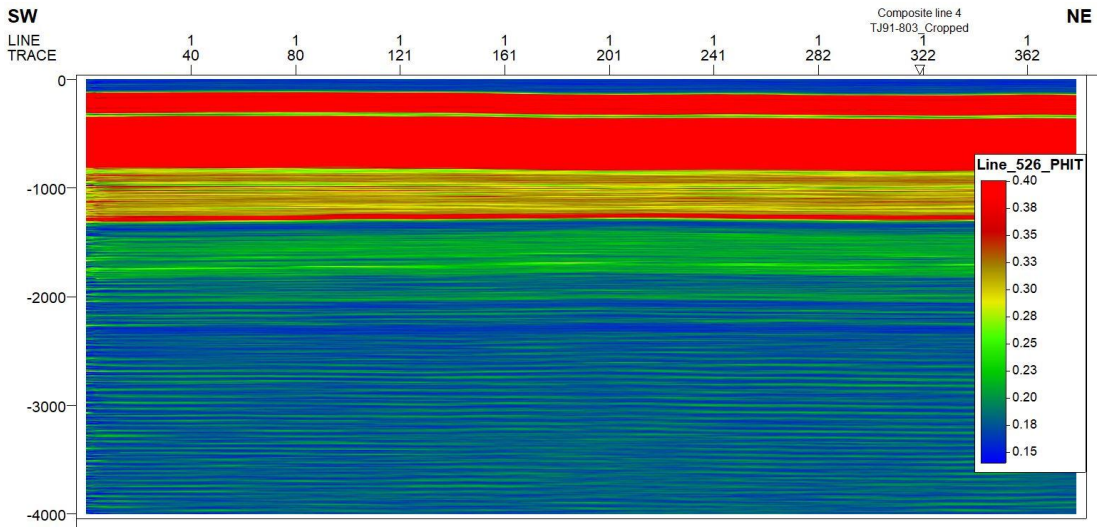



Figure 4. 28 Predicted total porosity along line TJ-89-526, calibrated at Kadanwari-04, displayed on a scale from 0.15 to 0.40.

The effective-porosity section, displayed from 0.05 to 0.30, is likewise featureless below approximately 1,900 ms, where values remain close to 0.08 throughout the Lower Goru interval and show no increase at the level of the B sand. The absence of any predicted response follows from the log coverage at the calibrating well: as recorded in Section 3.2, Kadanwari-04 reaches the top of the Lower Goru Formation without penetrating the individual sand units, so the training set for this line contains no samples of the reservoir interval. A model that has never seen the rock cannot predict its properties, and the flat response below the logged section is the expected consequence, not evidence that the reservoir is absent (Figure 4.47).

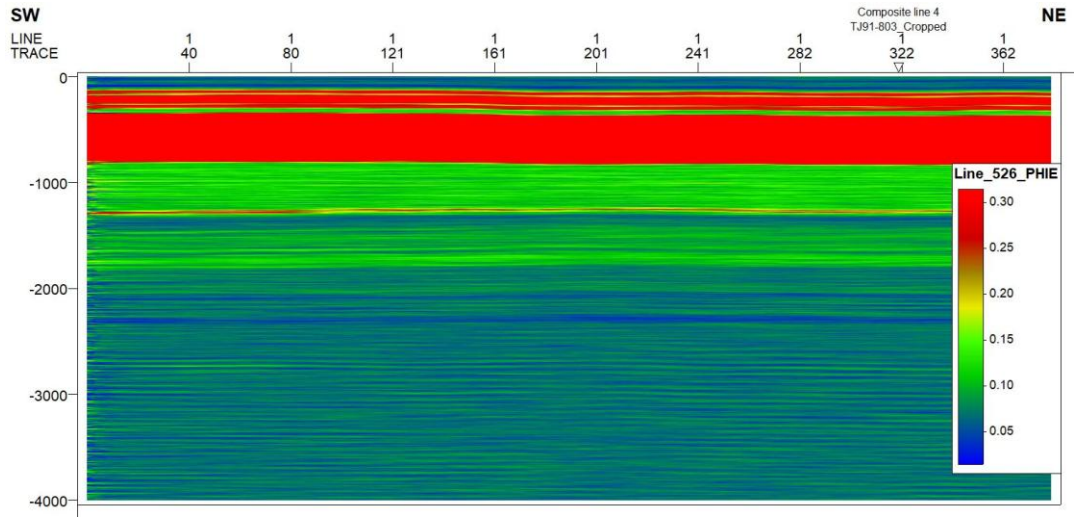



Figure 4. 29 Predicted effective porosity along line TJ-89-526, calibrated at Kadanwari-04, displayed on a scale from 0.05 to 0.30; the response below approximately 1,900 ms is effectively uniform.

The water-saturation section, displayed from 0.45 to 0.95, repeats the pattern, with saturations of approximately 0.90 between 900 and 1,200 ms and a constant value of approximately 0.78 below 1,900 ms. No interval of reduced saturation is developed at reservoir level (Figure 4.48).

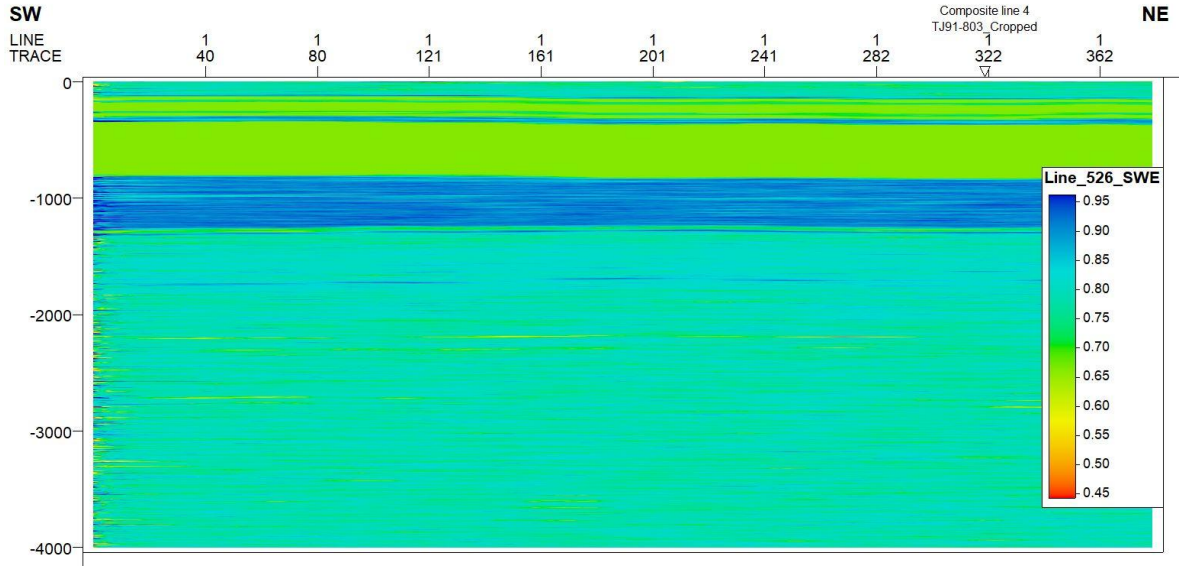



Figure 4. 30 Predicted water saturation along line TJ-89-526, calibrated at Kadanwari-04, displayed on a scale from 0.45 to 0.95; blue denotes the highest saturations.

The Premeability section is displayed from 0.0 to 42.000 and and is calculated in between from Upper Goru to Chiltan. Permeability in the Lower Goru Sand interval is relatively high.

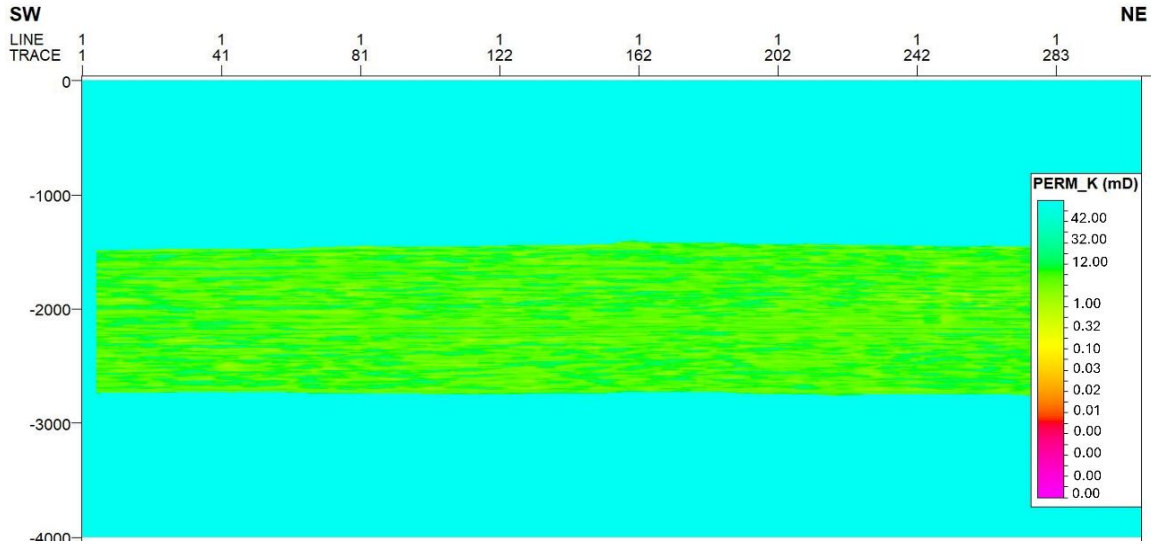



Figure 4. 31 Predicted Permeability along line TJ-89-526, calibrated at Kadanwari-04, displayed on a scale from 0.00 to 42.00.

### 4.4.4 Summary of the Machine Learning Results

The three lines do not give a uniform result, and the differences between them follow from the log control at the calibrating wells. Line TJ-89-516, tied to the only well that penetrates the B sand, returns a coherent reservoir response between approximately 2,400 and 2,500 ms, with effective porosity of approximately 0.13, shale volume of approximately 0.40 and water saturation of approximately 0.53, coincident with the low-impedance zone identified independently in Section 4.4. Line TJ-89-526, tied to a well that does not reach the sand units, returns no resolvable response at reservoir level. Line TJ-89-512 returns a banded section in which the Lower Goru interval appears as a relative porosity low.

The result on TJ-89-512 requires comment, because it runs opposite to the inversion. The inverted section along that line carries a low-impedance zone through the same interval, which would ordinarily indicate elevated porosity, whereas the trained model maps that interval to reduced effective porosity and reduced water saturation together. Since both predictions derive from the same impedance values, the disagreement lies in the transform rather than in the data, and it indicates that the relationship learned at Kadanwari-03 does not carry the same sense as the relationship learned at Kadanwari-01. The predicted sections along TJ-89-512 are therefore used qualitatively in what follows, and the porosity carried into the volumetric estimate of Section 4.7 is taken from the line and the well that constrain the B sand directly.

This leaves three limitations, all of which apply to the sections that follow. The predicted properties on any line are transforms of a single impedance attribute and are not independent of one another, so their coincidence cannot be used as mutual confirmation. The colour scales differ between lines, so colours cannot be compared from one section to another and only the quoted values are comparable. And the predictions are reliable only within the impedance range represented in the training data, which restricts them to the logged intervals and excludes the shallow parts of all three sets of sections.

Machine learning was used to estimate shale volume, porosity, water saturation, and permeability from the available well-log and petrophysical data. However, variations in data quality, missing logs, and skewed well data introduced some uncertainty into the predicted results. To improve the interpretation, the ML results were integrated with seismic inversion results, which provided a more continuous representation of the reservoir properties. The combined results helped identify the overall reservoir trends and improve confidence in the interpretation where well data were limited.

## 4.5 Seismic Inversion

Model-based inversion was carried out in the Hampson-Russell suite along the three lines carrying well control, following the procedure of Section 3.5. The results are presented below in the order in which the inversion was run: the extracted wavelet, the initial low-frequency model, the comparison between the inverted and the upscaled impedance logs, the cross-plot of inverted against original impedance, and the inverted section. The reservoir properties predicted from the inverted impedance by machine learning are presented in Section 4.5.

### 4.5.3 Kadanwari-01 (Line TJ-89-516)

Kadanwari-01 lies on line TJ-89-516 at coordinates 525,485.87 m east and 3,002,164.22 m north, with a kelly bushing elevation of 60.0 m and a seismic reference datum of 52.0 m. It is the only well of the three that penetrates the full Lower Goru sand succession through to the B sand, and it therefore carries the log control on which the predicted properties at reservoir level ultimately depend.

The wavelet extracted over the Kadanwari-01 tie window shows the same zero-phase character as the wavelet used on the other two lines, with a bandwidth of approximately 10 to 60 Hz and dominant energy between 30 and 35 Hz. The symmetry of the time response about zero time confirms that the phase estimate is stable, and the comparable bandwidth at all three wells indicates that a single wavelet character is representative of the survey. Frequencies below approximately 10 Hz are again absent as a result of the low-cut filter applied during processing (Figure 4.37).

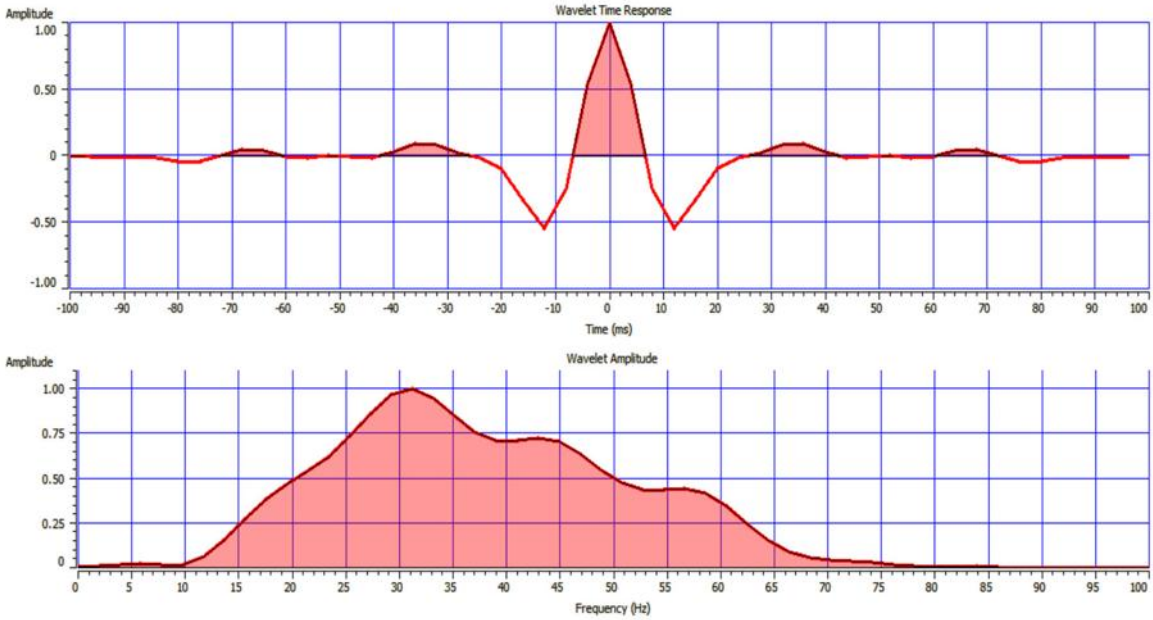



Figure 4. 32 Wavelet extracted over the Kadanwari-01 well-tie window, showing the time response (upper) and the amplitude spectrum (lower).

The seismic-to-well tie at Kadanwari-01 was constructed from the density log displayed from 1.5 to 3.0 g/cc, the corrected P-wave velocity from 1,000 to 6,000 m/s and the volume of shale from 0 to 1 v/v, with the synthetic seismogram shown against the trace extracted from the cropped TJ-89-516 volume between CDP 315 and CDP 355. This is the only tie at which the full sand succession is posted: the H, G, F, E, D, C and B sand tops are carried between approximately 2,200 and 2,510 ms, over a true vertical depth range of approximately 2,750 to 3,500 m, and they project onto consistent seismic events. The cross-correlation was computed over a window of 1,270 to 2,500 ms with a lag of ±50 ms and returns a maximum coefficient of 0.585 at zero lag with a phase rotation of zero degrees. This is the lowest of the three correlations, which is consistent with the more strongly interbedded log character described in Section 4.2.1, but the zero-lag maximum and zero-degree rotation confirm that the tie is correctly phased. The strong reflection at the Upper Goru level and the group of high-amplitude events at the B sand level provide the two anchors used when the horizons were carried away from the well (Figure 4.38).

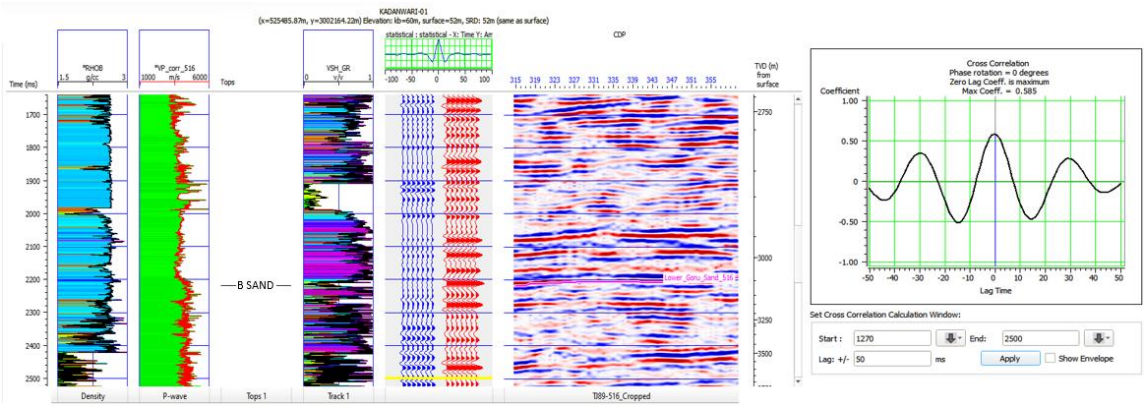



Figure 4. 33 Seismic-to-well tie for Kadanwari-01 on line TJ-89-516, showing the density, P-wave velocity and volume of shale tracks with the H to B sand tops posted, the synthetic seismogram against the extracted seismic trace, and the cross-correlation function computed over the 1,270 to 2,500 ms window.

The initial low-frequency model along TJ-89-516 was generated from the interpreted horizons with the upscaled P-impedance from Kadanwari-01 interpolated between them. The model is displayed from CDP 323 to CDP 811 at a horizontal scale of approximately 1:62,085, with the well at approximately CDP 761, and it extends from the Khadro to the Chiltan level over an impedance range of approximately 6,000 to 11,927 (m/s)(g/cc). This line is the longest of the three, and the low-frequency trend accordingly carries more lateral structure than the models along TJ-89-512 and TJ-89-526 (Figure 4.39).

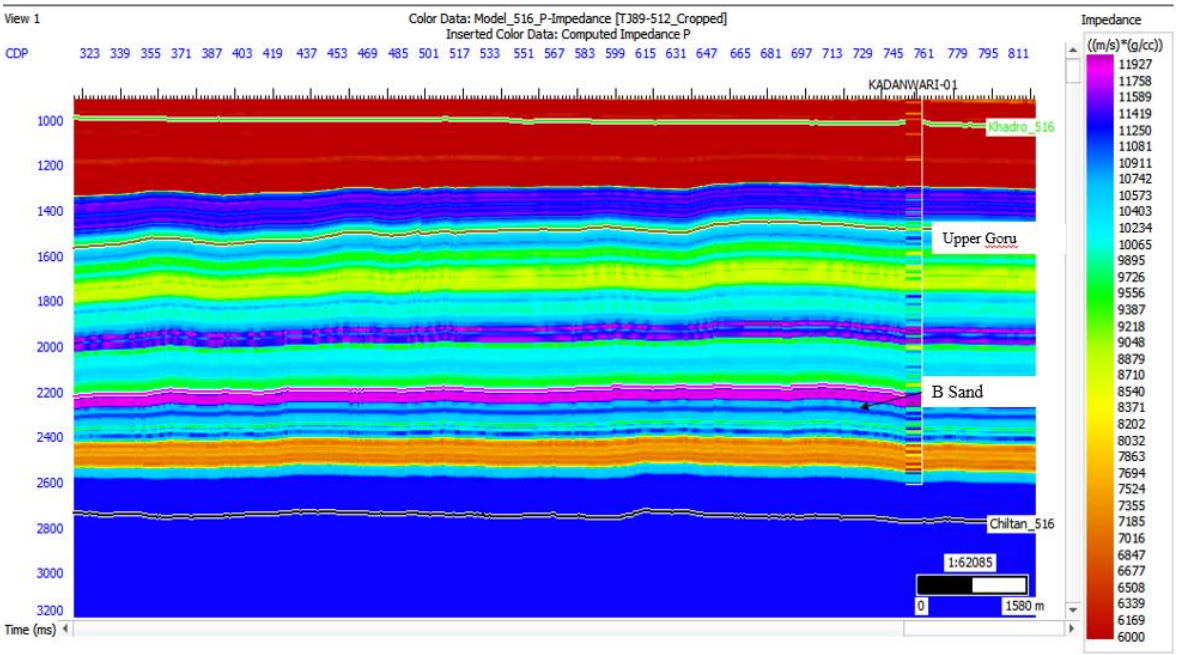



Figure 4. 34 Initial low-frequency impedance model along line TJ-89-516, built from the interpreted horizons and the upscaled impedance log at Kadanwari-01.

Log upscaling was checked at Kadanwari-01 by comparing the blocked P-impedance log with the synthetic seismogram and the extracted seismic trace at CDP 315. The correlation obtained is 0.9965 and the residual error is 0.083, with an impedance error of 2,375.59 (m/s)(g/cc) on a log track spanning 1,974.02 to 22,968 (m/s)(g/cc). The correlation confirms that the blocking has not removed impedance contrasts that the seismic data are able to resolve. The formation tops posted on the display, from the shale unit and the Lower Goru top at approximately 1,560 to 1,600 ms through to the H, G, F, E and D sands between approximately 2,200 and 2,400 ms, provide the depth-to-time calibration used in the inversion (Figure 4.40).

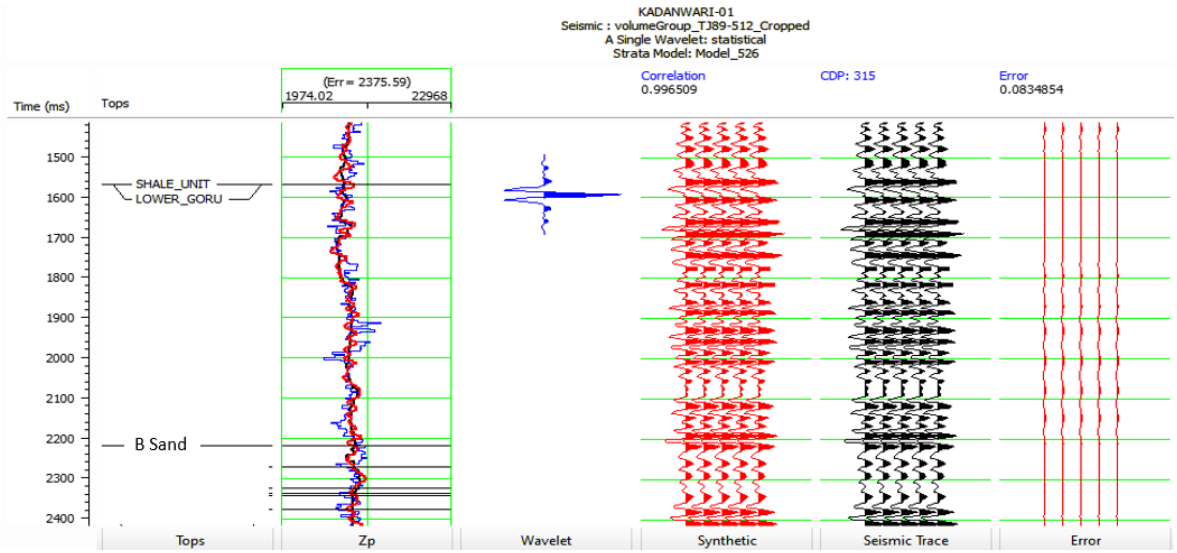



Figure 4. 35 Log upscaling quality control at Kadanwari-01, comparing the upscaled P-impedance log with the synthetic seismogram and the extracted seismic trace at CDP 315.

The cross-plot of inverted against original impedance at Kadanwari-01 spans an impedance range of approximately 1,500 to 16,000 (m/s)(g/cc) and returns an error of 2,375.59 (m/s)(g/cc) about the 45-degree reference line, reducing to 1,150.06 for the best-fit regression, which has a gradient of 0.3483 and an intercept of 6,528.12. The scatter about the reference line is the largest of the three wells and the regression gradient is the shallowest, so the compression of the dynamic range is most severe here. This matches the more strongly interbedded log character described in Section 4.2.1 and the lower well-tie correlation obtained at this well, and it means that absolute impedance values along this line should be treated with more caution than those along TJ-89-512 and TJ-89-526, and that the section is better used for its lateral variation than for its absolute values (Figure 4.41).

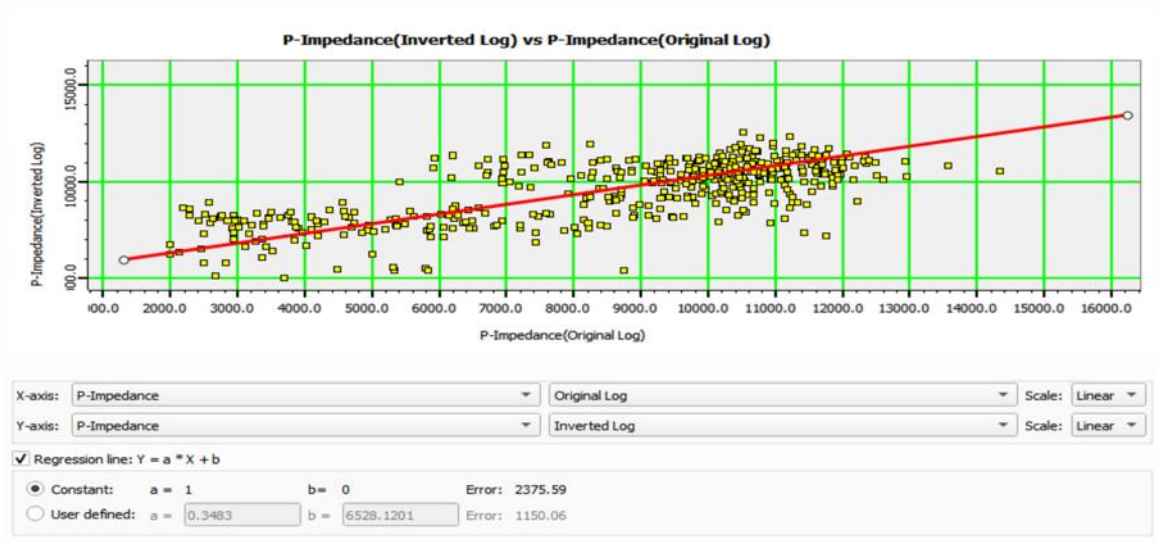



Figure 4. 36 Cross-plot of inverted P-impedance against original P-impedance at Kadanwari-01, with the 45-degree reference line and the best-fit regression.

The inverted section along TJ-89-516 is displayed from CDP 323 to CDP 819 at a horizontal scale of approximately 1:61,146, with Kadanwari-01 at approximately CDP 761 and all interpreted horizons posted, on the same colour scale of 6,000 to 11,927 (m/s)(g/cc). A laterally continuous zone of low impedance of approximately 7,500 to 8,200 (m/s)(g/cc) is developed beneath the Lower Goru Sand horizon between approximately 2,450 and 2,600 ms, shown in orange, and is enclosed above and below by the higher impedance values shown in cyan and blue. The impedance values within this zone are lower than those observed on the other two lines, which is consistent with the more gas-affected log response recorded at Kadanwari-01. The inverted impedance at the well agrees closely with the measured impedance log, which validates the result at the tie point (Figure 4.42).

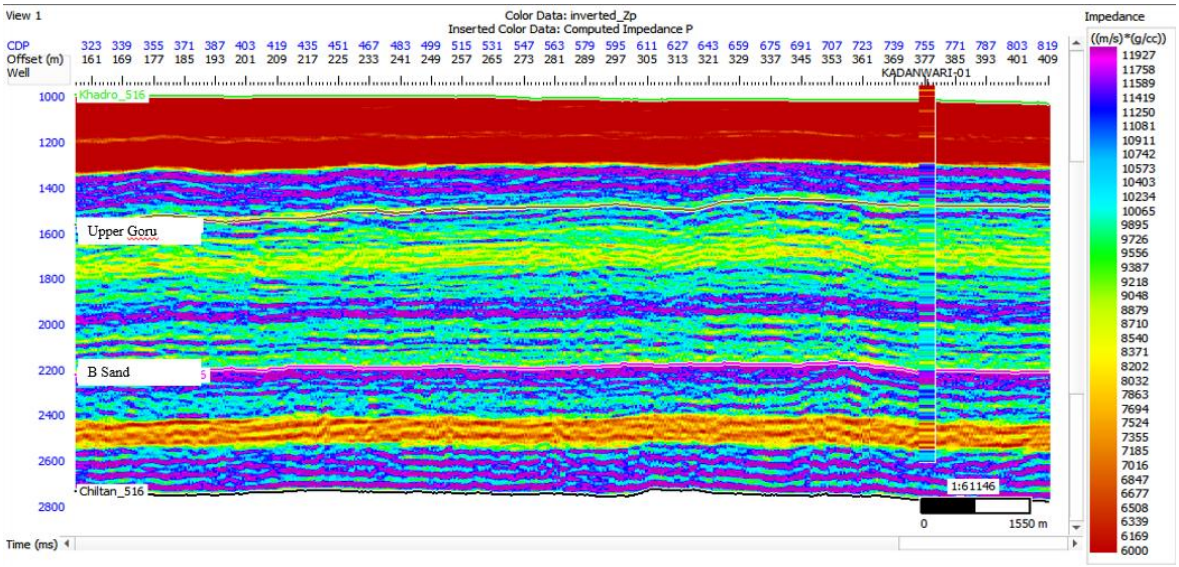



Figure 4. 37 Inverted P-impedance section along line TJ-89-516 with Kadanwari-01 tied at the well location; the low-impedance zone beneath the Lower Goru Sand horizon is highlighted.

The predicted volume of shale along TJ-89-516 is displayed on a scale from 0.4428 to 0.7383 v/v. A green band of low shale volume at approximately 0.44 to 0.48 occupies the interval from approximately 1,000 to 1,300 ms, above the logged section, and below approximately 1,400 ms the section is heavily mottled with the alternating low and high values characteristic of a strongly interbedded succession. Within the Lower Goru interval a distinctly cleaner band is developed between approximately 2,400 and 2,600 ms, where shale volume falls to approximately 0.45 to 0.52 and the response is more continuous laterally than elsewhere on the section. This is the cleanest interval predicted on any of the three lines, and it lies at the level of the reservoir target and can be followed along the full length of the section (Figure 4.43).

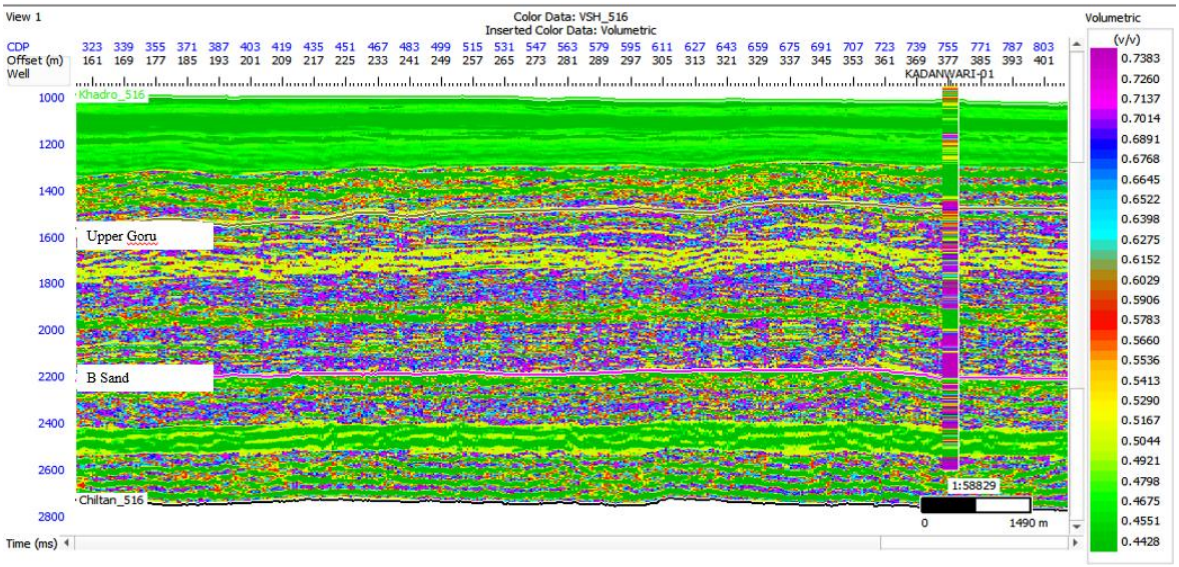



Figure 4. 38 Predicted volume of shale along line TJ-89-516, calibrated at Kadanwari-01, displayed on a scale from 0.4428 to 0.7383 v/v.

The predicted porosity section along TJ-89-516 is displayed from 0.0280 to 0.4000 v/v. Above approximately 1,350 ms the section carries values of approximately 0.35 to 0.40 shown in magenta; these are far above any porosity that a consolidated sandstone at this depth could support and are read as an artefact of prediction outside the calibrated impedance range, not as a result. Between approximately 1,400 and 2,350 ms the values become physically reasonable and stabilise at approximately 0.11 to 0.14 in yellow, interrupted by red bands of approximately 0.17 to 0.19. The highlighted interval between approximately 2,430 and 2,590 ms carries the highest physically reasonable porosities on the section, approximately 0.24 to 0.28, shown as laterally continuous cyan bands interleaved with dark red laminae of approximately 0.19 to 0.21. These are coincident with the shale-volume minimum of Figure 4.43 and with the low-impedance zone of Figure 4.42, and they constitute the clearest reservoir response obtained from the property prediction on any line (Figure 4.44).

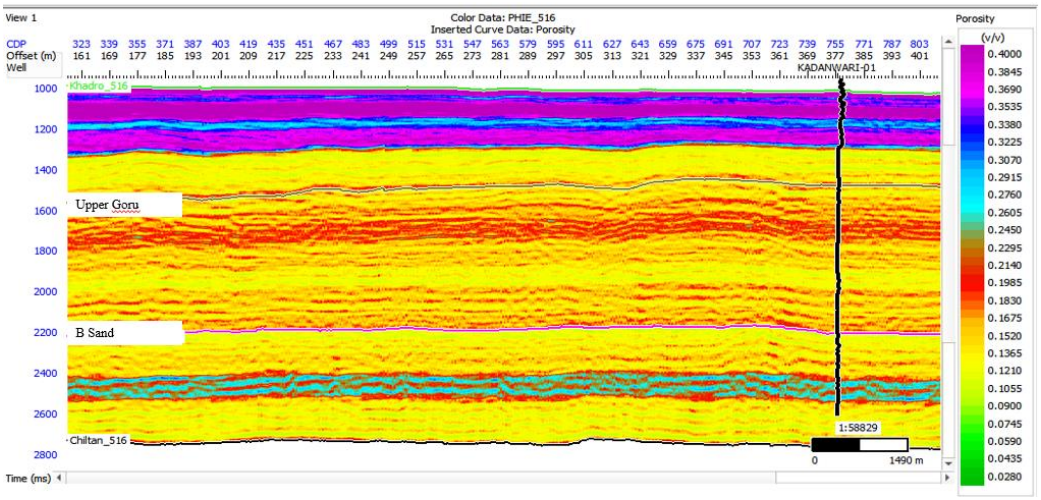



Figure 4. 39 Predicted porosity along line TJ-89-516, calibrated at Kadanwari-01, displayed on a scale from 0.0280 to 0.4000 v/v.

The predicted water saturation along TJ-89-516 is displayed from 0.5205 to 0.9056 v/v. A yellow band of approximately 0.58 occupies the interval from approximately 1,050 to 1,300 ms, above the logged section and outside the calibrated range. Between approximately 1,400 and 2,350 ms saturation stands at approximately 0.80 to 0.85 in blue-grey, and it falls to approximately 0.60 to 0.65, shown in green, between approximately 2,350 and 2,550 ms, over the same interval in which shale volume is lowest and porosity highest. On this line the three properties combine into the configuration expected of a reservoir sand, with the qualification that all three are transforms of the same impedance and are not independent of one another (Figure 4.45).

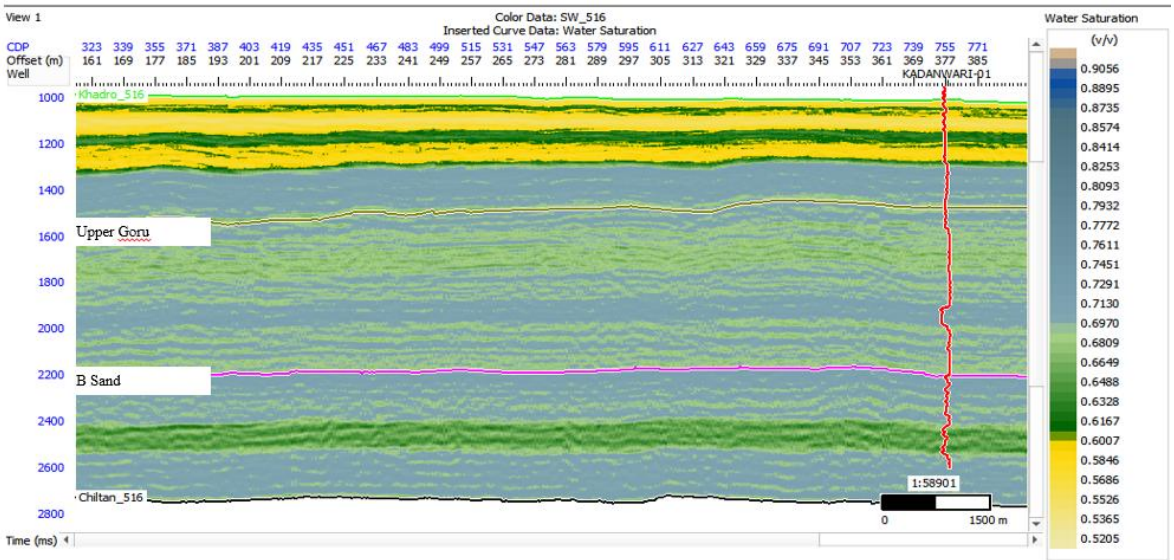



Figure 4. 40 Predicted water saturation along line TJ-89-516, calibrated at Kadanwari-01, displayed on a scale from 0.5205 to 0.9056 v/v; dark blue denotes the highest saturations.

The predicted permeability section along TJ-89-516 is displayed from 0.0 to 40.0 mD and is calculated over the interval from the Upper Goru to the Chiltan level. Above approximately 1,300 ms the section is uniformly magenta at values above 35 mD; this interval lies above the logged section and the values are unconstrained. Between approximately 1,400 and 2,350 ms the section is uniformly green at 0 to 5 mD. The highlighted interval between approximately 2,420 and 2,560 ms carries a strongly mottled band of predominantly 10 to 35 mD, with magenta values at and above 40 mD, that is developed along the full length of the section, indicating relatively good reservoir quality over the same interval in which porosity is highest, shale volume lowest and impedance lowest (Figure 4.46).

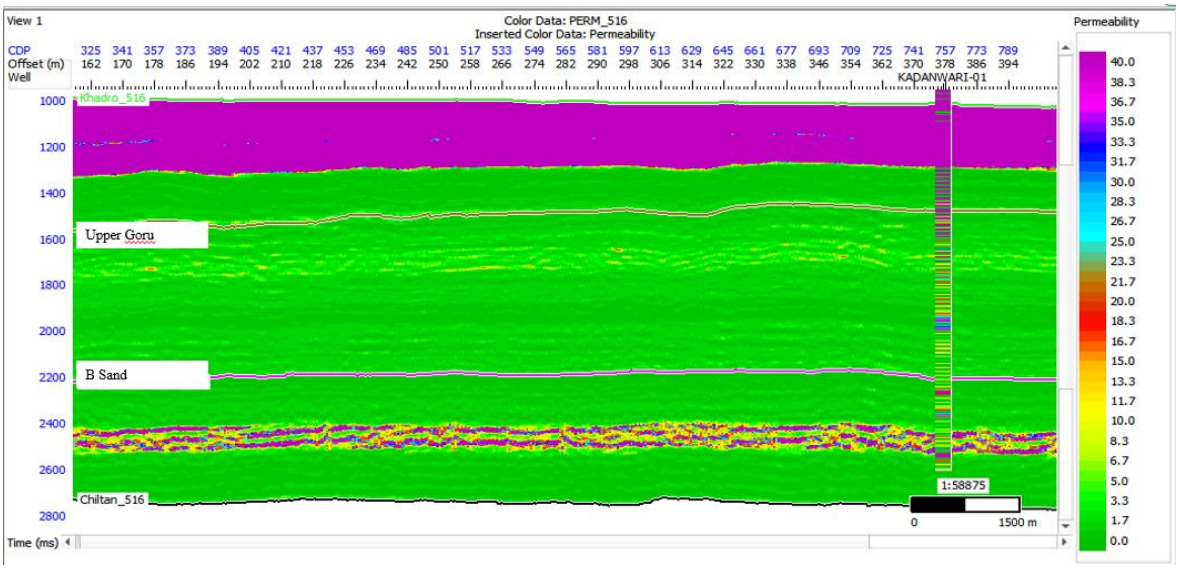



Figure 4. 41 Predicted permeability along line TJ-89-516, calibrated at Kadanwari-01, displayed on a scale from 0.0 to 40.0 mD.

### 4.5.1 Kadanwari-03 (Line TJ-89-512)

Kadanwari-03 lies on line TJ-89-512 at approximately CDP 440, at coordinates 519,568.00 m east and 3,003,825.00 m north, with a kelly bushing elevation of 59.59 m and a seismic reference datum of 50.59 m. The well returned the highest tie correlation and the lowest residual error of the three, and it is the well on which the inversion parameters were first established.

A statistical wavelet was extracted from the seismic data over the interval from the Khadro Formation to the Chiltan Limestone. The wavelet is zero phase and symmetrical about zero time, with the principal trough pair at approximately ±12 ms and low-amplitude side lobes beyond. Its amplitude spectrum gives a usable bandwidth of approximately 15 to

60 Hz, with the dominant energy at about 31 Hz and secondary shoulders near 43 and 56 Hz, falling away above 65 Hz. Frequencies below about 10 Hz are absent as a result of the low-cut filter applied during processing, and this is precisely the component that the low-frequency model must supply if absolute impedance is to be recovered (Figure 4.17).

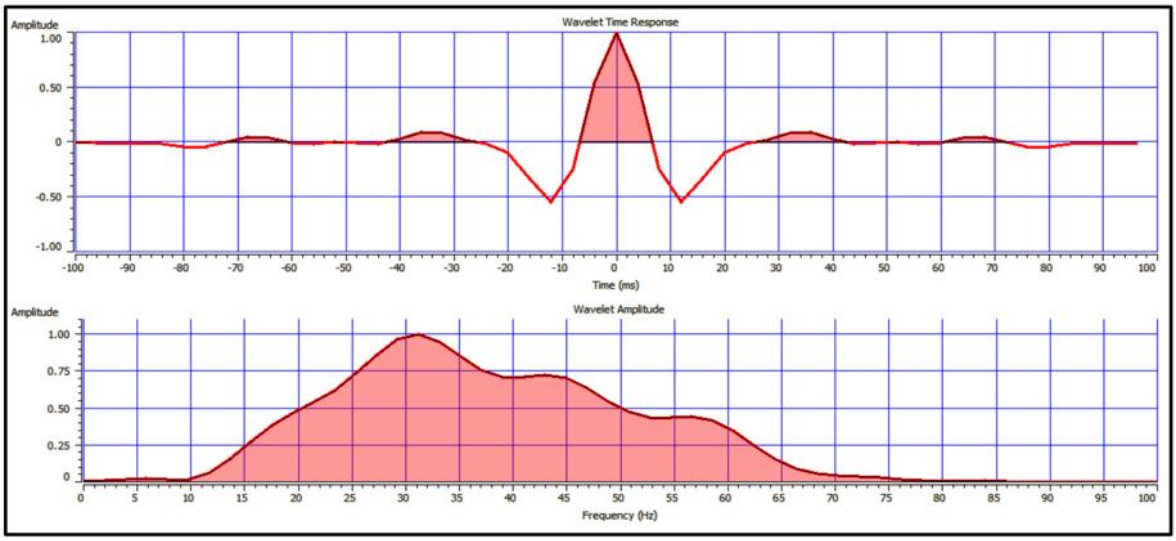



Figure 4. 42 Statistical wavelet extracted from the seismic data between the Khadro and Chiltan levels for the inversion at Kadanwari-03, showing the time response (upper) and the amplitude spectrum (lower).

The seismic-to-well tie was constructed from the density and corrected P-wave velocity logs, displayed over ranges of 1.5 to 3.0 g/cc and 1,000 to 7,000 m/s respectively, with the volume of shale computed from the gamma ray carried alongside on a scale of 0 to 1 v/v for lithological correlation. The synthetic seismogram generated from those logs is shown in blue against the seismic trace extracted along the borehole in red, with the corresponding panel of the cropped TJ-89-512 volume displayed from CDP 417 to CDP 457. The match is good across the Upper Goru and Lower Goru intervals, and the H sand top at approximately 2,235 ms is clearly resolved against the Lower Goru Sand horizon carried on the seismic panel. The cross-correlation was computed over a window of 1,100 to 2,400 ms with a lag of ±50 ms and returns a maximum coefficient of 0.691 at zero lag with a phase rotation of zero degrees. This is the highest correlation obtained at any of the three wells, and it follows from the more blocky log character described in Section 4.2.2, which produces a reflectivity series with stronger and more distinctive events. The zero-lag maximum and the zero-degree rotation together confirm that the extracted wavelet is zero phase (Figure 4.18).

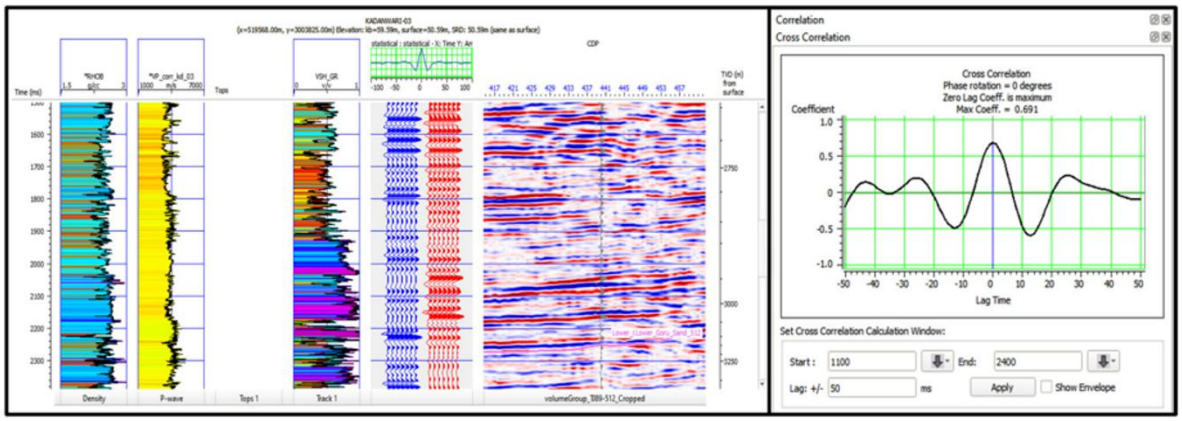



Figure 4. 43 Seismic-to-well tie for Kadanwari-03 on line TJ-89-512, showing the density, P-wave velocity and volume of shale tracks, the synthetic seismogram against the extracted seismic trace, and the cross-correlation function computed over the 1,100 to 2,400 ms window.

The initial low-frequency model along TJ-89-512 was built by interpolating the upscaled impedance from Kadanwari-03 between the interpreted horizons, which were used as stratigraphic layer boundaries, with a moving average of fifteen samples applied to the log. The model is displayed from CDP 246 to CDP 556 at a horizontal scale of approximately 1:36,177, extends from the Khadro to the Chiltan level, and covers an impedance range of approximately 6,000 to 11,927 (m/s)(g/cc). Because the model was built along the interpreted horizons and not on flat layers, its low-frequency trend follows the mapped structure, and the layering visible in the display reproduces the horizon geometry rather than imposing a false one (Figure 4.19).

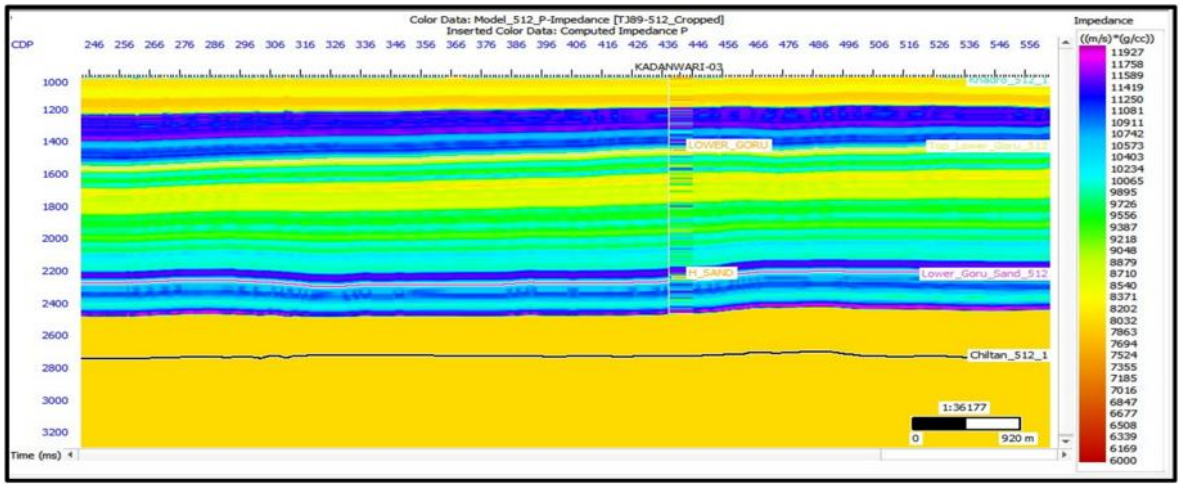



Figure 4. 44 Initial low-frequency impedance model along line TJ-89-512, built from the interpreted horizons and the upscaled impedance log at Kadanwari-03.

The inversion analysis at Kadanwari-03 compares the inverted impedance with the original and upscaled impedance logs and the synthetic generated from the inverted result with the seismic trace at CDP 440. The original impedance log is shown in blue, its upscaled or blocked equivalent in black and the inverted result in red, over an impedance range of 3,368.75 to 14,849.5 (m/s)(g/cc). The inverted curve follows the upscaled log closely over the whole analysis window from approximately 1,300 to 2,300 ms, and the residual trace shows no systematic structure that would indicate a biased solution. The correlation between the synthetic and the recorded trace is 0.9969 and the residual error is 0.079, with an associated impedance error of 1,516.89 (m/s)(g/cc) on the log track. These figures indicate that the inversion parameters reproduce the recorded data without the solution reverting to the initial model (Figure 4.20).

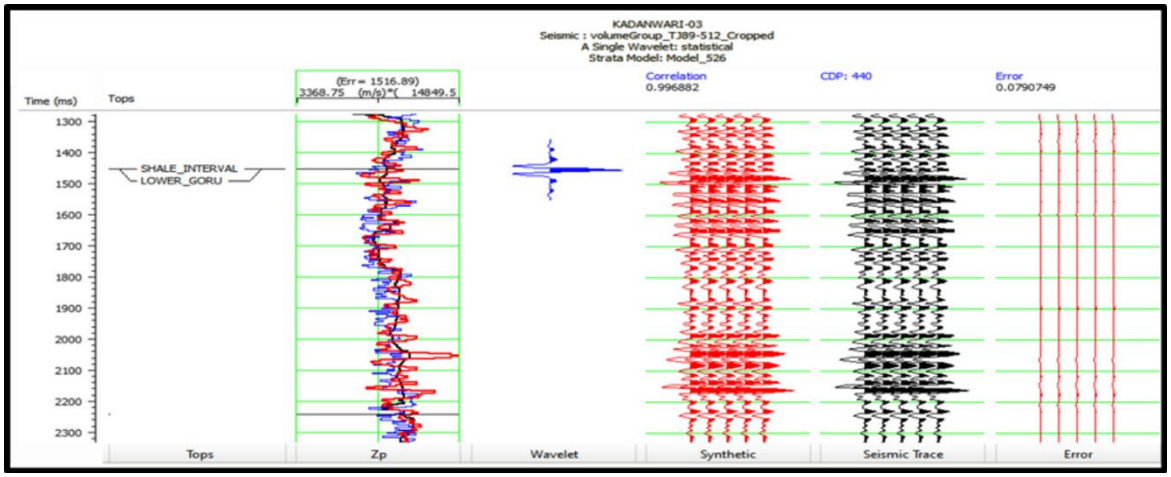



Figure 4. 45 Comparison of the inverted, upscaled and original impedance logs at Kadanwari-03, with the synthetic generated from the inverted result, the seismic trace at CDP 440 and the residual error.

The cross-plot of inverted against original impedance provides an independent check on the inversion at this well, with the original log on the horizontal axis and the inverted log on the vertical axis. The points are distributed about the 45-degree reference line over an impedance range of approximately 6,500 to 14,000 (m/s)(g/cc), and the error associated with that line is 1,516.89 (m/s)(g/cc), reducing to 1,384.21 for the best-fit regression, which has a gradient of 0.5313 and an intercept of 4,484.69. The gradient of less than unity is the quantitative expression of a compressed dynamic range: the inversion recovers the central part of the impedance distribution well but pulls the extremes towards the mean. The scatter accordingly increases at impedances above approximately 12,000 (m/s)(g/cc), where fewer

samples are available and where the inversion underestimates the highest values, an expected consequence of the limited seismic bandwidth (Figure 4.21).

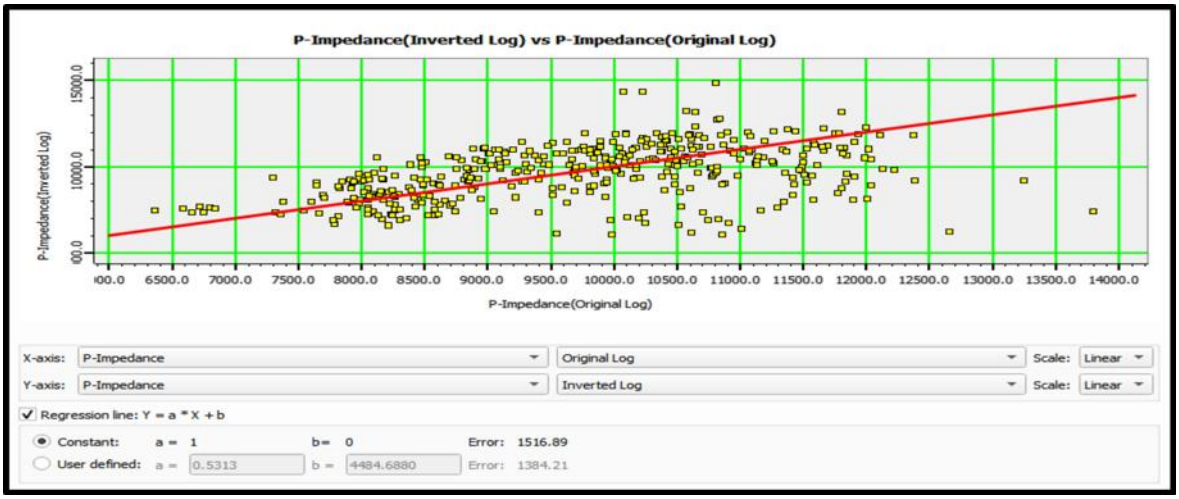



Figure 4. 46 Cross-plot of inverted P-impedance against original P-impedance at Kadanwari-03, with the 45-degree reference line and the best-fit regression.

The inverted section along TJ-89-512 is displayed in absolute acoustic impedance from CDP 246 to CDP 556 with Kadanwari-03 tied at CDP 440 and all interpreted horizons posted, on a colour scale running from 6,000 (m/s)(g/cc) in red through yellow and green to 11,927 (m/s)(g/cc) in magenta. The highlighted interval lies immediately below the Lower Goru Sand horizon, between approximately 2,240 and 2,420 ms, and carries the green to cyan response of approximately 9,400 to 10,500 (m/s)(g/cc). It is enclosed above and below by thin, laterally continuous magenta bands of approximately 11,600 to 11,900 (m/s)(g/cc), the configuration expected where a more porous interval is encased between tighter units, and both the zone and its bounding bands can be followed across the full length of the section rather than being restricted to the vicinity of the well.

Two further features of this section should be recorded. Below approximately 2,440 ms the section passes into a thick yellow to orange interval of approximately 7,300 to 8,400 (m/s)(g/cc), which is by some margin the lowest impedance on the display. This interval lies below the base of the logged section at Kadanwari-03, where the inversion analysis window closes at approximately 2,320 ms, so its absolute level is controlled by the low-frequency model rather than by well data and it should not be read as a reservoir response without independent confirmation. Above the highlighted zone, between approximately 1,500 and 2,100 ms, the section carries a broad green interval of approximately 9,400 to 9,900 (m/s)(g/cc) within the Lower Goru, which is the lowest impedance developed anywhere within the logged section on this line (Figure 4.22).

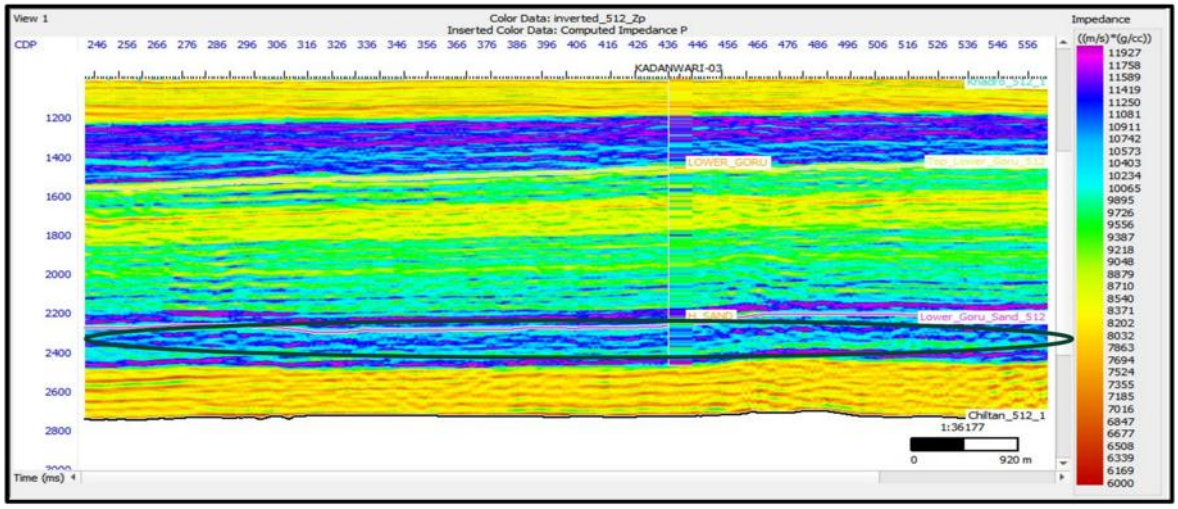



Figure 4. 47 Inverted P-impedance section along line TJ-89-512 with Kadanwari-03 tied at CDP 440. The highlighted interval, immediately below the Lower Goru Sand horizon, carries approximately 9,400 to 10,500 (m/s)(g/cc) between two thin high-impedance bands; the thick low-impedance interval below approximately 2,440 ms lies beneath the base of the logged section at the well.

The predicted volume of shale along TJ-89-512 is displayed on a scale from 0.4428 to 0.7323 v/v, with the lowest shale volumes in pale yellow and green and the highest in blue-grey and buff. The section is finely mottled throughout and is organised into laterally continuous laminae that follow the interpreted layering rather than cutting across it. Through the logged part of the Lower Goru, between the Top Lower Goru horizon and approximately 2,300 ms, shale volume alternates between approximately 0.45 and 0.59 with no single interval standing out as a clean sand. The highlighted interval, between approximately 2,400 and 2,560 ms, carries a laterally continuous buff band of approximately 0.62 to 0.73 v/v, that is a shale-rich rather than a sand-prone response, set against the more mottled and generally lower values above and below it. As with the impedance section, this interval lies below the logged section at the calibrating well and outside the range of impedance represented in the training data, so it is not constrained by the well control (Figure 4.23).

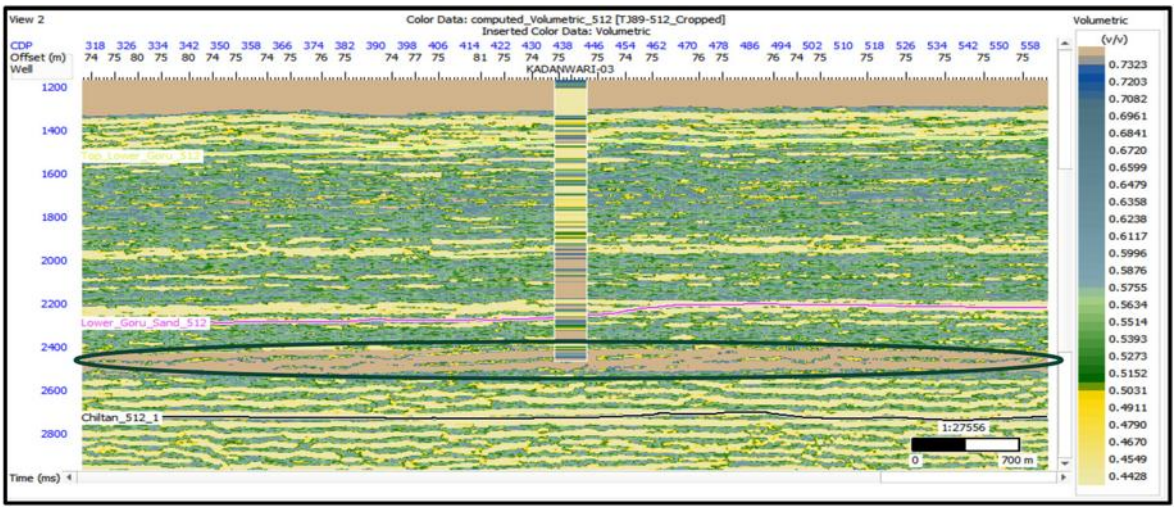



Figure 4. 48 Predicted volume of shale along line TJ-89-512, calibrated at Kadanwari-03, displayed on a scale from 0.4428 to 0.7323 v/v; the highlighted interval carries the shale-rich buff response.

The predicted porosity section along the same line is displayed from 0.0280 to 0.4000 v/v. The response is banded and follows the same layering. Low porosities of approximately 0.03 to 0.09, shown in green, occupy the interval from approximately 1,200 to 1,500 ms and again from approximately 1,900 to 2,400 ms, and these are separated by an interval of higher porosity of approximately 0.12 to 0.17, shown in yellow and orange, between approximately 1,550 and 1,900 ms. The highlighted interval, between approximately 2,400 and 2,570 ms, spans the downward transition out of that green low-porosity response and into the orange interval of approximately 0.13 to 0.17 that occupies the section from approximately 2,530 ms to the Chiltan horizon, with yellow values of approximately 0.09 to 0.12 across the transition itself. The elevated porosities therefore lie at and below the base of the logged section rather than within it (Figure 4.24).

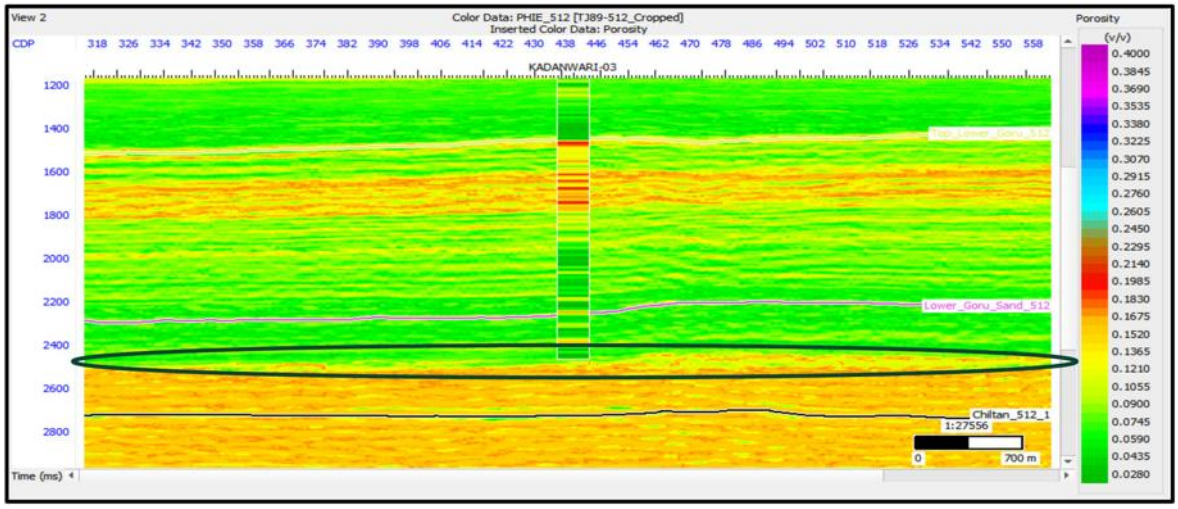



Figure 4. 49 Predicted porosity along line TJ-89-512, calibrated at Kadanwari-03, displayed on a scale from 0.0280 to 0.4000 v/v.

The predicted water saturation along TJ-89-512 is displayed from 0.5205 to 0.9056 v/v, with the highest saturations in dark blue and the lowest in yellow and red. Almost the whole section stands at or close to the upper limit of the scale, and only two intervals depart from it appreciably: a band between approximately 1,150 and 1,300 ms, and a narrow, strongly mottled band of yellow and red at approximately 2,400 to 2,480 ms, at the top of the highlighted interval, where saturation falls to approximately 0.58 to 0.70. That band is laterally continuous along the full length of the line and coincides in time with the base of the highlighted zone on the impedance section and with the porosity transition of Figure 4.24. Below it the section returns immediately to saturations close to 0.90 (Figure 4.25).

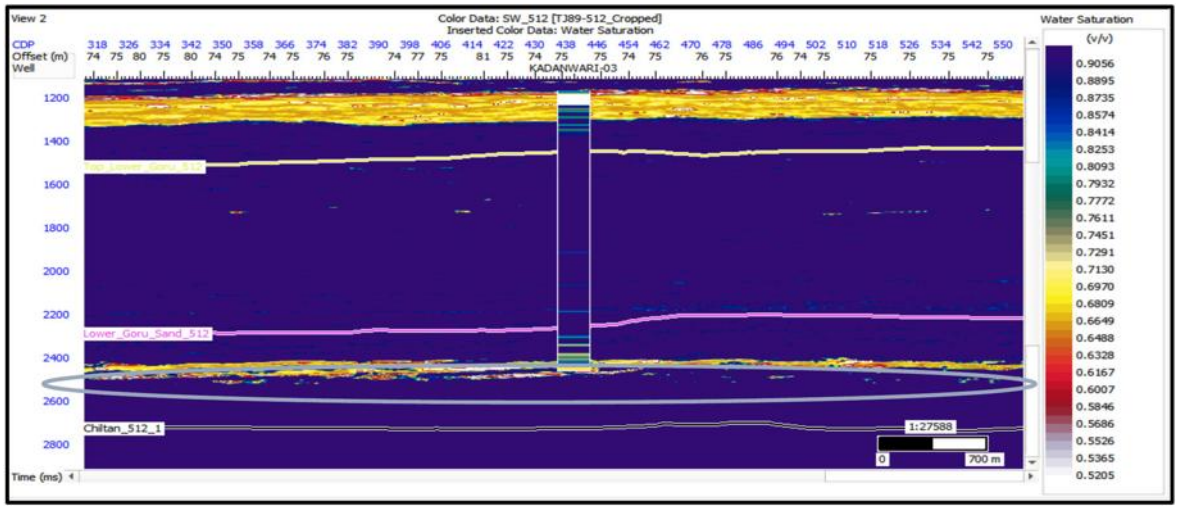



Figure 4. 50 Predicted water saturation along line TJ-89-512, calibrated at Kadanwari-03, displayed on a scale from 0.5205 to 0.9056 v/v; dark blue denotes the highest saturations.

The predicted permeability section along TJ-89-512 is displayed from 0.0 to 40.0 mD and is calculated over the interval from the Upper Goru to the Chiltan level. Through the logged section the background is green at permeabilities of the order of 0 to 5 mD, lightly speckled with orange and red values of 10 to 20 mD, and a more heavily mottled interval is developed between approximately 1,600 and 1,900 ms. The highlighted interval, between approximately 2,390 and 2,570 ms, spans the downward passage out of that green background into a densely mottled interval in which magenta values at and above 40 mD predominate and which continues to the base of the display. The permeability increase therefore coincides in time with the porosity increase of Figure 4.24 and with the base of the highlighted zone on the impedance section, and it lies below the logged interval at the calibrating well (Figure 4.26).

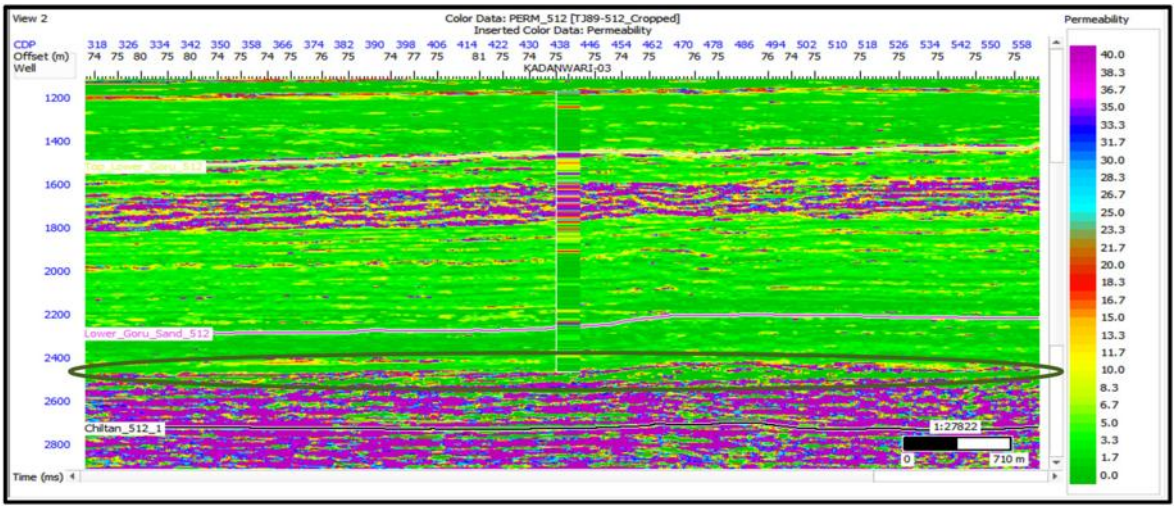



Figure 4. 51 Predicted permeability along line TJ-89-512, calibrated at Kadanwari-03, displayed on a scale from 0.0 to 40.0 mD.

Taken together, the four predicted sections along TJ-89-512 place the strongest property contrasts at approximately 2,400 to 2,570 ms, some 100 to 250 ms below the base of the inversion analysis window at this well. Within the logged part of the Lower Goru the predicted properties are comparatively featureless, and the clearest impedance contrast within that logged interval is the broad green low at approximately 1,500 to 2,100 ms noted above. The contrasts below the logged section are the least well constrained part of the prediction and are carried forward qualitatively only, for the reasons set out in the introduction to this section.

### 4.5.2 Kadanwari-04 (Line TJ-89-526)

Kadanwari-04 lies on line TJ-89-526 at approximately CDP 510, at coordinates 527,657.00 m east and 2,992,120.00 m north, with a kelly bushing elevation of 50.15 m and a seismic reference datum of 42.15 m. The well reaches the top of the Lower Goru Formation but does not penetrate the individual sand units, and the consequences of that limited log coverage run through the whole of this subsection.

The same statistical wavelet was applied to the inversion along TJ-89-526, extracted from the seismic data between the Khadro and Chiltan levels. It is zero phase and symmetrical about zero time, with a bandwidth of approximately 15 to 60 Hz and dominant energy near 31 Hz, and frequencies below approximately 10 Hz are absent as a result of the low-cut filter applied during processing. The fact that a single wavelet character is representative across the survey is itself a result: it indicates that the processing has delivered a laterally consistent embedded wavelet, so the three inversions are directly comparable with one another (Figure 4.27).

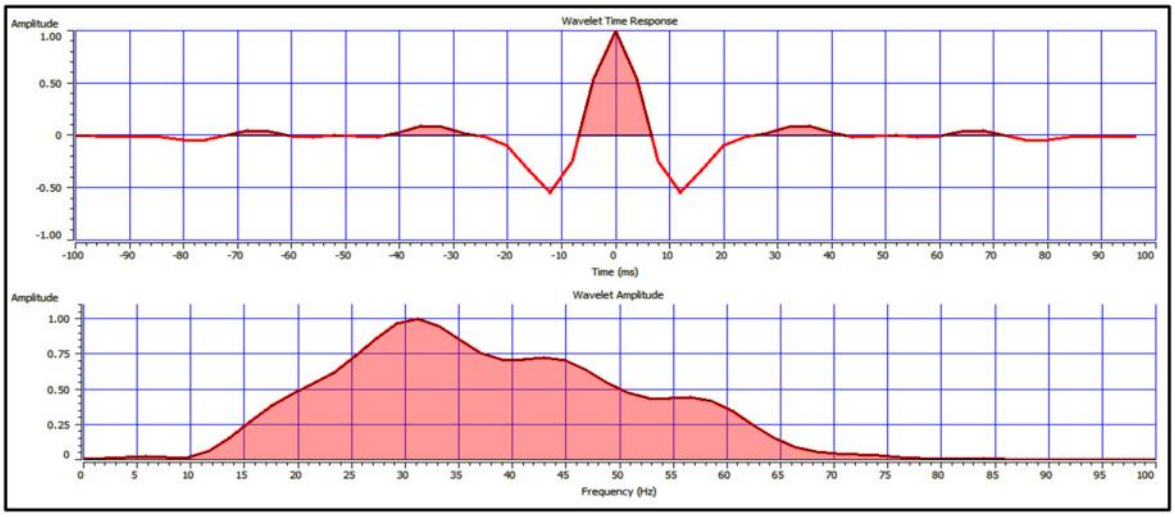



Figure 4. 52 Statistical wavelet applied to the inversion along line TJ-89-526 at Kadanwari-04, showing the time response (upper) and the amplitude spectrum (lower).

The seismic-to-well tie at Kadanwari-04 was constructed on the same basis, with the density log displayed from 1.5 to 3.0 g/cc, the corrected P-wave velocity from 1,000 to 6,000 m/s and the volume of shale from 0 to 1 v/v, and the synthetic seismogram shown against the seismic trace extracted from the cropped TJ-89-526 volume between CDP 251 and CDP 291. Only one formation top is available at this well, the Lower Goru top at approximately 1,490 ms, which is posted against the Top Lower Goru horizon on the seismic panel. The cross-correlation was computed over a window of 1,500 to 2,360 ms with a lag of ±50 ms and

returns a maximum coefficient of 0.594 at zero lag with a phase rotation of zero degrees. The tie is acceptable across the Upper Goru and Lower Goru levels, although the correlation is lower than at Kadanwari-03; this is attributed to the shorter logged section available at this well, which spans approximately 2,500 to 3,500 m true vertical depth, and to the absence of the individual Lower Goru sand tops, which reduces the number of independent events available for matching (Figure 4.28).

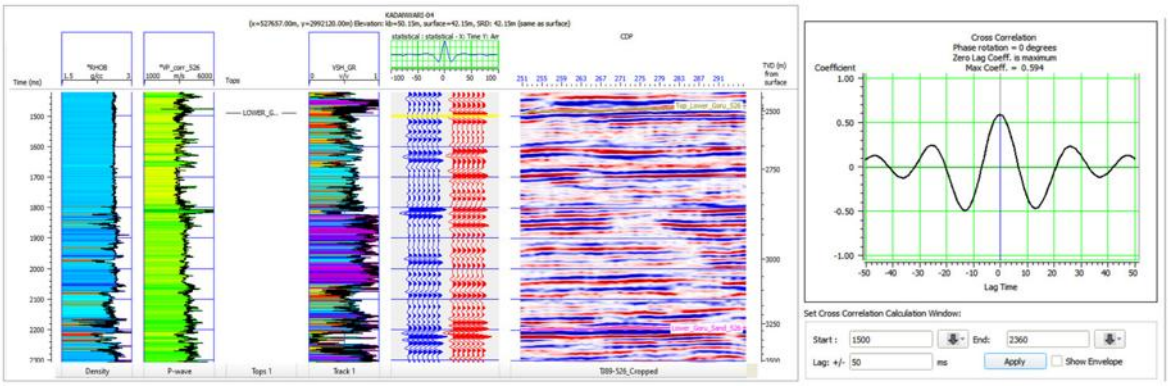



Figure 4. 53 Seismic-to-well tie for Kadanwari-04 on line TJ-89-526, showing the density, P-wave velocity and volume of shale tracks, the synthetic seismogram against the extracted seismic trace, and the cross-correlation function computed over the 1,500 to 2,360 ms window.

The initial low-frequency model along TJ-89-526 was constructed on the same basis as that at Kadanwari-03, using the interpreted horizons as layer boundaries and the upscaled impedance from Kadanwari-04, with a fifteen-sample moving average. The model is displayed from CDP 255 to CDP 565 at a horizontal scale of approximately 1:36,065, extends from the Khadro to the Chiltan level, and covers an impedance range of approximately 6,000 to 11,927 (m/s)(g/cc). The layering again follows the interpreted horizons, with the Top Lower Goru horizon at approximately 1,450 ms and the Lower Goru Sand horizon at approximately 2,200 ms (Figure 4.29).

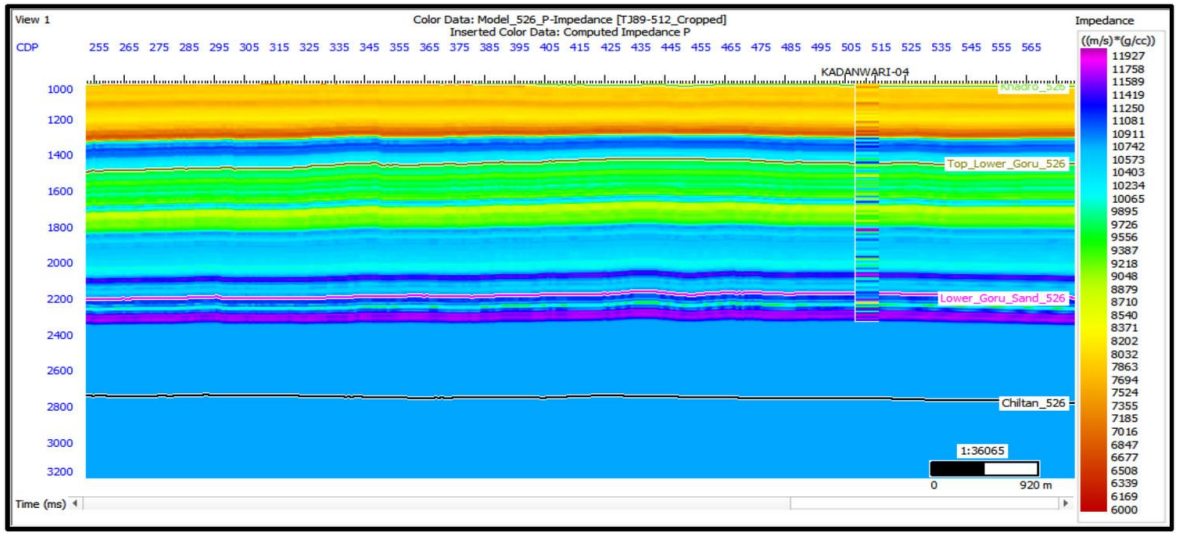



Figure 4. 54 Initial low-frequency impedance model along line TJ-89-526, built from the interpreted horizons and the upscaled impedance log at Kadanwari-04.

The inversion analysis at Kadanwari-04 compares the inverted impedance with the original and upscaled logs over an impedance range of 3,800.27 to 15,520.2 (m/s)(g/cc), with the associated synthetic and recorded traces taken at CDP 251 of the cropped volume. The correlation between the synthetic and the recorded trace is 0.9963 and the residual error is 0.086, with an impedance error of 1,135.98 (m/s)(g/cc) on the log track. The inverted impedance follows the upscaled log through the Lower Goru interval over the analysis window from approximately 1,480 to 2,250 ms, and the agreement is comparable with that obtained at Kadanwari-03 despite the lower well-tie correlation reported above. The residual trace again shows no systematic structure (Figure 4.30).

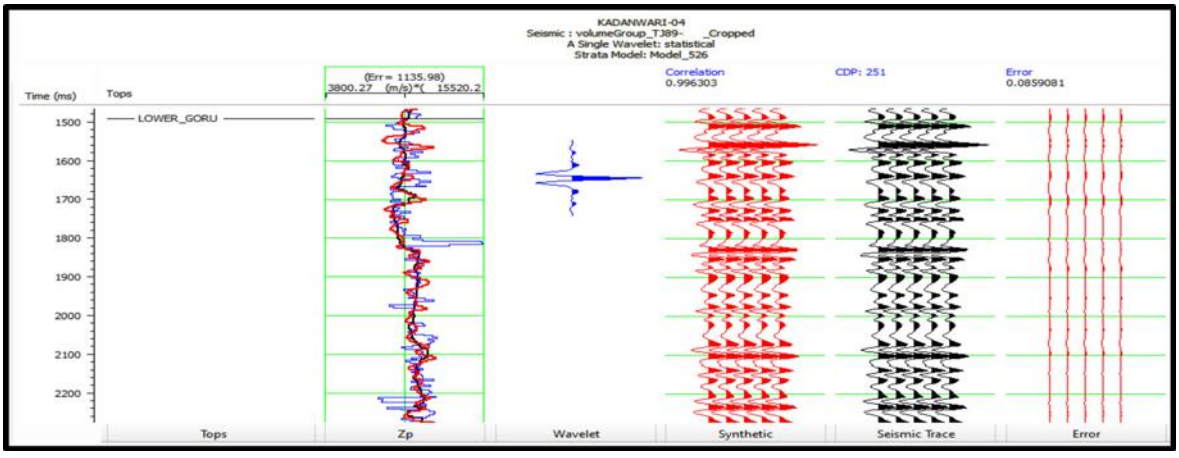



Figure 4. 55 Comparison of the inverted, upscaled and original impedance logs at Kadanwari-04, with the synthetic, the recorded seismic trace and the residual error.

The cross-plot of inverted against original impedance at Kadanwari-04 shows the points clustered about the 45-degree reference line over an impedance range of approximately 5,500 to 16,000 (m/s)(g/cc). The error about that line is 1,135.98 (m/s)(g/cc), reducing to 994.06 for the best-fit regression, which has a gradient of 0.6353 and an intercept of 3,424.74. Both error terms are the lowest of the three wells and the regression gradient is the steepest, which indicates that the inversion reproduces the measured impedance more closely at this well than at either of the others and compresses the dynamic range least (Figure 4.31).

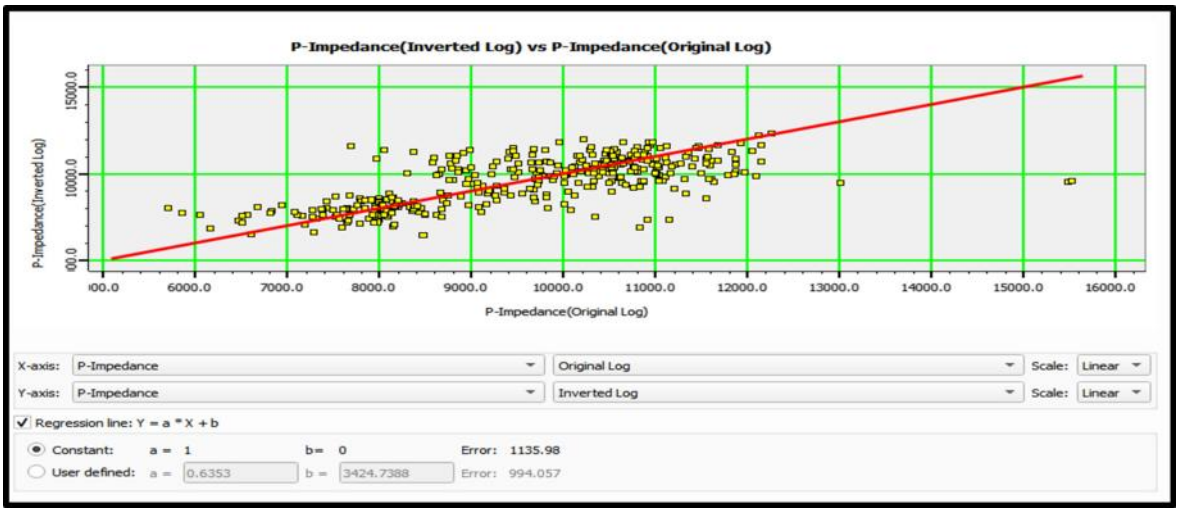



Figure 4. 56 Cross-plot of inverted P-impedance against original P-impedance at Kadanwari-04, with the 45-degree reference line and the best-fit regression.

The inverted section along TJ-89-526 is displayed from CDP 255 to CDP 565 with Kadanwari-04 tied at CDP 510, on the same colour scale of 6,000 to 11,927 (m/s)(g/cc) used for the other two lines. Above the Top Lower Goru horizon at approximately 1,400 ms the section carries the low impedance values of approximately 7,200 to 8,400 (m/s)(g/cc) shown in orange and yellow. Between the Top Lower Goru horizon and approximately 1,900 ms a broad green interval of approximately 9,400 to 9,900 (m/s)(g/cc) is developed, and this is the lowest impedance reached anywhere within the Lower Goru on this line. Below approximately 1,900 ms the section is dominated by the higher values of approximately 10,100 to 10,600 (m/s)(g/cc) shown in cyan.

The highlighted interval lies immediately below the Lower Goru Sand horizon, between approximately 2,200 and 2,350 ms. It carries the cyan response of approximately 10,100 to 10,600 (m/s)(g/cc) together with a laterally continuous magenta band of approximately 11,600 to 11,900 (m/s)(g/cc) developed between approximately 2,250 and 2,330 ms, so the interval marked at reservoir level on this line is one of elevated rather than

reduced impedance. The green low-impedance interval higher in the Lower Goru, between the Top Lower Goru horizon and approximately 1,900 ms, is the counterpart on this line of the green interval identified over the same relative position on TJ-89-512, and it is laterally continuous across the full length of the section (Figure 4.32).

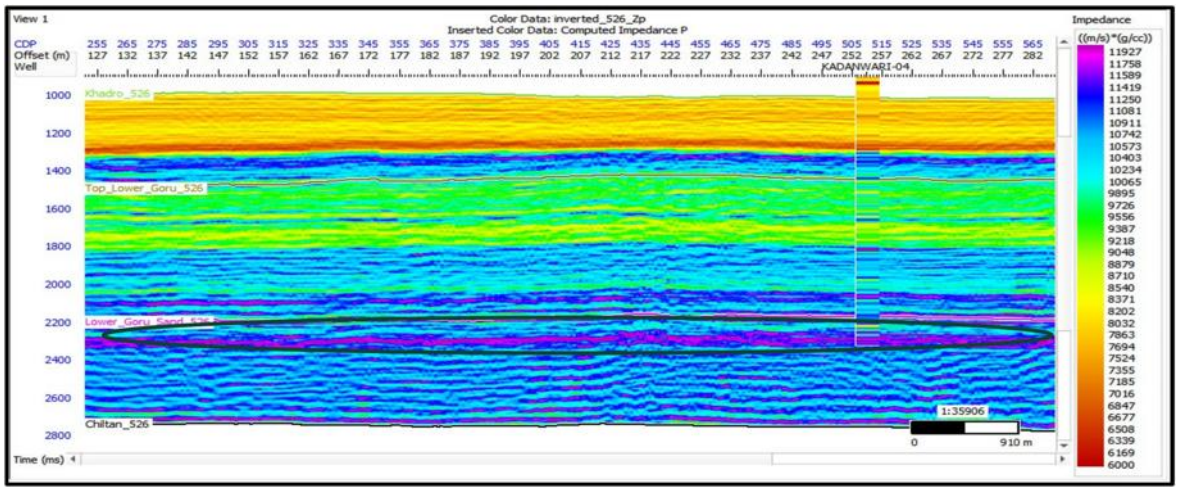



Figure 4. 57 Inverted P-impedance section along line TJ-89-526 with Kadanwari-04 tied at CDP 510. The highlighted interval, immediately below the Lower Goru Sand horizon, carries approximately 10,100 to 10,600 (m/s)(g/cc) with a laterally continuous high-impedance band developed within it; the green low-impedance interval higher in the Lower Goru lies between approximately 1,450 and 1,900 ms.

The predicted volume of shale along TJ-89-526 is displayed on a scale from 0.4428 to 0.7323 v/v. The section is dominated by the blue-grey response of relatively high shale volume at approximately 0.58 to 0.67, speckled throughout with pale yellow values of approximately 0.44 to 0.49 and organised into fine laterally continuous laminae. The highlighted interval between approximately 2,220 and 2,410 ms is indistinguishable in character from the intervals immediately above and below it: the mottling continues across the Lower Goru Sand horizon without any change in the density or the amplitude of the yellow response, and no interval of reduced shale volume is resolved at reservoir level (Figure 4.33).

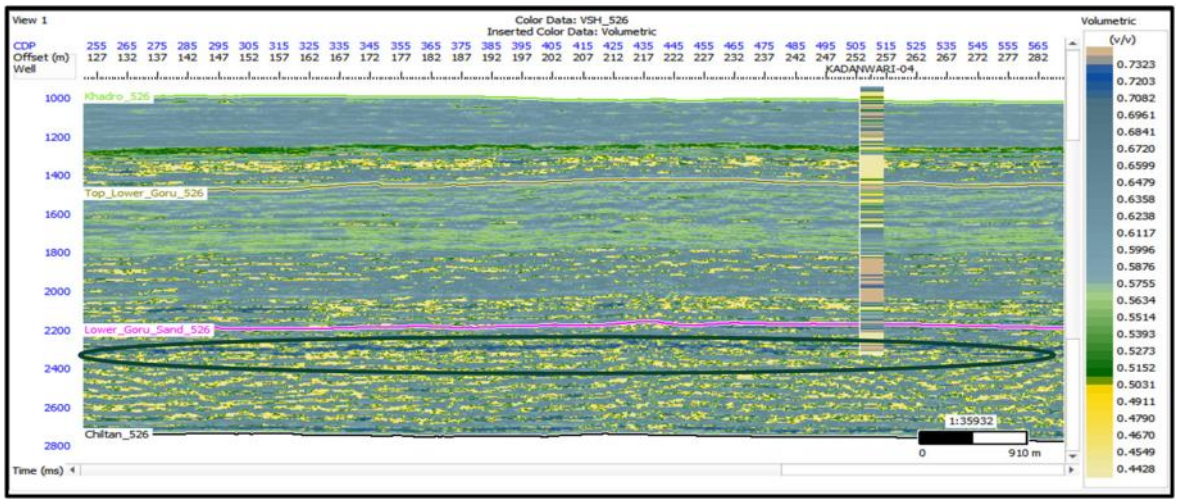



Figure 4. 58 Predicted volume of shale along line TJ-89-526, calibrated at Kadanwari-04, displayed on a scale from 0.4428 to 0.7323 v/v.

The predicted porosity section along TJ-89-526 is displayed from 0.0280 to 0.4000 v/v. Values of approximately 0.09 to 0.13 are predicted above the Top Lower Goru horizon, interrupted by a laterally continuous band of approximately 0.18 to 0.20 shown in red at approximately 1,300 ms, which lies above the logged section and is not constrained by the training data. Between approximately 1,400 and 2,200 ms the section carries values of approximately 0.07 to 0.11 in yellow-green, and below the Lower Goru Sand horizon, across the highlighted interval between approximately 2,250 and 2,420 ms, it becomes uniformly green at approximately 0.05 to 0.09, broken only by faint yellow laminae, and shows no increase at the level of the B sand (Figure 4.34).

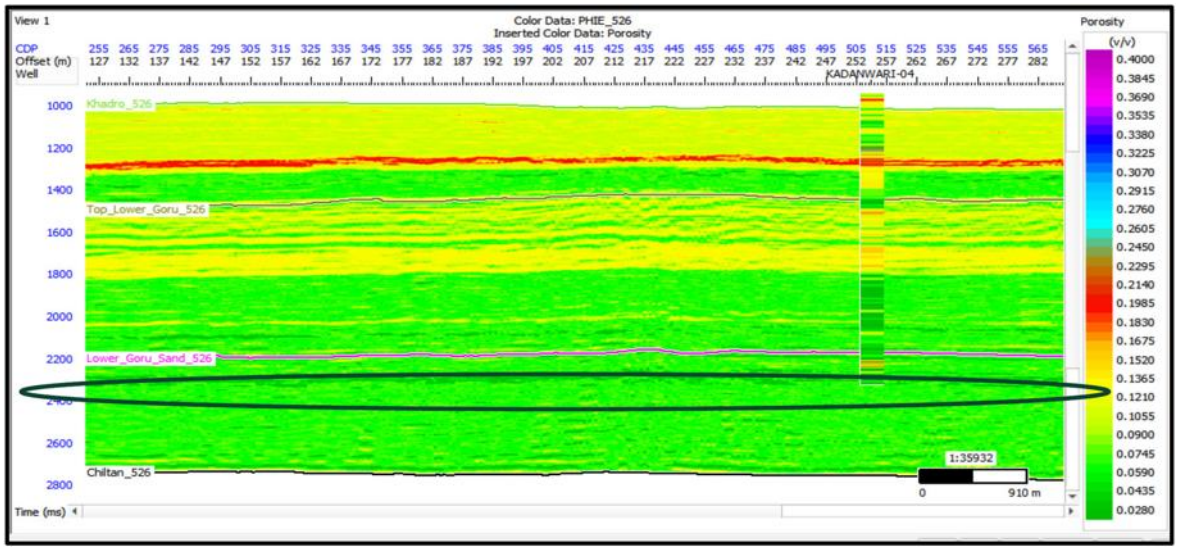



Figure 4. 59 Predicted porosity along line TJ-89-526, calibrated at Kadanwari-04, displayed on a scale from 0.0280 to 0.4000 v/v.

The predicted water saturation along TJ-89-526 is displayed from 0.5205 to 0.9056 v/v. Saturations of approximately 0.89 to 0.91 are predicted above approximately 1,250 ms, and below approximately 1,400 ms the section stabilises at approximately 0.78 to 0.80 in teal and remains effectively constant to the base of the display. No interval of reduced saturation is developed at reservoir level (Figure 4.35).

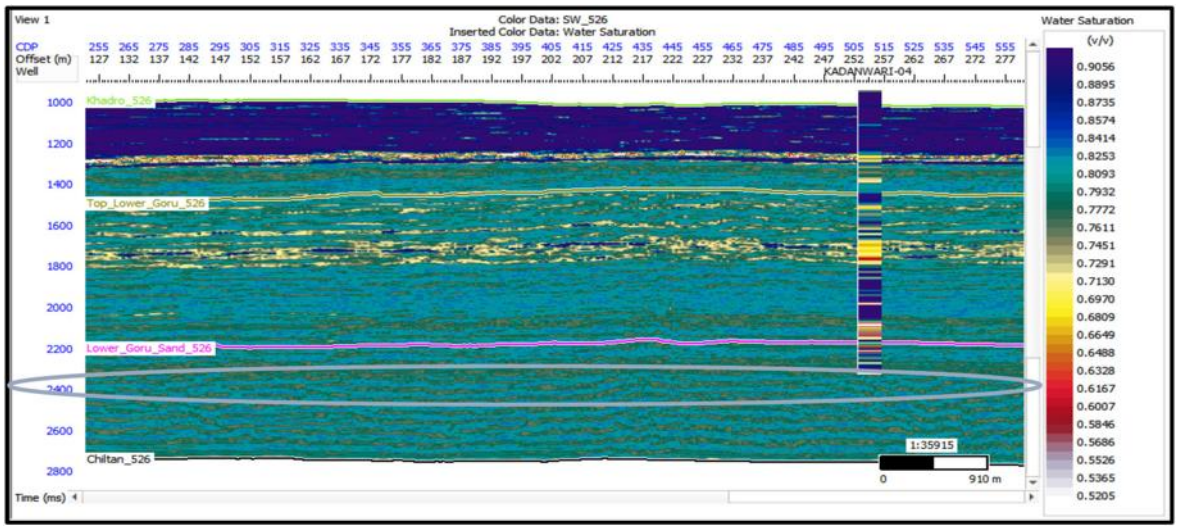



Figure 4. 60 Predicted water saturation along line TJ-89-526, calibrated at Kadanwari-04, displayed on a scale from 0.5205 to 0.9056 v/v; dark blue denotes the highest saturations.

The predicted permeability section along TJ-89-526 is displayed from 0.0 to 40.0 mD and is calculated over the interval from the Upper Goru to the Chiltan level. Above approximately 1,300 ms the section carries values of approximately 25 to 33 mD in cyan and blue; this interval lies above the logged section and the values are outside the calibrated range. Between approximately 1,450 and 1,900 ms the section is green at 0 to 5 mD with laterally continuous orange and red bands of approximately 15 to 20 mD, and below the Lower Goru Sand horizon, across the highlighted interval between approximately 2,250 and 2,440 ms, it becomes uniformly green at 0 to 3 mD with only isolated yellow specks (Figure 4.36).

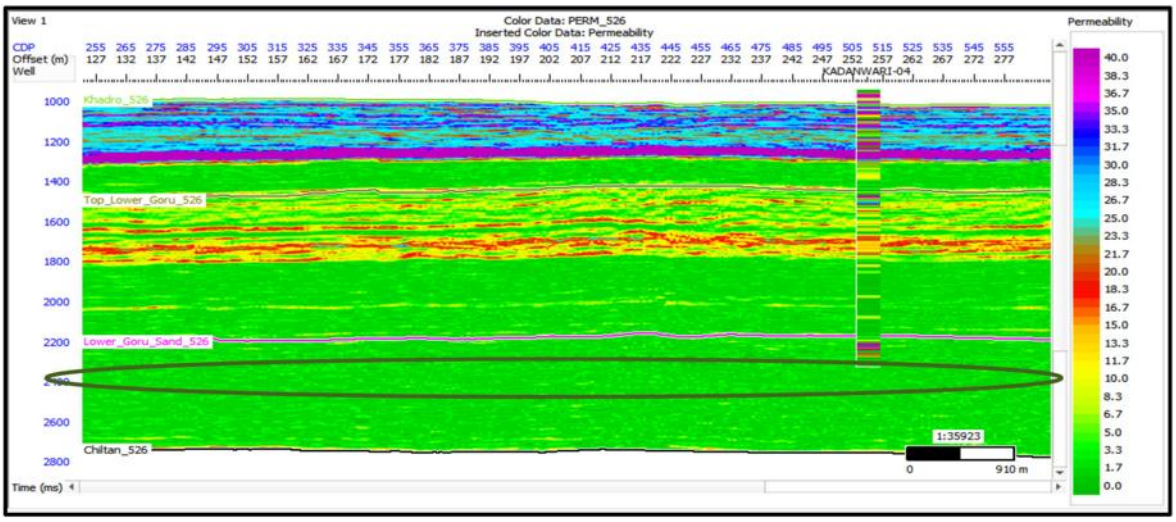



Figure 4. 61 Predicted permeability along line TJ-89-526, calibrated at Kadanwari-04, displayed on a scale from 0.0 to 40.0 mD.

The four predicted sections along TJ-89-526 are therefore effectively featureless below approximately 2,200 ms, and this is a consequence of the log control rather than a statement about the reservoir. As recorded in Section 3.2, Kadanwari-04 reaches the top of the Lower Goru Formation without penetrating the individual sand units, so the training set for this line contains no samples of the reservoir interval. A model that has never seen the rock cannot predict its properties, and the flat response below the logged section is the expected consequence, not evidence that the reservoir is absent. The inverted impedance section of Figure 4.32, which does not depend on the training data, carries the low-impedance zone at reservoir level on this line and is the result that should be carried forward from it.

### 4.5.4 Summary of the Inversion Results

The quality-control figures obtained at the three wells are collected in Table 4.2. All three ties are correctly phased, with the cross-correlation maximum at zero lag and a phase rotation of zero degrees in every case, and all three inversions reproduce the recorded seismic to a correlation of better than 0.996 with residual errors below 0.09. The three wells are separated, however, by the cross-plot errors. Kadanwari-04 returns the lowest error and the steepest regression gradient, Kadanwari-03 is intermediate, and Kadanwari-01 returns an error about the reference line more than twice that at Kadanwari-04 together with the shallowest gradient of the three.

| | **Kadanwari-03** | **Kadanwari-04** | **Kadanwari-01** |
|---|---|---|---|
| **Seismic line** | TJ-89-512 | TJ-89-526 | TJ-89-516 |
| **Well position (CDP)** | 440 | 510 | 761 |

| | Kadanwari-03 | Kadanwari-04 | Kadanwari-01 |
|---|---|---|---|
| **Tie window (ms)** | 1,100 – 2,400 | 1,500 – 2,360 | 1,270 – 2,500 |
| **Maximum cross-correlation** | 0.691 | 0.594 | 0.585 |
| **Phase rotation** | 0° | 0° | 0° |
| **Analysis CDP** | 440 | 251 | 315 |
| **Synthetic–seismic correlation** | 0.9969 | 0.9963 | 0.9965 |
| **Residual error** | 0.079 | 0.086 | 0.083 |
| **Cross-plot error, 45° line** | 1,516.89 | 1,135.98 | 2,375.59 |
| **Cross-plot error, best fit** | 1,384.21 | 994.06 | 1,150.06 |
| **Best-fit gradient** | 0.5313 | 0.6353 | 0.3483 |
| **Highlighted zone** | 9,400 – 10,500 | 10,100 – 11,900 | 7,300 – 8,200 |
| **Zone interval (ms)** | 2,240 – 2,420 | 2,200 – 2,350 | 2,400 – 2,600 |
| **Lowest Zp in logged Lower Goru** | 9,400 – 9,900 (1,500 – 2,100 ms) | 9,400 – 9,900 (1,450 – 1,900 ms) | 7,300 – 8,200 (2,400 – 2,600 ms) |

Table 4. 2 Quality-control summary of the model-based inversion at the three wells, giving the seismic-to-well tie parameters, the correlation between the synthetic generated from the inverted result and the recorded trace, the cross-plot errors against the 45-degree reference line and the best-fit regression, the impedance and time interval of the zone highlighted on each inverted section, and the lowest impedance reached within the logged part of the Lower Goru on each line. Impedance and error values are in (m/s)(g/cc).

The inverted sections agree on one point and differ on another. On all three lines a laterally continuous zone of reduced acoustic impedance is developed within the Lower Goru interval and can be followed across the full length of the section, so the low-impedance response is a field-scale feature developed between the wells and not only at them. Where the lines differ is in the position of that zone relative to the mapped Lower Goru Sand horizon. On TJ-89-516 it lies beneath the horizon, between approximately 2,400 and 2,600 ms, at the level at which Kadanwari-01 penetrates the B sand, and it reaches 7,300 to 8,200 (m/s)(g/cc). On TJ-89-512 and TJ-89-526 the lowest impedance within the logged Lower Goru lies well above the horizon, between approximately 1,450 and 2,100 ms, at 9,400 to 9,900 (m/s)(g/cc), while the interval immediately beneath the horizon carries 10,100 to 10,600 (m/s)(g/cc) on both lines, with a laterally continuous high-impedance band developed within it on TJ-89-526.

Two considerations bear on that difference. The first is log control: Kadanwari-01 is the only well that penetrates the B sand, and it is the only line on which the low-impedance zone at the horizon can be tied to a logged reservoir. At Kadanwari-03 the inversion analysis window closes at approximately 2,320 ms and at Kadanwari-04 at approximately 2,250 ms,

so on those two lines the interval at and below the Lower Goru Sand horizon is at or beyond the limit of the well control. The second is the compression of dynamic range quantified by the cross-plots: the best-fit gradient at Kadanwari-01 is 0.3483 against 0.5313 and 0.6353 at the other two wells, and the intercept is correspondingly larger, so absolute impedance values are not directly comparable between TJ-89-516 and the other two lines. The difference between the sections is therefore not by itself evidence that the reservoir is absent along TJ-89-512 and TJ-89-526.

The property predictions likewise do not give a uniform result, and the differences between the lines follow from the log control at the calibrating wells rather than from the seismic. Line TJ-89-516, tied to the only well that penetrates the B sand, returns a coherent reservoir response between approximately 2,400 and 2,600 ms, with porosity of approximately 0.24 to 0.28, shale volume of approximately 0.45 to 0.52, water saturation of approximately 0.60 to 0.65 and permeability of 10 to 35 mD, all four coincident with one another and with the low-impedance zone identified independently from the inversion. This is the only line on which the four predicted properties combine into the configuration expected of a reservoir sand. Line TJ-89-526 returns no resolvable response at reservoir level at all, for the reason set out at the end of Section 4.4.2. Line TJ-89-512 returns its strongest property contrasts at approximately 2,400 to 2,570 ms, below the base of the analysis window at Kadanwari-03, and those contrasts are not internally consistent: shale volume rises to approximately 0.62 to 0.73 over the same interval in which porosity and permeability increase. Since all four properties are transforms of the same impedance, that inconsistency lies in the transforms rather than in the data, and it indicates that the relationship learned at Kadanwari-03 does not carry the same sense as the relationship learned at Kadanwari-01. The predicted sections along TJ-89-512 are therefore used qualitatively in what follows, and the porosity carried into the volumetric estimate is taken from the line and the well that constrain the B sand directly.

Three limitations should be carried forward from this section into the storage estimate of Section 4.6. The absolute impedance values are least reliable along TJ-89-516, where the cross-plot error is the largest of the three wells, so that section is better used for its lateral variation than for its absolute values. The predicted properties on any line are transforms of a single impedance attribute and are not independent of one another, so their coincidence over an interval cannot be treated as mutual confirmation. And the predictions are reliable only within the impedance range represented in the training data, which restricts them to the logged intervals and excludes the shallow part of all three sets of sections. The principal

result of this section stands within those limits: a laterally continuous low-impedance zone is developed within the Lower Goru interval on all three well-tied lines, and where the well control is sufficient to constrain it, along TJ-89-516 at Kadanwari-01, that zone lies at the mapped Lower Goru B sand level and carries the porosity, shale-volume, saturation and permeability response of a reservoir sand.

## 4.6 Fault Seal Analysis

The juxtaposition analysis of Section 3.7 was carried out on F3, the major fault bounding the reservoir compartment on the B sand maps of Figures 4.17 and 4.18. Contour values were read on the upthrown and the downthrown side at nine positions along the fault trace, and the cut-off depths for the D sand, the C sand and the top and base of the B sand plotted against position to give the fault-plane section of Figure 4.45. Solid lines carry the upthrown block and broken lines the downthrown block; on either side the interval between the reservoir top and the reservoir base is the B sand, its base taken as the top of the underlying shale.

The section spans approximately 3,300 to 3,520 m. The D sand lies at the top of the diagram, its two profiles crossing near positions 4 and 7, so the sense of the offset at that level is not constant along strike. The C sand occupies the middle, and the shaded body extending from its upthrown top down to the top of the B sand is the downthrown C sand block, a thick non-reservoir section standing against the reservoir over the whole length of the fault. The B sand lies between about 3,460 and 3,520 m and is the narrowest of the three intervals, its top and base running close together over much of the section.

Over most of the length of F3 the throw at reservoir level is small relative to the thickness of the sand, so the upthrown and downthrown B sand intervals overlap and sand is placed against sand, which provides no juxtaposition seal in itself and leaves the two blocks potentially in communication. Two intervals depart from this and are annotated as possible sealing areas: the larger between positions 4 and 6, where the upthrown reservoir top falls away while the downthrown top rises and the reservoir of one block is carried against the fine-grained section of the other, and a narrower window between positions 8 and 9. F3 therefore offers localised rather than continuous juxtaposition sealing at reservoir level, and the more important element for vertical containment is the downthrown C sand block above it.

The two limits set out in Section 3.7 apply here as well. Juxtaposition establishes which units are placed against which and no more: entrained fine-grained material may still

support a pressure difference across a sand-against-sand window, and that fault rock is not quantified here. The cut-off depths are also only as accurate as the depth conversion. F3 is accordingly interpreted as showing potential sealing behaviour at the preliminary assessment level, which is the basis on which the fault-bounded closures are treated as separate storage compartments in Section 4.7.

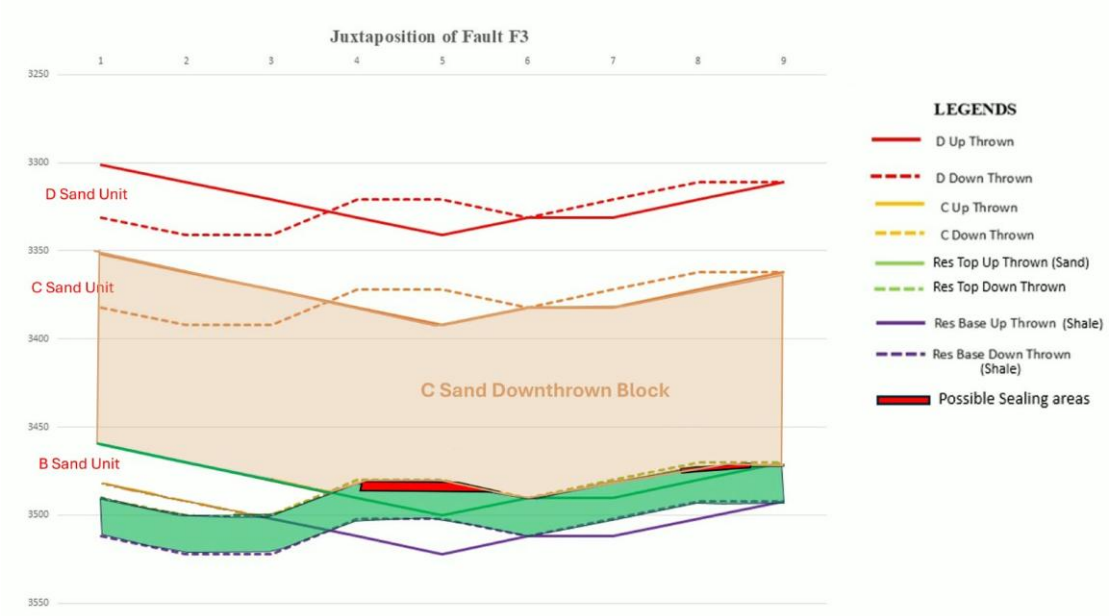



Figure 4. 62 Juxtaposition diagram for fault F3, constructed from the upthrown and downthrown cut-off depths of the D sand, the C sand and the Lower Goru B sand read at nine positions along the fault trace. Solid lines denote the upthrown block and broken lines the downthrown block; the reservoir base is taken as the top of the underlying shale. The intervals shown in red are the possible sealing areas identified from the juxtaposition.

## 4.7 Storage Capacity Estimation

The volumetric method set out in Section 3.8 was applied to three structural closures delineated on the mapped Lower Goru B sand surface of Section 4.3.3. Each closure was outlined as a polygon around the closing contours and its area measured in map view, and the area was then combined with the effective reservoir thickness, the effective porosity and water saturation of Sections 4.2 and 4.5, the adopted CO2 density of 600 kg/m³ and the storage efficiency factor to give the mass of CO2 that the pore volume of the closure could hold. All three lie in the north-central part of the survey, on the narrow fault-bounded culmination immediately north-west of Kadanwari-03 identified on the B sand maps of Figures 4.17 and 4.18, and each falls within a single fault-bounded compartment. The polygons are shown as white outlines on the maps of Figures 4.46 to 4.48.

### 4.7.1 Three closure areas marked

Closure 1 is outlined immediately north-west of Kadanwari-03 as a narrow, wedge-shaped polygon elongated north-northwest to south-southeast in parallel with the mapped fault trend, tapering to a point at its northern end and closing on the well at its southern end. It occupies the western side of the fault-bounded culmination, where the contours turn and close against the fault. Its narrowness is the feature that controls its capacity: the closing contours are tightly spaced across the block, so the area enclosed is small in comparison with the length of the closure (Figure 4.46).

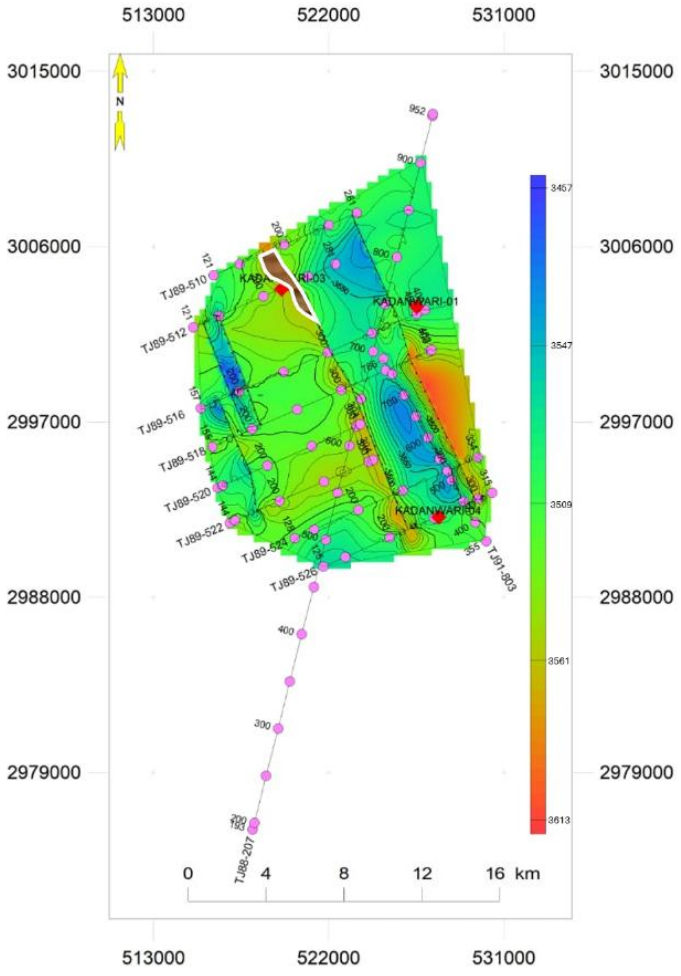



Figure 4. 63 Delineation of Closure 1 on the gridded Lower Goru B sand structure map used for the volumetric $CO_2$ storage-capacity estimation, with the three well locations posted.

Closure 2 occupies the same trend and is by some margin the smallest of the three. The polygon is a thin lens, narrower throughout than Closure 1, running from a point at its northern end down to Kadanwari-03. It is developed where the contours close over only a

short section of the block, and the area it encloses is a small fraction of that of either of the other two closures (Figure 4.47).

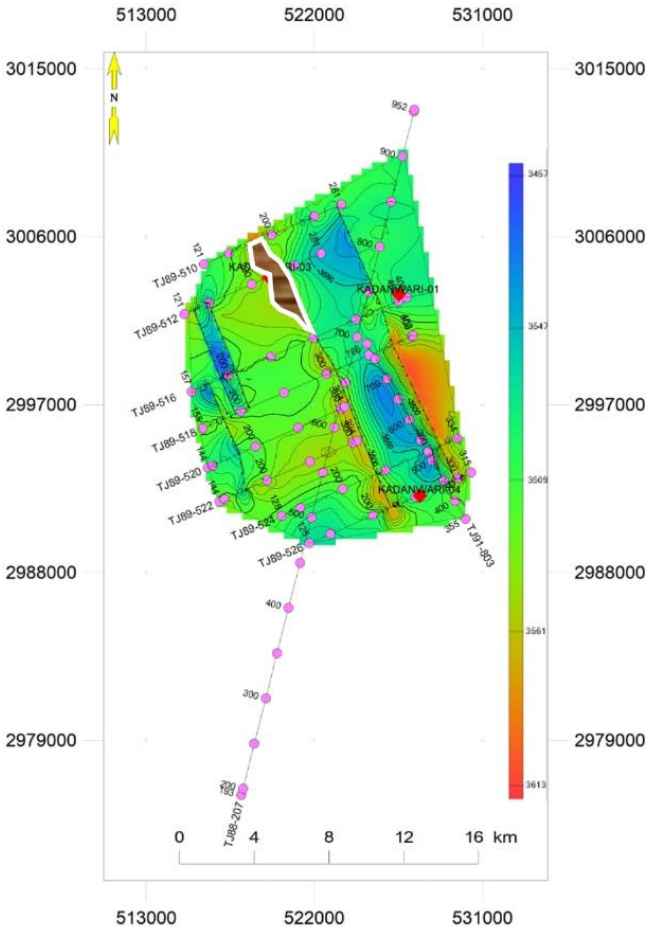



Figure 4. 64 Delineation of Closure 2 on the gridded Lower Goru B sand structure map used for the volumetric $CO_2$ storage-capacity estimation, with the three well locations posted.

Closure 3 is the largest of the three. The polygon shares the northern apex of Closure 1 but is both wider and appreciably longer, broadening through its central part and continuing south-southeast past Kadanwari-03 before narrowing to a point at its southern end. It encloses the more fully developed part of the same culmination, and it is this greater map area that dominates its calculated capacity (Figure 4.48).

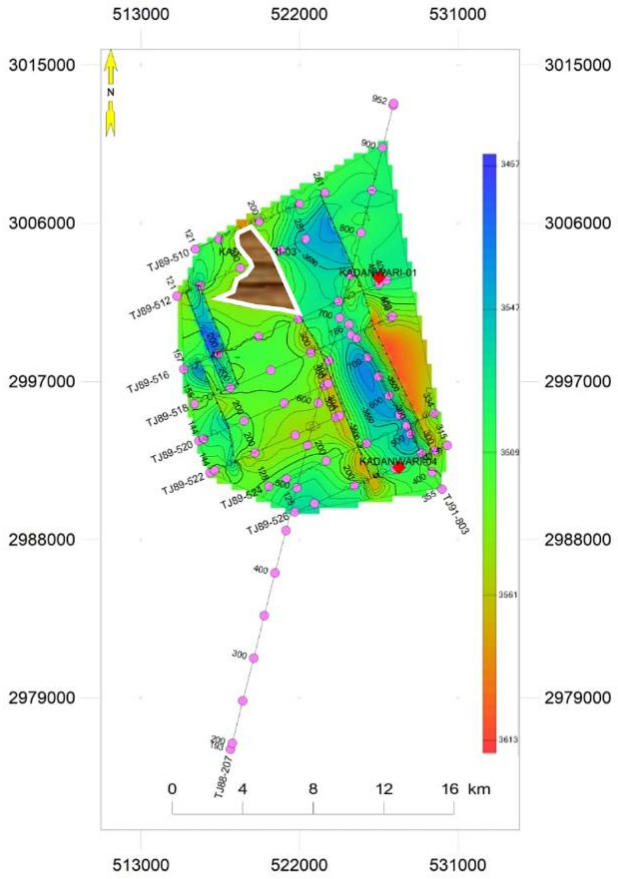



Figure 4. 65 Delineation of Closure 3 on the gridded Lower Goru B sand structure map used for the volumetric $CO_2$ storage-capacity estimation, with the three well locations posted.

The capacities calculated for the three closures are listed in Table 4.2.

| **Structural closure** | **Estimated $CO_2$ storage capacity (tonnes)** |
|---|---|
| Closure 1 (P90) | 81,968 |
| Closure 2 (P50) | 167,808 |
| Closure 3 (P10) | 326,823 |
| Combined | 576,599 |

Table 4. 3 Estimated volumetric $CO_2$ storage capacity of the three structural closures delineated on the Lower Goru B sand, calculated using an adopted $CO_2$ density of 600 kg/m³.

The three closures do not carry equal storage potential. Closure 3 accounts for approximately 326,823 tonnes, a little over seventy per cent of the total, and Closure 1 for approximately 81,968 tonnes. Closure 2, at approximately 167,808 tonnes, is smaller than

either of the others by more than an order of magnitude. The combined capacity of the three is approximately 576,599 tonnes, or about 0.5765 Mt of CO2.

The ranking follows the mapped areas of the polygons, not any difference in reservoir quality between the closures. Effective porosity and water saturation vary little from one to another, since all three lie within the same reservoir interval and are constrained by the same well control, so the area term carries most of the variation in the result. Closure 3 encloses the largest area and returns the largest capacity, Closure 2 encloses the smallest and returns the smallest, and effective thickness modulates the outcome without reversing it. The one qualification to this is that the porosity carried into the calculation is the predicted effective porosity of Section 4.5, which is best constrained along TJ-89-516 at Kadanwari-01, the only well penetrating the B sand; the closures lie closer to Kadanwari-03, where the predicted sections were shown in Section 4.5.4 to be less reliable, so the porosity assigned to them is the less well constrained of the two terms.

These figures come with three limits. They are static volumetric estimates of the pore space contained within the mapped closures, not injectable volumes: what could in practice be injected and retained would depend on injectivity, on the pressure development during injection, on well placement, on the geomechanical response of the reservoir and its bounding faults, and on the migration of the plume over time, none of which is assessed here. They rest on an adopted CO2 density and an assumed storage efficiency factor, and the efficiency factor in particular is not a measured quantity, so the figures are better read as indicating relative magnitude than as precise tonnages. And they apply to the three delineated closures alone; the combined figure of approximately 0.1185 Mt is the estimated capacity of those three compartments, not of the Kadanwari Gas Field as a whole.

Read together with the fault-seal result of Section 4.6, the volumetric outcome supports treating the three closures as preliminary $CO_2$ storage targets, with Closure 3 the most favourable of them on capacity alone. The juxtaposition analysis indicates potential sealing behaviour along F3 but does not establish it, and it shows the reservoir sands to be in contact across parts of the fault, so the capacities reported here are best regarded as the resource the closures contain rather than the volume they have been shown capable of retaining.

# CHAPTER 5
# DISCUSSION

The Kadanwari gas field provides a suitable geological setting for assessing the potential of depleted gas reservoirs for $CO_2$ storage. The field is associated with the Lower Goru Formation, which contains alternating sandstone and shale intervals. The sandstone provides potential reservoir space, while the surrounding fine-grained formations can contribute to containment. The use of depleted gas fields for $CO_2$ storage is particularly attractive because the reservoir has already contained hydrocarbons over geological time and its existing geological framework can be used for evaluating storage potential (Holloway et al., 2009).

Previous work has already identified Kadanwari as a potential site for $CO_2$ storage. Shah et al. (2024) assessed the storage potential of the field and identified suitable reservoir intervals and structural closures. The present study builds on this work by using seismic inversion and property prediction to investigate the B sand in greater detail. The study also considers the relationship between the B sand and the F3 fault and uses the interpreted closures to estimate their potential $CO_2$ storage capacity. In this way, the present study provides a more detailed view of the reservoir and its possible containment compared with the earlier assessment.

The seismic inversion results show a laterally continuous zone of reduced acoustic impedance at the B sand level across all three well-tied seismic lines. The consistency of this response is important because it suggests that the B sand extends across a considerable part of the investigated area rather than being restricted to the immediate vicinity of Kadanwari-01. The agreement between the three seismic lines also supports the interpretation of the low-impedance zone as a geological reservoir response. This is consistent with the geological character of the Lower Goru Formation, where contrasts between sandstone and shale can produce a clear acoustic impedance response.

The inversion therefore provides useful information about the lateral distribution of the B sand, particularly because Kadanwari-01 is the main well providing direct control on this interval. While the well gives detailed information at a single location, the seismic data allow the reservoir response to be followed between the available well locations. The continuous seismic response consequently provides a broader picture of the reservoir and helps define the areas that may contribute to $CO_2$ storage.

The predicted reservoir properties further support the interpretation of the B sand as a potential storage interval. Around Kadanwari-01, the predicted effective porosity is approximately 0.13, with a shale volume of approximately 0.40 and water saturation of approximately 0.53. These values indicate that the reservoir contains sufficient pore space to consider it for $CO_2$ storage, while the shale content reflects the interbedded nature of the reservoir. The combination of seismic inversion and property prediction is useful because inversion provides information about the distribution of the reservoir, while the predicted properties give an indication of its quality.

The results also highlight the importance of integrating seismic interpretation with the structural framework of the field. The identified closures provide potential locations where injected $CO_2$ could accumulate within the B sand. Their size and geometry directly influence the available pore volume and therefore the amount of $CO_2$ that could potentially be stored. This makes accurate seismic interpretation an important part of evaluating depleted gas fields for storage.

The F3 fault is particularly important in understanding the containment of the identified closures. The juxtaposition analysis shows that the B sand on the upthrown and downthrown sides is in contact across much of the fault. This sand-against-sand relationship means that the fault geometry alone does not indicate a complete seal. However, two sections, approximately between positions 4 and 6 and between positions 8 and 9, show the reservoir juxtaposed against a finer-grained interval. These sections are more favourable from a containment perspective because the fine-grained material may restrict fluid movement across the fault.

The downthrown C sand also occurs above the reservoir along the interpreted fault trace and contributes to the overall structural arrangement of the storage compartments. Fault juxtaposition is an important part of evaluating possible fluid pathways because it shows which geological units are brought into contact by fault displacement (Bretan et al., 2003; Færseth, 2006; Yielding et al., 1997). The F3 interpretation therefore provides useful information about the geological configuration of the storage compartments and identifies areas where the fault may play a role in containment.

This aspect of the study adds to the previous work of Shah et al. (2024). While the earlier study established the potential storage capacity of Kadanwari, the present study provides additional information on the relationship between the reservoir and F3 fault. This is important because $CO_2$ storage potential depends not only on the amount of available pore

space but also on the geological arrangement that allows the injected $CO_2$ to remain within the storage interval.

The three investigated closures have a combined estimated storage capacity of approximately 0.1185 Mt of $CO_2$. This is a relatively modest volume compared with large-scale storage projects, but it represents a measurable storage opportunity within the investigated part of the Kadanwari field. The estimated capacity is approximately of the order of one-tenth of a year's injection at the Sleipner storage project (Furre et al., 2017). It is also much smaller than the approximately 1.6 Gt storage potential estimated by Holloway et al. (2009) for depleted gas fields in Pakistan. These values are not directly comparable because Holloway et al. (2009) considered depleted gas fields across Pakistan, whereas this study focuses on three specific closures within one reservoir interval at Kadanwari.

The difference in scale nevertheless provides useful context for the Kadanwari results. The estimated 0.1185 Mt or 576,599 tonnes should be viewed as the potential storage volume of the investigated closures rather than as the total storage potential of the Kadanwari field. The three closures are controlled mainly by their structural area and geometry, with larger closures providing greater pore volume where suitable reservoir conditions are present.

The storage calculation is based on the available pore volume, $CO_2$ density and storage efficiency. A $CO_2$ density of 600 kg/m$^3$ was used to convert the available pore volume into an estimated mass of stored $CO_2$. In a more detailed assessment, $CO_2$ density could be calculated under the specific reservoir pressure and temperature conditions using an appropriate equation of state (Span & Wagner, 1996). Similarly, the storage efficiency factor is important because only a proportion of the total pore space is expected to be effectively occupied by injected $CO_2$ (Bachu et al., 2007).

When the reservoir, structural and volumetric results are considered together, Kadanwari shows several favourable characteristics for $CO_2$ storage. The continuous B sand response indicates the presence of a laterally extensive reservoir, the identified closures provide potential structural traps, and the surrounding shale-rich formations provide a suitable geological setting for containment. The F3 interpretation further shows that the fault has different juxtaposition relationships along its length, with some sections being more favourable for containment than others.

Overall, the findings of this study support the previous interpretation of Shah et al. (2024) that Kadanwari has potential for geological $CO_2$ storage. The present study adds further detail by demonstrating the lateral continuity of the B sand, providing predicted

reservoir properties, examining the F3 fault relationship and estimating the capacity of three individual closures. The combined estimated capacity of approximately 0.1185 Mt demonstrates that the investigated closures contain a meaningful volume of potential storage space.

The results therefore indicate that the Kadanwari field can be considered a potential depleted-gas-field storage site, particularly within the B sand and the identified structural closures. The study demonstrates that the storage potential of Kadanwari is supported by the combination of reservoir distribution, structural closure and available pore volume. Further detailed evaluation of the field can build on this geological framework and provide a stronger basis for assessing its suitability for future $CO_2$ injection and long-term storage.

# CONCLUSIONS

The conclusions are stated below against the three research objectives of Section 1.5, followed by the overall outcome of the storage assessment.

1. Structural seismic demarcated the Horst and Graben structures, and Lower Goru sand B-sand was marked as the potential reservoir zone through Petrophysical analysis in well Kadanwari-01 while in well Kadanwari-03 H-sand was marked which determined key reservoir properties along reservoir zone.
2. By using Extra tree Regressive algorithms reservoir attributes like volume of shale, effective porosity, water saturation and permeability were computed, due to data limitations and skewness in well data, these results were less accurate and were further incorporated with model based seismic inversion.
3. Model based Seismic Inversion developed the final impedance model at B interval having less impedance sandwiched between high impedances. Furthermore, key parameters like Volume of shale, porosity, water saturation and permeability were computed at that reservoir level.
4. Fault Seal analysis was performed along B sand, which produced juxtaposition of sand and shale providing possible sealing sites and using formulae along 3 storage closures P90, P50, P10 storage capacity was calculated. P10 closure had the most storage capacity and along 3 closure and total combined capacity of the three is approximately 576,599 tones, or about 0.5765 Mt of CO2.

## REFERENCES

Ahmad, N., & Chaudhry, S. (2002). Kadanwari Gas Field, Pakistan: A disappointment turns into an attractive development opportunity. Petroleum Geoscience, 8(4), 307–316. https://doi.org/10.1144/petgeo.8.4.307

Ahmad, N., Fink, P., Sturrock, S., Mahmood, T., & Ibrahim, M. (2004). Sequence stratigraphy as predictive tool in Lower Goru fairway, Lower and Middle Indus Platform, Pakistan. In PAPG Annual Technical Conference (pp. 85–104). Pakistan Association of Petroleum Geoscientists.

Ahmad, N., Spadini, G., Palekar, A., & Subhani, M. A. (2007). Porosity prediction using 3D seismic inversion, Kadanwari gas field, Pakistan. Pakistan Journal of Hydrocarbon Research, 17, 95–102.

Ahmad, S., & Ghazi, S. (2022). Depositional trends and reservoir geometries of the Early Cretaceous Lower Goru Formation in Lower Indus Basin, Pakistan: Evidence from sequence stratigraphy. Journal of Petroleum Exploration and Production Technology, 12(11), 2981–3001.

Ali, A., Azeem, T., Khalid, R. F., & Hussain, M. (2023). Delineation of thin-bedded sands and porosity using post-stack seismic inversion in the Lower Goru Formation, Kadanwari gas field, Pakistan. Journal of Earth System Science, 132(2), Article 60. https://doi.org/10.1007/s12040-023-02071-8

Ali, M., Arif, M., Sahito, M. F., Al-Anssari, S., Keshavarz, A., Barifcani, A., Stalker, L., Sarmadivaleh, M., & Iglauer, S. (2019a). CO2-wettability of sandstones exposed to traces of organic acids: Implications for CO2 geo-storage. International Journal of Greenhouse Gas Control, 83, 61–68.

Ali, M., Khan, M. J., Ali, M., & Iftikhar, S. (2019b). Petrophysical analysis of well logs for reservoir evaluation: A case study of "Kadanwari" gas field, Middle Indus Basin, Pakistan. Arabian Journal of Geosciences, 12(6), Article 215. https://doi.org/10.1007/s12517-019-4389-x

Ali, N., Chen, J., Fu, X., Hussain, W., Ali, M., Hussain, M., Anees, A., Rashid, M., & Vo Thanh, H. (2022). Prediction of Cretaceous reservoir zone through petrophysical modeling: Insights from Kadanwari gas field, Middle Indus Basin. Geosystems and Geoenvironment, 1(3), Article 100058.

Allan, U. S. (1989). Model for hydrocarbon migration and entrapment within faulted structures. AAPG Bulletin, 73(7), 803–811. https://doi.org/10.1306/44B4A271-170A-11D7-8645000102C1865D

Amer, M., Mabrouk, W. M., Eid, A. M., & Metwally, A. (2025). 3D seismic modeling of the Amal oil field to evaluate CO2 storage potential in depleted reservoirs, southern Gulf of Suez. Scientific Reports, 15. https://doi.org/10.1038/s41598-025-03032-5

Archie, G. E. (1942). The electrical resistivity log as an aid in determining some reservoir characteristics. Transactions of the AIME, 146(1), 54–62.

Asquith, G. B., Krygowski, D., & Gibson, C. R. (2004). Basic well log analysis (2nd ed.). American Association of Petroleum Geologists.

Azeem, T., Chun, W. Y., Lisa, M., Khalid, P., Qing, L. X., Ehsan, M. I., Munawar, M. J., & Wei, X. (2017). An integrated petrophysical and rock physics analysis to improve reservoir characterization of Cretaceous sand intervals in Middle Indus Basin, Pakistan. Journal of Geophysics and Engineering, 14(2), 212–225.

Bachu, S. (2003). evaluation and ranking of sedimentary basins for sequestration of CO2 in geological media in response to climate change. Environmental Geology, 44(3), 277–289. https://doi.org/10.1007/s00254-003-0762-9

Bachu, S., Bonijoly, D., Bradshaw, J., Burruss, R., Holloway, S., Christensen, N. P., & Mathiassen, O. M. (2007). CO2 storage capacity estimation: Methodology and gaps. International Journal of Greenhouse Gas Control, 1(4), 430–443. https://doi.org/10.1016/S1750-5836(07)00086-2

Baig, M. O., Harris, N. B., Ahmed, H., & Baig, M. O. A. (2016). Controls on reservoir diagenesis in the Lower Goru sandstone formation, Lower Indus Basin, Pakistan. Journal of Petroleum Geology, 39(1), 29–47. https://doi.org/10.1111/jpg.12626

Bashir, A., Ali, M., Patil, S., Aljawad, M. S., Mahmoud, M., Al-Shehri, D., Hoteit, H., & Kamal, M. S. (2024). Comprehensive review of CO2 geological storage: Exploring principles, mechanisms, and prospects. Earth-Science Reviews, 249, Article 104672.

Berger, A., Gier, S., & Krois, P. (2009). Porosity-preserving chlorite cements in shallow-marine volcaniclastic sandstones: Evidence from Cretaceous sandstones of the Sawan

gas field, Pakistan. AAPG Bulletin, 93(5), 595–615. https://doi.org/10.1306/01300908096

Breiman, L. (2001). Random forests. Machine Learning, 45(1), 5–32. https://doi.org/10.1023/A:1010933404324

Breiman, L., Friedman, J. H., Olshen, R. A., & Stone, C. J. (1984). Classification and regression trees. Wadsworth.

Bretan, P., Yielding, G., & Jones, H. (2003). Using calibrated shale gouge ratio to estimate hydrocarbon column heights. AAPG Bulletin, 87(3), 397–413. https://doi.org/10.1306/08010201128

Færseth, R. B. (2006). Shale smear along large faults: Continuity of smear and the fault seal capacity. Journal of the Geological Society, 163(5), 741–751. https://doi.org/10.1144/0016-76492005-162

Fareed, A. G., Khoja, A. H., De Felice, F., Petrillo, A., Sultan, M. A., Jalalzai, Z. K., & Daood, S. S. (2023). Underground geological sequestration of carbon dioxide (CO2) and its effect on possible enhanced gas and oil recovery in a fractured reservoir of Eastern Potwar Basin, Pakistan. Science of the Total Environment, 905, Article 167124.

Friedlingstein, P., O'Sullivan, M., Jones, M. W., Andrew, R. M., Hauck, J., Landschützer, P., Le Quéré, C., Li, H., Luijkx, I. T., Olsen, A., Peters, G. P., Peters, W., Pongratz, J., Schwingshackl, C., Sitch, S., Canadell, J. G., Ciais, P., Jackson, R. B., Alin, S. R., … Zeng, J. (2025). Global Carbon Budget 2024. Earth System Science Data, 17(3), 965–1039. https://doi.org/10.5194/essd-17-965-2025

Furre, A.-K., Eiken, O., Alnes, H., Vevatne, J. N., & Kiær, A. F. (2017). 20 years of monitoring CO2 injection at Sleipner. Energy Procedia, 114, 3916–3926. https://doi.org/10.1016/j.egypro.2017.03.1523

Geurts, P., Ernst, D., & Wehenkel, L. (2006). Extremely randomized trees. Machine Learning, 63(1), 3–42. https://doi.org/10.1007/s10994-006-6226-1

Hampson, D. P., Schuelke, J. S., & Quirein, J. A. (2001). Use of multiattribute transforms to predict log properties from seismic data. Geophysics, 66(1), 220–236. https://doi.org/10.1190/1.1444899

Hastie, T., Tibshirani, R., & Friedman, J. (2009). The elements of statistical learning: Data mining, inference, and prediction (2nd ed.). Springer.

Hazarika, S., Boruah, A., & Kumar, H. (2024). Study of pore structure of shale formation for CO2 storage. Materials Today: Proceedings, 99, 138–144.

Hepple, R. P., & Benson, S. M. (2005). Geologic storage of carbon dioxide as a climate change mitigation strategy: Performance requirements and the implications of surface seepage. Environmental Geology, 47(4), 576–585.

Holloway, S., Garg, A., Kapshe, M., Deshpande, A., Pracha, A. S., Khan, S. R., Mahmood, M. A., Singh, T. N., Kirk, K. L., & Gale, J. (2009). An assessment of the CO2 storage potential of the Indian subcontinent. Energy Procedia, 1(1), 2607–2613. https://doi.org/10.1016/j.egypro.2009.02.027

Hossain, S., Rahman, N., & Shekhar, H. (2024). Sedimentological and petrophysical characterization of the Bokabil Formation in the Surma Basin for CO2 storage capacity estimation. Scientific Reports, 14(1). https://doi.org/10.1038/s41598-024-66373-7

Kadri, I. B. (1995). Petroleum geology of Pakistan. Pakistan Petroleum Limited.

Kazmi, A. H., & Jan, M. Q. (1997). Geology and tectonics of Pakistan. Graphic Publishers.

Khan, M. J., & Khan, H. A. (2018). Petrophysical logs contribute in appraising productive sands of Lower Goru Formation, Kadanwari concession, Pakistan. Journal of Petroleum Exploration and Production Technology, 8(4), 1089–1098. https://doi.org/10.1007/s13202-018-0472-1

Khan, Z. U., Ahmed, Z., Naseer, M. T., Kontakiotis, G., Naseem, S., Janjuhah, H. T., Antonarakou, A., & Panagiotopoulos, I. P. (2024). Assessing the hydrocarbon potential of the Kadanwari gas field using integrated seismic and petrophysical data. Journal of Petroleum Exploration and Production Technology, 14(6), 1349–1364. https://doi.org/10.1007/s13202-024-01780-0

Khan, Z. U., Hussain, M., & Ahmed, S. A. (2023). Bayesian stochastic inversion with petro-elastic relation to quantify thin gas sands of Khadro Formation, Zamzama gas field. Episodes, 46(3), 389–405.

Knipe, R. J. (1997). Juxtaposition and seal diagrams to help analyze fault seals in hydrocarbon reservoirs. AAPG Bulletin, 81(2), 187–195.

Kohavi, R. (1995). A study of cross-validation and bootstrap for accuracy estimation and model selection. In Proceedings of the 14th International Joint Conference on Artificial Intelligence (Vol. 2, pp. 1137–1143). Morgan Kaufmann.

Krois, P., Mahmood, T., & Milan, G. (1998). Miano field, Pakistan: A case history of model driven exploration. In Proceedings of the Pakistan Petroleum Convention (pp. 111–131). Pakistan Association of Petroleum Geologists.

Metz, B., Davidson, O., de Coninck, H., Loos, M., & Meyer, L. (Eds.). (2005). IPCC special report on carbon dioxide capture and storage. Cambridge University Press.

Mohamed, I. M., & Nasr-El-Din, H. A. (2013). Fluid/rock interactions during CO2 sequestration in deep saline carbonate aquifers: Laboratory and modeling studies. SPE Journal, 18(3), 468–485.

Pedregosa, F., Varoquaux, G., Gramfort, A., Michel, V., Thirion, B., Grisel, O., Blondel, M., Prettenhofer, P., Weiss, R., Dubourg, V., Vanderplas, J., Passos, A., Cournapeau, D., Brucher, M., Perrot, M., & Duchesnay, E. (2011). Scikit-learn: Machine learning in Python. Journal of Machine Learning Research, 12, 2825–2830.

Poupon, A., & Leveaux, J. (1971). Evaluation of water saturation in shaly formations. In Transactions of the SPWLA 12th Annual Logging Symposium (Paper O). Society of Petrophysicists and Well-Log Analysts.

Priezzhev, I. I., Veeken, P. C. H., Egorov, S. V., & Strecker, U. (2019). Direct prediction of petrophysical and petroelastic reservoir properties from seismic and well-log data using nonlinear machine learning algorithms. The Leading Edge, 38(12), 949–958. https://doi.org/10.1190/tle38120949.1

Raza, M., Khan, F., Khan, M. Y., Riaz, M. T., & Khan, U. (2020). Reservoir characterization of the B-interval of Lower Goru Formation, Miano 9 and 10, Miano area, Lower Indus Basin, Pakistan. Environmental & Earth Sciences Research Journal, 7(1), 18–32.

Razaq, M., Ali, A., Rehman, K., Hussain, M., & Amin, Y. (2025). Carbon storage assessment using machine learning approaches in Qadirpur Gas Field, Pakistan. Acta Geophysica. Advance online publication. https://doi.org/10.1007/s11600-025-01649-8

Ringrose, P. (2020). How to store CO2 underground: Insights from early-mover CCS projects. Springer. https://doi.org/10.1007/978-3-030-33113-9

Ringrose, P. S., Mathieson, A. S., Wright, I. W., Selama, F., Hansen, O., Bissell, R., Saoula, N., & Midgley, J. (2013). The In Salah CO2 storage project: Lessons learned and knowledge transfer. Energy Procedia, 37, 6226–6236. https://doi.org/10.1016/j.egypro.2013.06.551

Russell, B., & Hampson, D. (1991). Comparison of poststack seismic inversion methods. In SEG Technical Program Expanded Abstracts 1991 (pp. 876–878). Society of Exploration Geophysicists. https://doi.org/10.1190/1.1888870

Saif-Ur-Rehman, K. J., Lin, D., Ehsan, S. A., Jadoon, I. A. K., & Idrees, M. (2020). Structural styles, hydrocarbon prospects, and potential of Miano and Kadanwari fields, Central Indus Basin, Pakistan. Arabian Journal of Geosciences, 13(2), Article 97. https://doi.org/10.1007/s12517-020-5122-5

Shah, S. Y. A., Du, J., Iqbal, S. M., Du, L., Khan, U., Zhang, B., & Tan, J. (2024). Integrated three-dimensional structural and petrophysical modeling for assessment of CO2 storage potential in gas reservoir. Lithosphere, 2024(4), Article lithosphere_2024_222. https://doi.org/10.2113/2024/lithosphere_2024_222

Shakir, U., Ali, A., Hussain, M., Azeem, T., & Bashir, L. (2022). Selection of sensitive post-stack and pre-stack seismic inversion attributes for improved characterization of thin gas-bearing sands. Pure and Applied Geophysics, 179(1), 169–196. https://doi.org/10.1007/s00024-021-02900-1

Span, R., & Wagner, W. (1996). A new equation of state for carbon dioxide covering the fluid region from the triple-point temperature to 1100 K at pressures up to 800 MPa. Journal of Physical and Chemical Reference Data, 25(6), 1509–1596. https://doi.org/10.1063/1.555991

Surachman, L. M., Abdulraheem, A., Al-Shuhail, A., & Kaka, S. I. (2024). Acoustic impedance prediction based on extended seismic attributes using multilayer perceptron, random forest, and extra tree regressor algorithms. Journal of Petroleum Exploration and Production Technology, 14(7), 1923–1931. https://doi.org/10.1007/s13202-024-01795-7

Vo Thanh, H., Sugai, Y., & Sasaki, K. (2020). Impact of a new geological modelling method on the enhancement of the CO2 storage assessment of E sequence of Nam Vang field,

offshore Vietnam. Energy Sources, Part A: Recovery, Utilization, and Environmental Effects, 42(12), 1499–1512.

Yang, B., Shao, C., Hu, X., Ngata, M. R., & Aminu, M. D. (2023). Advances in carbon dioxide storage projects: Assessment and perspectives. Energy & Fuels, 37(3), 1757–1776.

Yielding, G., Freeman, B., & Needham, D. T. (1997). Quantitative fault seal prediction. AAPG Bulletin, 81(6), 897–917. https://doi.org/10.1306/522B498D-1727-11D7-8645000102C1865D

Zou, C., Zhao, L., Xu, M., Chen, Y., & Geng, J. (2021). Porosity prediction with uncertainty quantification from multiple seismic attributes using random forest. Journal of Geophysical Research: Solid Earth, 126(7), Article e2021JB021826. https://doi.org/10.1029/2021JB021826

# 13% Overall Similarity

The combined total of all matches, including overlapping sources, for each database.

## Filtered from the Report

- Bibliography
- Quoted Text

## Match Groups

**204** Not Cited or Quoted 7%
Matches with neither in-text citation nor quotation marks

**143** Missing Quotations 5%
Matches that are still very similar to source material

**0** Missing Citation 0%
Matches that have quotation marks, but no in-text citation

**0** Cited and Quoted 0%
Matches with in-text citation present, but no quotation marks

## Top Sources

7% Internet sources
9% Publications
8% Submitted works (Student Papers)